NONLINEAR CONTROL AND ACTIVE DAMPING OF A FORCED-FEEDBACK METERING POPPET VALVE

A Dissertation
presented to
the Faculty of the Graduate School
at the University of Missouri – Columbia

In Partial Fulfillment
of the Requirements for the Degree
Doctor of Philosophy

By

C. HARVEY O. CLINE

Dr. Roger Fales, Dissertation Supervisor

DECEMBER 2007

The undersigned, appointed by the dean of the Graduate School, have examined the dissertation entitled

NONLINEAR CONTROL AND ACTIVE DAMPING OF A FORCED-FEEDBACK METERING POPPET VALVE

presented by C. Harvey O. Cline,

a candidate for the degree of doctor of philosophy,

and hereby certify that, in their opinion, it is worthy of acceptance.

Professor Roger Fales

Professor John Miles

Professor Craig Kluever

Professor Steven Borgelt

Professor Robert McLaren

ACKNOWLEDGEMENTS

First and foremost, I want to thank Jesus Christ, my Lord and Savior, for taking hold of the awesome gift of salvation for me. It is only through the grace of God that I do anything.

I want to supremely thank Dr. Roger Fales for taking me on as his graduate student. His extensive understanding of controls and hydraulic systems has ushered in another chapter of intellectual growth in my life. He provided an environment where I was able to hone my research abilities and solidify a knowledge base, which had been initiated in course work. Because of his style and approach I complete my Ph.D. program with the confidence that I need to perform any research and development job.

I would like to thank Dr. Satish Nair for agreeing to work with me as an undergraduate student and teaching me how to conduct research.

I would also like to thank Dr. John Miles, Dr. Craig Kluever, Dr. Steven Borgelt, and Dr. Robert McLaren for agreeing to serve on my doctoral committee and tolerating my “last minute” style.

I would like to thank my research colleagues Chang, Kristie, Tai, Tim, and Tony. Throughout my tenure as a Ph.D. student, each one of these individuals contributed to my growth in their own way.

Finally, I would like to acknowledge my wife, Yasmin Cline. There are no words to describe the support that she provided for me. She rejoiced with me during the good times, and she suffered with me in the bad times. Her willingness to put her career on hold for my Ph.D. program is to be commended in this age and the age to come. We earned a Doctoral of Philosophy Degree.

TABLE OF CONTENTS

LIST OF FIGURES

LIST OF TABLES

NONLINEAR CONTROL AND ACTIVE DAMPING OF A FORCED-FEEDBACK METERING POPPET VALVE

C. Harvey O. Cline

Dr. Roger Fales, Dissertation Supervisor

ABSTRACT

For a metering poppet valve which was developed at the University of Missouri (MU valve), the valve can be configured for performance at the cost of stability. It is desirable to achieve both performance and stability using electronic control. Presently, in the MU valve, the pilot poppet motion is damped by the flow of hydraulic fluid through a channel or orifice running through the poppet. In this research, it is proposed that the solenoid be used to provide damping (active damping) to the pilot poppet. The damping input signal to the solenoid is determined as a function of the pilot poppet velocity. In practice, the velocity is difficult to measure due to the MU valve's configuration and it is estimated according to the self-sensing actuator concept. Theoretical results demonstrated that a valve actuator could be designed with an emphasis on high speed performance while an electronic control system is used to damp unwanted oscillations. For flow control, several researchers have used feedback linearization to cancel part of a hydraulic system's nonlinearities in spool valves. In the case of the metering poppet valve, feedback linearization is an attractive approach since experimental studies have shown that poppet instabilities are caused by nonlinear mechanisms like flow forces. In this work, nonlinearities are cancelled in the input-output relationship of the metering poppet valve. The controller was shown to achieve robust tracking of a reference trajectory.

CHAPTER 1

INTRODUCTION

1.1 BACKGROUND, MOTIVATION, AND OBJECTIVES

Hydraulic control systems are used to transfer power via fluid. Such systems can be valve-controlled or pump-controlled. Each arrangement offers certain advantages and disadvantages over the other. For the valve-controlled hydraulic system, a control valve is used to control the flow and pressure difference between the hydraulic input component (the pump) and the hydraulic output component (the actuator).

Control valves may be classified according to the function-type. Three broad categories of function-type are generally accepted: directional-control valves, pressure-control valves, and flow-control valves. Directional-control valves mechanically shift the direction of fluid flow. Pressure-control valves maintain or limit the pressure in a circuit at a specific level. Flow-control valves continuously modulate the fluid flow in a hydraulic circuit. Valves may also be classified according to the construction type. Typically, the major restrictive components of the valve define its classification. Examples include poppet valves and spool valves, each type having a poppet or spool, respectively, which provides the primary restriction, as shown in Figure 1.1. In the present research, a poppet type flow-control valve is studied.

Poppet valves have been available for many years but mostly limited in use to provide pressure-relief in high-powered hydraulic circuits. Recently, there has been an

interest in developing poppet valves for flow metering applications in place of the typically used spool valves [1-5]. The poppet valve offers certain advantages over the spool valve. Mainly, poppet valves have extremely low leakage when closed, require less precise machining, are capable of adjusting themselves with wear, and are self-flushing and therefore less sensitive to contamination [6]. Key disadvantages to using the poppet valve for flow metering are centered on dynamic instability issues [7-9]. Here, "dynamic instabilities" refers to undesirable oscillations in the valve position response. Such oscillations result in unacceptable fluctuations in flow control and possibly vibrations in the mechanical system being controlled by the hydraulic system.

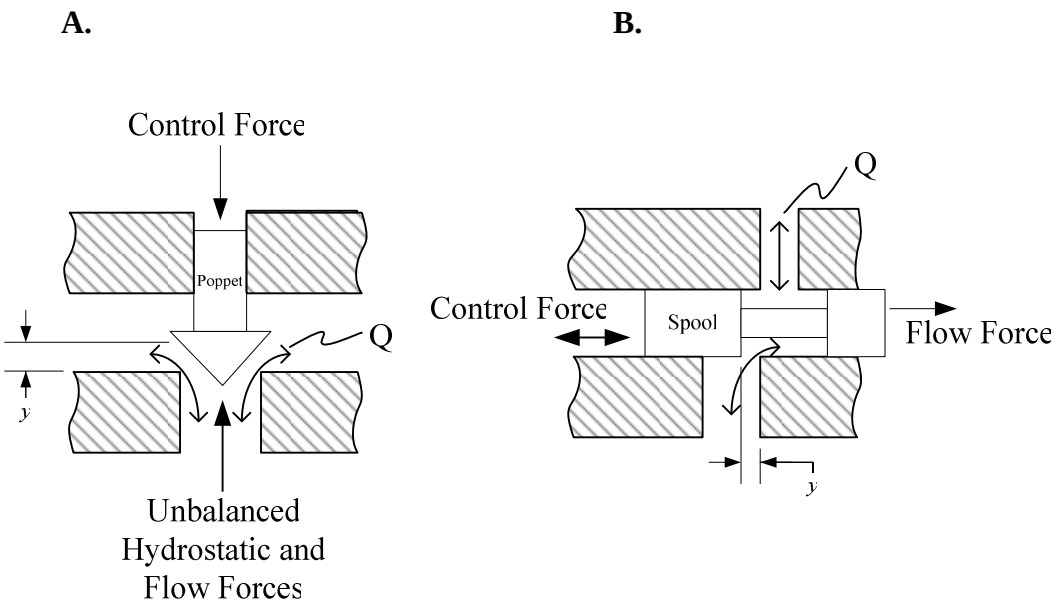

Figure 1.1: Poppet (A) and spool (B) valves

The objective of the research documented in this dissertation is to produce a closed-loop metering poppet valve hydraulic system capable of performance while ensuring stability. Towards this end, two complementary sub-objectives were formulated: (1) develop active damping to attenuate the instabilities of an open-loop

metering poppet valve hydraulic circuit; (2) develop a nonlinear feedback control system for a closed-loop metering poppet valve circuit. These sub-objectives were first pursued using modeling and simulation techniques and then using experimentation with a solenoid ElectroMechanical Actuator and components of a valve prototype.

The valve used in the present study was developed at the University of Missouri-Columbia (MU valve). It is a two-stage, electrohydraulic, forced-feedback, metering poppet valve, Figure 1.2. The pilot poppet is actuated by a solenoid ElectroMechanical Actuator (EMA) while the main poppet is hydraulically actuated by the pressure in a control volume which is situated between the main poppet and the pilot poppet. The valve incorporates forced-feedback in the form of a feedback spring.

In Figure 1.2, the valve is in the closed position with high pressure connected to the inlet port and low pressure connected to the outlet port. In order to raise the main poppet off its seat, current is supplied to the solenoid EMA which forces the pilot poppet off its seat. Fluid is then allowed to flow from the control volume through the pilot poppet orifice to the outlet port.

With the pilot poppet initial opening, the flow through the control volume inlet orifice is smaller than the flow through the pilot poppet orifice producing a net outflow from the control volume and decreasing the pressure in the control volume. The pressure in the control volume decreases to a level where the net force on the main poppet is in an upward direction, effectively lifting the main poppet off its seat. This opens an orifice between the high pressure inlet port and low pressure outlet port through which passes a metered flow.

The upward movement of the main poppet pushes on the pilot poppet through the feedback spring. The force on the spring causes the pilot poppet to move towards its seat decreasing the size of its orifice until a steady state is reached where flow into the control volume equals flow out of the control volume and the pressure in the control volume balances the upward force on the main poppet. At this point, both poppets are no longer moving but are off their seats allowing flow through their orifices.

The pilot poppet is pressure balanced by allowing flow of hydraulic fluid from the control volume to pass through a tube in the pilot poppet into a pressurized volume (pilot volume) above the pilot poppet. In addition, the fluid flow through the tube has a damping affect on the pilot poppet since the tube provides a small flow resistance and thus a pressure drop. A 7^{th} order mathematical model of this valve has been developed by Muller & Fales [10,11].

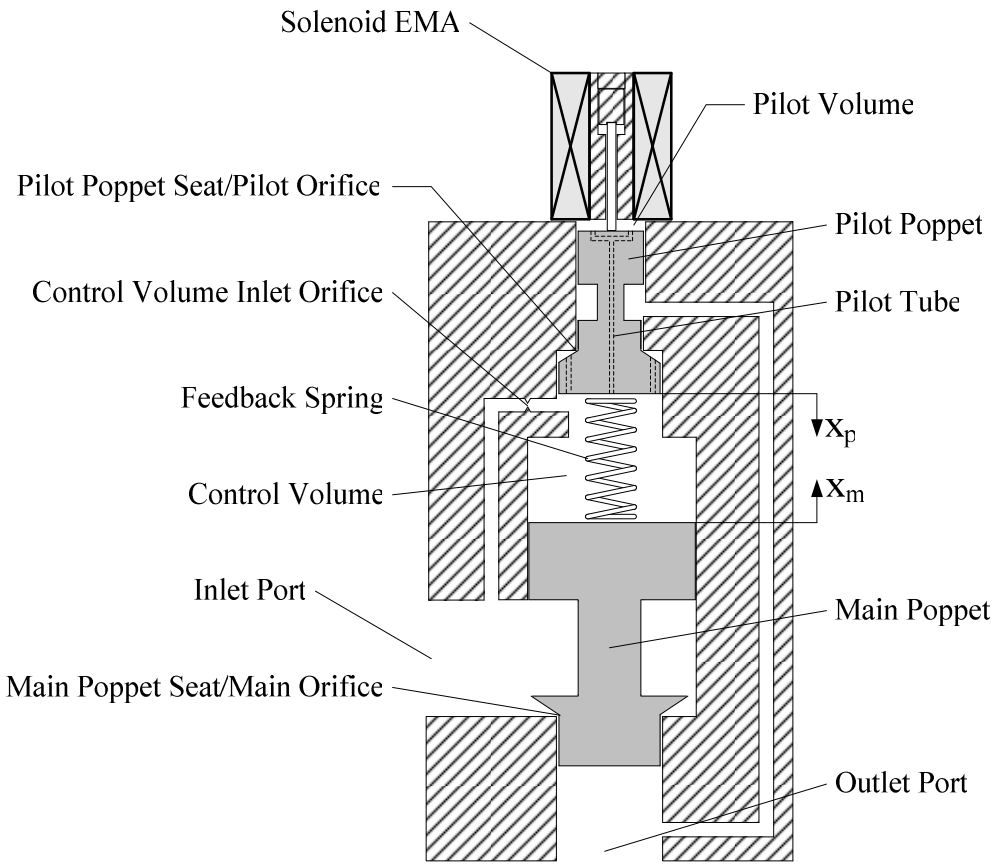

Figure 1.2: Forced-feedback metering poppet valve configuration

1.2 LITERATURE REVIEW

1.2.1 Stability

The literature contains many studies of the stability of hydraulic systems with poppet valves. In a review of these studies, Hayashi distinguishes between local and global stability [7]. This important distinction helps to reconcile the results from theoretical studies with those from experimental studies. Theoretical studies used linear approximations to examine the system's stability behavior in the neighborhood of equilibrium points. Experimental studies produced results not predicted in theory,

indicating that poppet valve hydraulic systems were operating in regions too far from the equilibrium point for linear approximations to predict behavior accurately.

The primary behavior discussed by Hayashi which is not predicted by theoretical studies is “hard” self-excited vibrations [7]. These vibrations took the form of relatively large amplitude, sustained oscillations of the poppet. This behavior occurred at stable steady states and was induced by sufficiently large disturbances. In the phase plane, “hard” self-excited vibrations were represented by a stable equilibrium point within a semi-stable limit cycle where trajectories outside (inside) the limit cycle converged (diverged) to (from) it. It has been shown that this behavior is affected by nonlinearities.

At this point, it is important to note that linear control techniques would be based solely on the linear approximations which produced the local stability results and thus unable to control the complete range of actual system behaviors. Local and global behavior must be considered when designing controllers for these types of systems. Since the systems global behavior is impacted by system nonlinearities, nonlinear control strategies are advisable.

Hayashi and Ohi [9] studied the mechanisms of instability in a pressure-relief poppet valve circuit through an analysis of the mechanical energy of the poppet. They found that, for one cycle of sinusoidally varying poppet displacement and valve chamber pressure, the phase lag of the pressure with respect to the poppet displacement caused the energy added to the poppet by flow forces to exceed the energy extracted from the poppet by damping. The net result was an increase in the mechanical energy of the poppet during one cycle. The authors discussed three primary contributors to the phase lag: hydraulic fluid compressibility, interference by other system components, and negative

damping forces. It was concluded that these mechanisms are essentially responsible for a poppet valve circuit's instabilities. Further, it was theorized that the instabilities can be attenuated with an actively increased damping force on the poppet.

It is important to emphasize that the hydraulic circuits used in the studies reviewed to this point employed poppet valves in the pressure-relief role. While the results from the studies discussed to this point are applicable, it is important to directly study the stability behavior of metering poppet valve hydraulic circuits.

Zhang et al. and Fales [1,12] have studied the stability characteristics and performance limitations of one of the few metering poppet valves available to the hydraulic industry, the Valvistor. This metering poppet valve is a two-stage, electrohydraulic flow valve. The pilot poppet is actuated by an EMA while the main poppet is hydraulically actuated by the pressure in a control volume which is situated between the main poppet and the pilot poppet. Flow from the control volume through the pilot poppet orifice is the primary mechanism for control of the pressure in the control volume. Thus, the flow through the pilot poppet orifice both controls and contributes to total flow. Zhang et al. used linear analysis and experimental validation to obtain results which indicated that the dual effect of the pilot poppet orifice flow on the total flow limits the closed loop performance of valve controlled systems. Analytically, the pilot poppet orifice flow was shown to result in performance limiting open loop zeros.

Fales [12] added to the simulation results of Zhang et al. and showed that the valve dynamics vary with supply pressure. In addition, it was shown that the speed of response and steady state flow error increased with supply pressure and oscillations occurred at the higher supply pressures. In an attempt to improve performance, Fales

examined the effect of parameter variations. His results showed increased performance with decreased stability. In addition, the implications of these results for controller design were briefly discussed. A controller would need to change with the system's dynamics in order to maintain optimal performance.

1.2.2 Metering Poppet Valve Control

Muller has developed electronic, feedback control for a metering poppet valve to control flow [10]. The importance of this study lies in the fact that the valve used, is the same valve used in the present research. Four controllers were developed and tested by Muller. The first controller made use of a look-up table which contained a functional relationship between desired flow and required solenoid force. This relationship was determined as a function of the pressure drop across the valve. Essentially, this controller was an open-loop controller with a feedforward path. Results showed that a comprehensive look-up table across the range of pressure drop values is important. In addition, results showed the existence of flow oscillations at high pressure drops.

In principle, the look-up table is not a robust approach if it is determined using a representative production valve and then applied to other production valves. Developing a closed-loop control system would enhance the robustness of the look-up table approach by providing feedback of the output. This was the case with the next controller developed by Muller. Valve flow feedback with Proportional Derivative (PD) control was used with the look-up table. Results showed more damping with reduced transient spikes as well as reduced steady state error. Gain scheduled PD control was tried without the look-up table and resulted in a higher steady state error. The best controller, which

consisted of a combination of gain scheduled PD control with table look-up, exhibited the best damping, reduction of transient spikes and steady state error.

Opdenbosch et al. conducted a modeling and control study of an electro-hydraulic poppet valve [13]. The valve used by Opdenbosch et al. was a flow metering poppet valve very similar in configuration to the valve used in the present research. In the work by Opdenbosch et al., modeling the valve was the focus with a brief treatment of control. The control focused on reference tracking of desired states. This was accomplished using a Nodal Link Perceptron Network. Though tracking was achieved, Opdenbosch et al. made no mention of any other performance or stability criteria.

1.2.3 Nonlinear Control of Valves

Feedback linearization is one nonlinear control method developed to handle system nonlinearities and draw from linear systems control theory to ensure stability and performance. This type of controller is capable of handling global system behavior and has seen use in a wide variety of applications including spool type metering valve systems. Sohl and Bobrow investigated the application of a feedback linearization control strategy for force and position reference tracking by a hydraulic spool valve servo system [14]. The result was a nonlinear controller which better handled system nonlinearities as compared to advanced linear controllers. Hahn et al. conducted a simulation study of the input-output, feedback linearization control technique applied to an electrohydraulic spool valve servo system [15]. The controller demonstrated excellent transient and robustness performance.

1.2.4 Self-Sensing Actuator Concept

Typically, in order to determine the position of the spool or poppet in a flow control valve, an LVDT is used. In the literature, an alternative approach that uses the estimator based self-sensing actuator concept is detailed. If an EMA is used to manipulate the position, this concept proposes to estimate the position and velocity using a dynamic model of the EMA and the electronic signals from the actual system. This approach is attractive because it circumvents the increased hardware complexities which accompany the setup and attachment of an LVDT or other position transducers. In some cases, the self-sensing actuator concept makes possible the acquisition of position when the direct measurement of position is otherwise impractical.

Several Researchers in the fluid power community have made use of the self-sensing actuator concept [16-19]. Eyabi [16] used this concept with a sliding mode estimator to determine the position for the closed-loop control of an electromagnetic valve actuation system. Yuan and Li [17-19] conducted several modeling and experimental studies on the self-sensing determination of position and velocity information for a dual solenoid actuator configuration. The work done by these two researchers contrasts with each other in many ways, but most importantly in terms of the complexity of the EMA model used. Yuan and Li used a simplified model which neglected certain effects, where as the model developed and used by Eyabi was more comprehensive.

In the research conducted by Yuan and Li, signal processing techniques along with estimator design were used to determine the position and velocity states. In particular, in order to avoid mechanical loading uncertainties, Yuan and Li did not

directly estimate the position and velocity. Instead, they estimated the flux linkage of the solenoid EMA and used this estimate with the current measurement to calculate the position and velocity states. For estimators, they attempted to use the boxcar window observer and a Kalman filter. The research of Eyabi and Yuan and Li validated the self-sensing actuator approach with Yuan and Li highlighting the importance of an accurate solenoid model.

Outside fluid power applications, researchers faced with situations where a reduction in the number of signal carrying wires is necessary have also been attracted to the self-sensing actuator concept. These applications include magnetic bearings, heart pumps, and reluctance motors [20-22].

1.2.5 Summary

In summary, the literature reviewed indicates that pressure-relief poppet valves are inherently susceptible to local instabilities. In the flow metering poppet valve, these instabilities persist. Designs have been created which ensure stability, but at the cost of performance (speed of response). In the flow metering poppet valve, performance is important for flow control and disturbance rejection. It is thus desired that a metering poppet valve meet certain performance criteria while remaining stable. The particular approaches of active damping and nonlinear control have been suggested to maintain performance while attenuating stabilities. The self-sensing actuator concept makes the previously impractical approach of active damping possible.

1.3 DISSERTATION OUTLINE

This dissertation is organized into two, self-sustaining, sections. In the first section, the focus is on the development of active damping. In the second section, the focus is on the development of an input-output, feedback linearization controller. The first section is composed of chapters 2 and 3 while the second section is composed of chapter 4. Both sections focus on the MU valve discussed above. The MU valve model is the only component shared between the two sections. Thus, some variables introduced in the first section for the MU valve model will not be reintroduced in the second section.

In chapter 2, the theoretical foundation is laid for the self-sensing actuator concept and the active damping approach. Here, in chapter 2, only modeling and simulation results are presented. Three self-sensing actuator approaches are developed and the optimal design of the three was chosen for use with active damping. A proportional active damping scheme is attempted. The simulation results demonstrate the advantages and disadvantages of the proposed active damping scheme. The results are intended as a "proof of concept" for both the self-sensing actuator concept and the active damping approach. In chapter 3, the results of experiments conducted on a solenoid testbed are presented and discussed. Here, the central characteristic of the solenoid EMA, which makes possible the self-sensing actuator concept, is highlighted.

In chapter 4, the mathematical development of the input-output feedback linearization controller is detailed. Here, certain necessary conditions for the application of this type of controller are presented and shown to be satisfied. Results were obtained from a mathematical model and focus on the controller's ability to perform reference

tracking under four different pressure conditions. In addition, certain mechanisms inherent to the system which affect the controller's linearization are shown numerically, discussed analytically and given a physical interpretation. The controller's robustness and disturbance rejection are briefly analyzed using simulations. The conclusions on all results from this work are presented in chapter 5 along with future work.

CHAPTER 2

SOLENOID DAMPING OF THE PILOT POPPET – DEVELOPMENT AND MODELING STUDY

2.1 INTRODUCTION

With passive damping, a physical mechanism, such as sliding friction or fluid drag, dissipates the kinetic energy of a moving object. The dissipative mechanisms are usually intrinsic to the system of interest and input energy to these mechanisms is not necessary for the dissipative mechanisms to remove kinetic energy. In contrast, active damping involves the active modulation of input energy to active damping mechanisms such that these mechanisms dissipate kinetic energy in a controlled way. In the present study, the benefit of an active damping approach is that the valve can be designed with a greater emphasis on performance while active damping is used to reduce the accompanying dynamic instabilities. As previously stated, "dynamic instabilities" refers to undesirable oscillations in the valve's response to input commands. Thus, for active damping, there must be a means for sensing instabilities, an input which modulates the damping of the valve, and a stated control law to modulate the input energy to produce the desired kinetic energy dissipation.

The input to the metering poppet valve used in the present study is the electromechanical force applied to the pilot poppet by the solenoid. This force is electronically controlled and thus can be adjusted to provide appropriate damping on the pilot poppet. The importance of pilot poppet operation is indicated by the fact that the

main poppet is hydraulically actuated, while the pilot poppet controls this hydraulic force. Therefore, due to the input location of the metering poppet valve used in the present study and the functional significance of the pilot poppet, this poppet was chosen as the point of application for active damping.

The position and velocity information of the pilot poppet can be used to identify dynamic instabilities. To measure position and velocity, a position transducer can be connected to the poppet or spool of a flow control valve to determine its position. Here, the pilot poppet position and velocity information are not measured due to increased hardware complexities. Also, there are economic reasons for not measuring position due to increased manufacture costs. For these reasons, the self-sensing actuator concept is used. The self-sensing actuator concept involves the measurement and use of the electrical variables (current and voltage) of a solenoid EMA to estimate the position and velocity of its armature. Here, the position and velocity information of the armature is also the position and velocity information of the pilot poppet. Since velocity holds the dynamic information of the pilot poppet mass, it will be used in the active damping scheme.

The objective of the research presented in this chapter is to evaluate the feasibility of using the solenoid with the self-sensing actuator concept [17-19] to achieve pilot poppet damping in order to attenuate dynamic instabilities. This is first done with modeling and simulation techniques.

2.2 MATHEMATICAL MODELING

A simplified representation of the pilot poppet was modeled to ease the initial development and analysis of the estimator and controller concepts. This model consists of a mass and spring mechanical system enclosed in a pressurized cylinder. The flow of hydraulic fluid through a tube in the mass is modeled to simulate the pressure balancing and damping effects on the pilot poppet. A solenoid is included to force the mass down against the spring as shown in Figure 2.1.

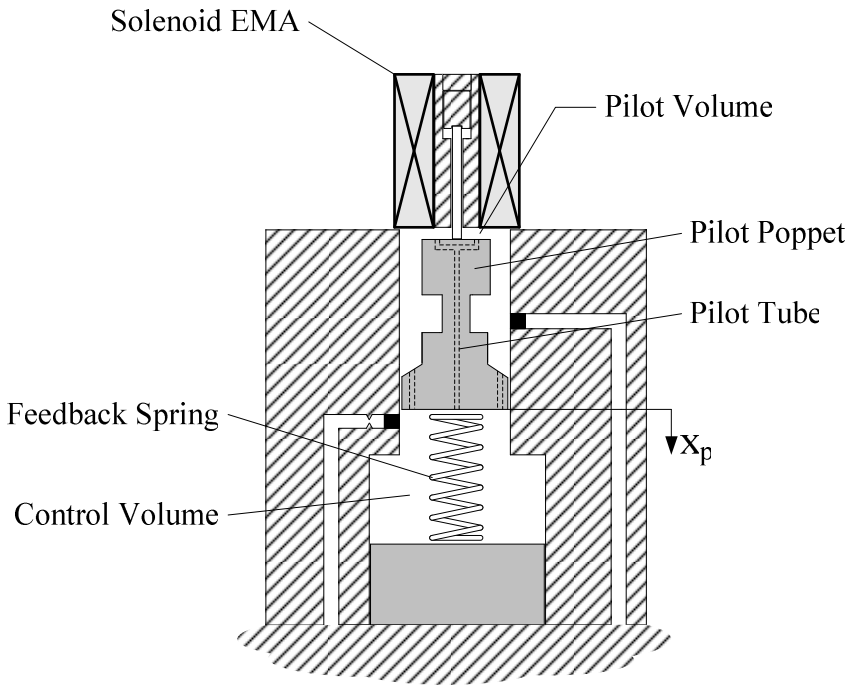

Figure 2.1: Simplified model configuration

The proposed model is a 4^{th}-order model composed of three ordinary differential equations: one mass-spring equation of motion for the pilot poppet, one pressure rise rate equation for the pressurized volumes above and below the mass and an electric circuit equation for the solenoid. For the mass, Newton's Second Law of Motion was applied

with terms accounting for the solenoid actuator force ($\lambda^2/2\beta_2$), pressure forces (ΔPA) and the spring force ($k\left(x_p + X_{sid}\right)$). The governing equation of motion for the mass is as follows:

$$m\ddot{x}_p = \frac{\lambda^2}{2\beta_2} - \Delta PA - k\left(x_p + X_{sid}\right), \tag{2.1}$$

where m is the pilot poppet mass (kg), x_p is the pilot poppet position (m), λ is the flux linkage of the solenoid EMA (Wb), β_2 is a composite solenoid parameter (see Appendix B.4) (H-m), ΔP is the net pressure acting on the pilot poppet (Pa), A is the surface area acted on by the net pressure (m), k is the feedback spring constant (N/m^2), and X_{sid} is the feedback spring preload (m). A mathematical expression for the solenoid EMA force was derived by Yuan and Li [17-19] and is used in Eq. 2.1.

A solenoid EMA consists primarily of a coil of wire with an iron core and an armature, Figure 2.2. With a constant current passing through the coil, the flux linkage depends on the position of the armature. The definition of flux linkage is stated as:

$$\lambda = L\left(x_p\right)i, \tag{2.2}$$

where L is the position dependent inductance of the coil (H) and i is the current in the solenoid coil (A). Eq. 2.2, indicates that it must be the solenoid inductance L that varies with the position of the armature. Thus, for the solenoid EMA, Kirchoff's Voltage Law (KVL) was applied to a Resistor-Inductor (RL)-circuit, Figure 2.2, with a position-dependent inductance.

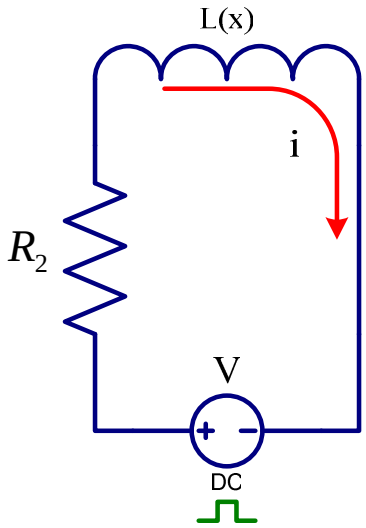

Figure 2.2: Solenoid EMA electrical circuit

The result of KVL is given by:

$$V - R_2 i - \dot{\lambda} = 0\,, \tag{2.3}$$

where V is the voltage across the coil (Volts) and R_2 is the current resistance of the EMA (Ω).

A mathematical expression for the position dependent inductance was derived by Yuan and Li [17-19] and is used in the present research. The position dependent inductance is represented by:

$$L(x_p) = \frac{\beta_2}{d + x_p} \tag{2.4}$$

where d is a composite solenoid parameter (see Appendix B.4) (m).

Substituting for i and rearranging terms produces the first order equation used to simulate the electrical dynamics of the solenoid EMA:

$$\dot{\lambda} = -\frac{R_2}{\beta_2}\left(d + x_p\right)\lambda + V \tag{2.5}$$

As discussed above, the self-sensing actuator concept uses the voltage and current. The voltage (V) is the input (u) to the model, $u = V$. To access the current (i) for the self-sensing actuator concept, it is defined as the output (y) of the model. This output current is determined using the following equation:

$$y = i = \frac{\lambda(d + x_p)}{\beta_2}. \tag{2.6}$$

Equation 2.6 was derived from Eqs. 2.2 & 2.4. This proposed approximation of the solenoid's dynamics is made possible by the exclusion of saturation and hysteresis effects of the model. Such simplifications are valid when the solenoid is designed to work in the linear region with little hysteresis, which is the case for most commercial valves [17-19].

The change in the pressures in the pressurized volumes above and below the mass can be determined using the pressure rise rate equations, which are given by:

$$\dot{P}_p = \frac{\beta}{(x_p + x_c)A}(Q - \dot{x}_p A), \tag{2.7}$$

$$\dot{P}_c = \frac{\beta}{(V_o - x_p A)}(-Q + \dot{x}_p A), \tag{2.8}$$

where P_p is the pressure in the volume above the pilot poppet (Pa), P_c is the pressure in the volume below the pilot poppet (Pa), β is the bulk modulus of the hydraulic fluid (Pa), x_c is the initial position of the pilot poppet (m), Q is the flow in the pilot poppet tube (m^3/s), and V_o is the initial volume of the space below the pilot poppet (m^3).

The pressures in the control volumes are represented by the net pressure acting on the mass ($\Delta P = P_c - P_p$). The rise rate equation for this net pressure is presented as:

$$\Delta\dot{P} = \frac{\beta(V_o + x_c A)}{(V_o - x_p A)(x_p + x_c)A}(-Q + \dot{x}A). \tag{2.9}$$

The flow through the mass (Q) is modeled as laminar flow through a tube by the following equation:

$$Q = \frac{\pi R^4}{8\mu L_p}(\Delta P) \tag{2.10}$$

where R is the radius of the pilot poppet tube, μ is the viscosity of the hydraulic fluid, and L_p is the length of the pilot poppet tube. Model parameters were taken from the work of Muller [10] and Yuan and Li [19] and are given in Appendix A.

For the self-sensing actuator concept, the discrete, linear equations of motion were needed. To facilitate this need, the model was converted into state space form, linearized and discretized. The derivation of the linearization and discretization forms used in the present study are presented in Appendix B.1 and B.2, respectively. Here, only the final forms are defined for convenience. The state space variables are defined as: $z_1 = x_p$, $z_2 = \dot{x}_p$, $z_3 = \Delta P$, and $z_4 = \lambda$. The state space equations were determined as follows:

$$\boldsymbol{z} = [z_1 \quad z_2 \quad z_3 \quad z_4]^T = [x_p \quad \dot{x}_p \quad \Delta P \quad \lambda]^T, \tag{2.11}$$

$$\dot{\boldsymbol{z}} = \boldsymbol{f}_o(\boldsymbol{z}, u) \tag{2.12}$$

$$y = h_o(\boldsymbol{z}), \tag{2.13}$$

where $\boldsymbol{z}$ is the 4 x 1 state vector. The nonlinear state function vectors were determined to be:

$$\boldsymbol{f}_o(\boldsymbol{z},u)=\begin{bmatrix} z_2 \\ \frac{1}{m}\left(\frac{z_4^2}{2\beta_2}-z_3A-k(z_1+X_{sid})\right) \\ \frac{\beta(V_o+x_cA)}{(V_o-z_1A)(z_1+x_c)A}\left(-\frac{\pi R^4}{8\mu L_p}z_3+z_2A\right) \\ -\frac{R_2}{\beta_2}(d+z_1)z_4+V \end{bmatrix}, \tag{2.14}$$

where $u=V$, and $h_o(\boldsymbol{z})=i=\frac{z_4(d+z_1)}{\beta_2}$. (2.15), (2.16)

The linear, state-space equations were determined to be:

$$\boldsymbol{\delta z}=\boldsymbol{z}-\boldsymbol{z}^*, \tag{2.17}$$

$$\boldsymbol{\delta \dot{z}}=\mathbf{A}\boldsymbol{\delta z}+\mathbf{B}\delta u, \tag{2.18}$$

$$\delta y=\mathbf{C}\boldsymbol{\delta z}, \tag{2.19}$$

where $\boldsymbol{\delta z}$ is the 4 x 1 state, perturbation vector (perturbation about the reference state trajectory), $\boldsymbol{z}^*$ is the 4 x 1 state, reference trajectory vector, δy is the output perturbation (perturbation about the reference output trajectory), δu is the input perturbation (perturbation about the reference input trajectory), $\mathbf{A}$ is the 4 x 4 system matrix, $\mathbf{B}$ is the 4 x 1 input vector, and $\mathbf{C}$ is the 1 x 4 output vector. The system matrix, input vector, output vector, and reference trajectory were determined to be:

$$\mathbf{A}=\begin{bmatrix} 0 & 1 & 0 & 0 \\ -\frac{k}{m} & 0 & -\frac{A}{m} & \frac{z_4^*}{m\beta_2} \\ 0 & \frac{\beta(V_o+x_cA)}{(V_o-z_1^*A)(z_1^*+x_c)} & \frac{\beta(V_o+x_cA)}{(V_o-z_1^*A)(z_1^*+x_c)A}\left(-\frac{\pi R^4}{8\mu L_p}\right) & 0 \\ -\frac{R_2}{\beta_2}z_4^* & 0 & 0 & -\frac{R_2}{\beta_2}(d+z_1^*) \end{bmatrix}, \tag{2.20}$$

$$\mathbf{B} = \begin{bmatrix} 0 & 0 & 0 & 1 \end{bmatrix}^T, \ \mathbf{C} = \begin{bmatrix} \frac{z_4^*}{\beta_2} & 0 & 0 & \frac{d + z_1^*}{\beta_2} \end{bmatrix}, \tag{2.21), (2.22}$$

and

$$\boldsymbol{z}^* = \begin{bmatrix} \frac{\left(z_4^*\right)^2}{2k\beta_2} - X_{sid} \\ 0 \\ 0 \\ u^* \frac{\beta_2}{R_2}\left(\frac{1}{d + z_1^*}\right) \end{bmatrix}. \tag{2.23}$$

The reference trajectory that the system was linearized about was its equilibrium point ($\boldsymbol{z}^*$), given by Eq. 2.23. Equation 2.23 is derived in Appendix B.3. The equilibrium point used in the simulations was chosen according to the following logic. In the simplified model, the spring is preloaded as is the case in the complete valve design. However, unlike in the complete valve design, there is no seat for the mass in the simplified model and the solenoid must hold the mass to maintain the volume of the space above the pilot poppet found in the completed valve design. The voltage required and the corresponding states together are the equilibrium point about which the simplified model was linearized.

Assuming control (u) is constant over a sample period, the discrete, linear state-space equations were determined to be:

$$\boldsymbol{\delta z}_k = \boldsymbol{z}_k - \boldsymbol{z}^* \tag{2.24}$$

$$\boldsymbol{\delta z}_{k+1} = \boldsymbol{\Phi}_k \boldsymbol{\delta z}_k + \mathbf{B}_k \delta u_k \tag{2.25}$$

$$\delta y_k = \mathbf{C}_k \boldsymbol{\delta z}_k \tag{2.26}$$

where $\boldsymbol{z}_k$ is the 4 x 1 discrete state vector, $\boldsymbol{\delta z}_k$ is the 4 x 1 discrete state, perturbation vector (perturbation about the reference state trajectory), δy_k is the discrete, output perturbation (perturbation about the reference output trajectory), δu_k is the discrete, input perturbation (perturbation about the reference input trajectory), $\mathbf{\Phi}_k$ is the 4 x 4 discrete system matrix (state transition matrix), $\mathbf{B}_k$ is the 4 x 1 discrete input vector, and $\mathbf{C}_k$ is the 1 x 4 discrete output vector. The discrete system matrix, discrete input vector, and discrete output vector, were determined as:

$$\mathbf{\Phi}_k = \mathbf{I} + \mathbf{A}T_s + \mathbf{A}^2 \frac{T_s^2}{2!} + \mathbf{A}^3 \frac{T_s^3}{3!} + \ldots \,, \tag{2.27}$$

$$\mathbf{B}_k = \mathbf{B}\left(\mathbf{I}T_s + \mathbf{A}\frac{T_s^2}{2!} + \ldots \right), \tag{2.28}$$

$$\mathbf{C}_k = \mathbf{C}\,, \tag{2.29}$$

where $\mathbf{I}$ is the 4 x 4 identity matrix and T_s is the sample period. In the present study, the higher-order terms for $\mathbf{\Phi}_k$ and $\mathbf{B}_k$ were neglected.

2.3 SELF-SENSING ACTUATOR CONCEPT

At the heart of the self-sensing actuator concept is state estimation. A state estimator must be developed which accepts as its inputs the voltage across and the current through the coil of the solenoid and has position and velocity estimates as its states. The literature provides a number of practical techniques that can be used to perform state estimation. Here, three related estimator types were investigated: a linear estimator with pole placement, a linearized Kalman filter, and an extended Kalman filter. Approaching

the problem by designing these three estimators allowed for a gradual increase in developmental complexity.

2.3.1 Linear Estimator with Pole Placement

A continuous linear estimator was developed first. This type of estimator uses a continuous linear model in state space form to represent the dynamics of the system [23]. Here, the linear model is the result of the linearization of the nonlinear model, Eqs. 2.17 – 2.22. This is summarized in Figure 2.3. The estimator itself is a linear dynamic system in state space form and is designed to estimate the state vector of the linearized model. The equation which comprises the linear estimator is given:

$$\dot{\hat{\boldsymbol{\delta z}}} = \hat{\mathbf{A}}\hat{\boldsymbol{\delta z}} + \hat{\mathbf{B}}\delta u + \mathbf{K}_{le}\delta y \tag{2.30}$$

where the symbol ^ over a variable denotes an estimate of that variable, $\hat{\mathbf{A}}$ is the 4 x 4 state matrix of the linear estimator, $\hat{\mathbf{B}}$ is the 4 x 1 input matrix of the linear estimator, and $\mathbf{K}_{le}$ is the 4 x 1 gain matrix of the linear estimator.

A straight forward derivation is used to determine the system ($\hat{\mathbf{A}}$), control ($\hat{\mathbf{B}}$), and gain ($\mathbf{K}_{le}$) matrices of the estimator. Define an estimate error vector as:

$$\boldsymbol{e} = \boldsymbol{\delta z} - \hat{\boldsymbol{\delta z}} \tag{2.31}$$

Taking the first time derivative of Eq. 2.31 and substituting into this derivative the model and estimator dynamics produces:

$$\dot{\boldsymbol{e}} = \mathbf{A}\boldsymbol{\delta z} + \mathbf{B}\delta u - \hat{\mathbf{A}}\hat{\boldsymbol{\delta z}} - \hat{\mathbf{B}}\delta u - \mathbf{K}_{le}\delta y \tag{2.32}$$

Substituting the model output dynamics into Eq. 2.32 and rearranging terms produces:

$$\dot{\boldsymbol{e}} = (\mathbf{A} - \mathbf{K}_{le}\mathbf{C})\boldsymbol{\delta z} - \hat{\mathbf{A}}\hat{\boldsymbol{\delta z}} + (\mathbf{B} - \hat{\mathbf{B}})\delta u \,. \tag{2.33}$$

In Eq. 2.33, setting $\hat{\mathbf{A}} = \mathbf{A} - \mathbf{K}_{le}\mathbf{C}$, $\hat{\mathbf{B}} = \mathbf{B}$ and substituting $\boldsymbol{\delta z} - \hat{\boldsymbol{\delta z}} = \boldsymbol{e}$ produces:

$$\dot{\boldsymbol{e}} = (\mathbf{A} - \mathbf{K}_{le}\mathbf{C})\boldsymbol{e} \tag{2.34}$$

To complete the estimator design, the pole-placement technique is used to determine $\mathbf{K}_{le}$ such that the estimator system matrix, $\mathbf{A} - \mathbf{K}_{le}\mathbf{C}$, is Hurwitz. When this is the case, the estimation error asymptotically approaches zero. The estimator is thus given by:

$$\dot{\delta\hat{\boldsymbol{z}}} = (\mathbf{A} - \mathbf{K}_{le}\mathbf{C})\delta\hat{\boldsymbol{z}} + \mathbf{B}\delta u + \mathbf{K}_{le}\delta y \tag{2.35}$$

In using the pole-placement technique to determine the estimator gain matrix ($\mathbf{K}_{le}$), the general rule is to choose $\mathbf{K}_{le}$ such that the estimator's system matrix, $\mathbf{A} - \mathbf{K}_{le}\mathbf{C}$, has eigenvalues 2 to 4 times larger than the eigenvalues of the model's system matrix causing the observer to be 2 to 4 times faster than the system's dynamics. This rule was applied here.

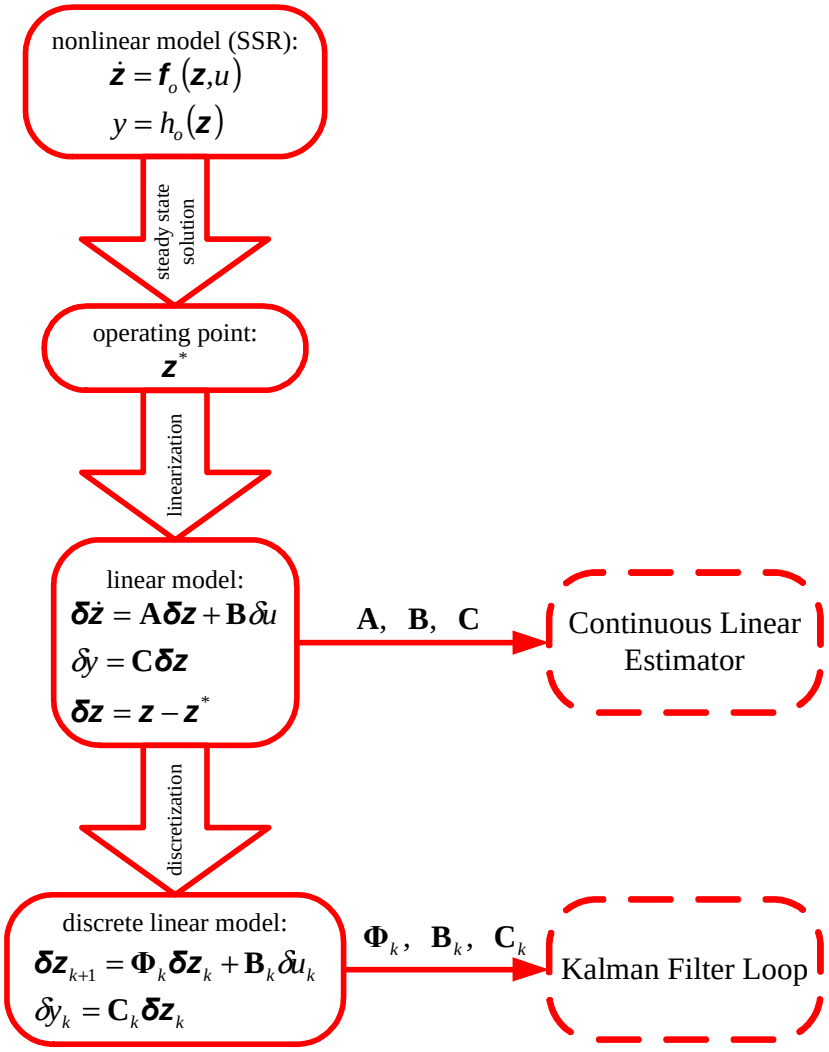

Figure 2.3: Linear estimator and Kalman filter pre-development

2.3.2 Kalman Filter

In the present work both a discrete linearized Kalman filter and an extended Kalman filter were developed. In this section, a brief explanation of the linearized Kalman filter is presented [24]. In the next section, the modifications to this linearized form which constitute the extended Kalman filter are discussed [24]. As the discussions will be brief, the reader is referred to the literature for a more comprehensive treatment of the filter derivation [24].

The discrete Kalman filter is a recursive state estimator which uses a discrete linear model in state space form to represent the dynamics of the system. As before, the linear model is the result of the linearization of the nonlinear model, Eqs. 2.17 -2.22, and this model is then discretized to obtain a discrete linear model, Eqs. 2.24 – 2.29. This is summarized in Figure 2.3. The derivation which produces the filter assumes that the discrete linear system is a discrete random process. This is modeled by adding process noise ($\boldsymbol{r}_k$) to the state equation, Eq. 2.25, and measurement noise (v_k) to the output equation, Eq. 2.26. The resulting discrete, linear, state-space system is given by:

$$\boldsymbol{\delta z}_{k+1} = \boldsymbol{\Phi}_k \boldsymbol{\delta z}_k + \mathbf{B}_k \delta u_k + \boldsymbol{r}_k , \tag{2.36}$$

$$\delta y_k = \mathbf{C}_k \boldsymbol{\delta z}_k + v_k . \tag{2.37}$$

where process noise and measurement noise are discrete, white, Gaussian noise processes with covariance matrix $\mathbf{R}_k$ and variance V_k, respectively. The process noise and measurement noise are uncorrelated.

The objective of the Kalman filter is to minimize the estimation error. Thus, similar to the linear estimator, an estimation error criterion is defined. Unlike the linear estimator situation, the system is a discrete random process and the conventional $\boldsymbol{e} = \boldsymbol{\delta z} - \boldsymbol{\delta \hat{z}}$ would not be a good criterion. It is the error covariance matrix ($\mathbf{P}_k$) associated with this estimation error that is used. It was determined as:

$$\mathbf{P}_k = \left(\mathbf{I} - \mathbf{K}_k \mathbf{C}_k\right)\mathbf{P}_k^- , \tag{2.38}$$

where $\mathbf{P}_k$ is the error covariance matrix, $\mathbf{K}_k$ is the Kalman filter gain matrix, and the symbol $^-$ in the superscript position to a variable denotes an *a priori* estimate of that variable. The error covariance matrix is important because it contains the estimation

error variances for the elements of the state vector being estimated along its major diagonal.

Kalman filter estimation begins with an *a prior* state estimate ($\boldsymbol{\delta}\hat{\mathbf{z}}_k^-$) and an *a prior* error covariance matrix ($\mathbf{P}_k^-$) and the measured system output ($y_{m,k}$). An *a priori* estimate output ($\hat{y}_k^-$) is created using the *a priori* state estimate and Eq. 2.26. The estimator compares the actual system measurement output with the *a priori* estimate output in order to update the *a priori* estimate. A linear update equation is used:

$$\boldsymbol{\delta}\hat{\mathbf{z}}_k = \boldsymbol{\delta}\hat{\mathbf{z}}_k^- + \mathbf{K}_k\left(y_{m,k} - \hat{y}_k^-\right) \tag{2.39}$$

In the derivation, optimization is done to develop Eq. 2.40, which will produce the proper gain matrix ($\mathbf{K}_k$) at each time step. This gain matrix is optimum in that the estimation error variances for the elements of the state vector being estimated along the major diagonal of the error covariance matrix are minimized. This gain is called the Kalman gain.

$$\mathbf{K}_k = \mathbf{P}_k^-\mathbf{C}_k^T\left(\mathbf{C}_k\mathbf{P}_k^-\mathbf{C}_k^T + V_k\right)^{-1} \tag{2.40}$$

For estimation at the next discrete time (t_{k+1}), the state estimate vector and error covariance matrix are projected ahead to produce *a priori* estimates, $\boldsymbol{\delta}\hat{\mathbf{z}}_{k+1}^-$ and $\mathbf{P}_{k+1}^-$ at the step *k+1*. This is done using the following equations:

$$\boldsymbol{\delta}\hat{\mathbf{z}}_{k+1}^- = \boldsymbol{\Phi}_k\boldsymbol{\delta}\hat{\mathbf{z}}_k + \mathbf{B}_k u_k \tag{2.41}$$

$$\mathbf{P}_{k+1}^- = \boldsymbol{\Phi}_k\mathbf{P}_k\boldsymbol{\Phi}_k^T + \mathbf{R}_k \tag{2.42}$$

The linearized Kalman filter loop in the proper sequence for digital computer execution is shown is Figure 2.4.

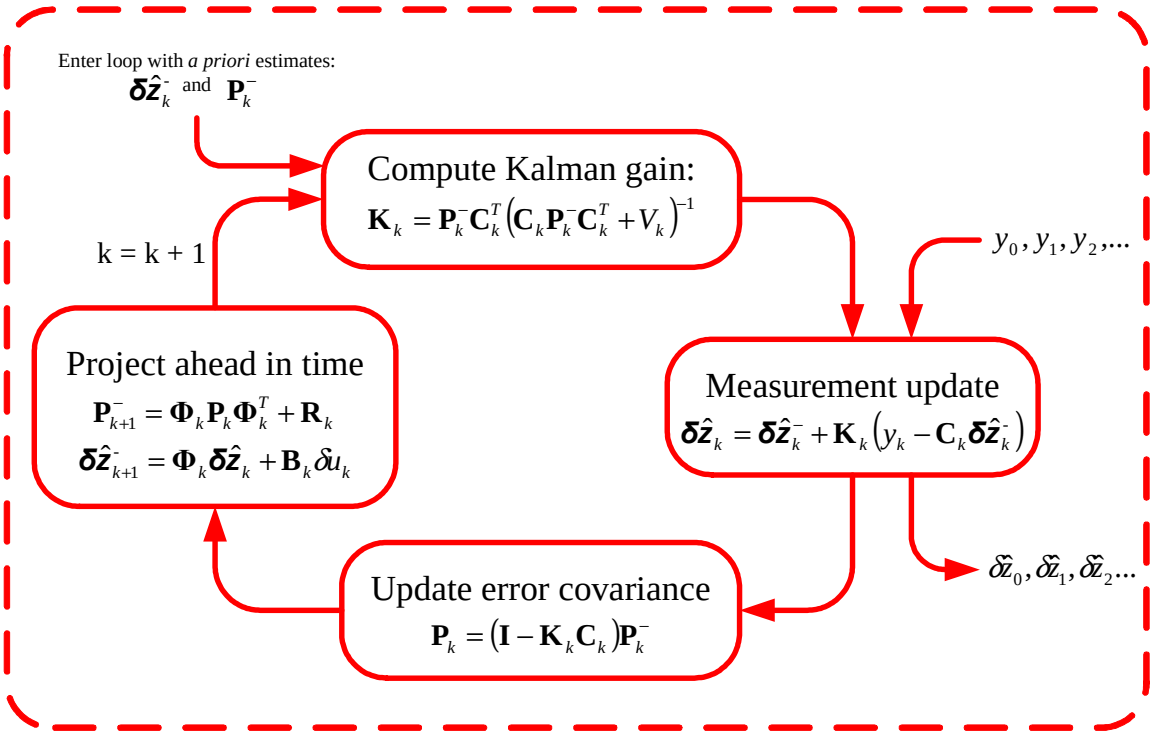

Figure 2.4: Kalman filter loop

2.3.3 Extended Kalman Filter

There are three differences between the extended Kalman filter used here and the linearized Kalman filter. First, with the linearized Kalman filter, the nonlinear model is linearized about a precomputed reference trajectory. With an extended Kalman filter, the nonlinear model is linearized at each time step about the updated state estimates' trajectory. Second, in the present study, the extended Kalman filter uses the nonlinear model dynamics and the Euler numerical integration technique to produce the *a priori* state estimates. This is done using the following equations:

$$\dot{\hat{\boldsymbol{z}}}_k^- = \boldsymbol{f}\left(\hat{\boldsymbol{z}}_k, u_k\right) \tag{2.43}$$

$$\hat{\boldsymbol{z}}_{k+1}^- = \hat{\boldsymbol{z}}_k + \dot{\hat{\boldsymbol{z}}}_k T_s \tag{2.44}$$

Finally, in the update Equation (2.39), the *a priori* estimate output ($\hat{y}_k^-$) is determined using the nonlinear output dynamics from Eq. 2.16:

$$\hat{y}_k^- = h\left(\hat{\boldsymbol{z}}_k^-\right). \tag{2.45}$$

The extended Kalman filter loop in the proper sequence for digital computer execution is shown is Figure 2.5.

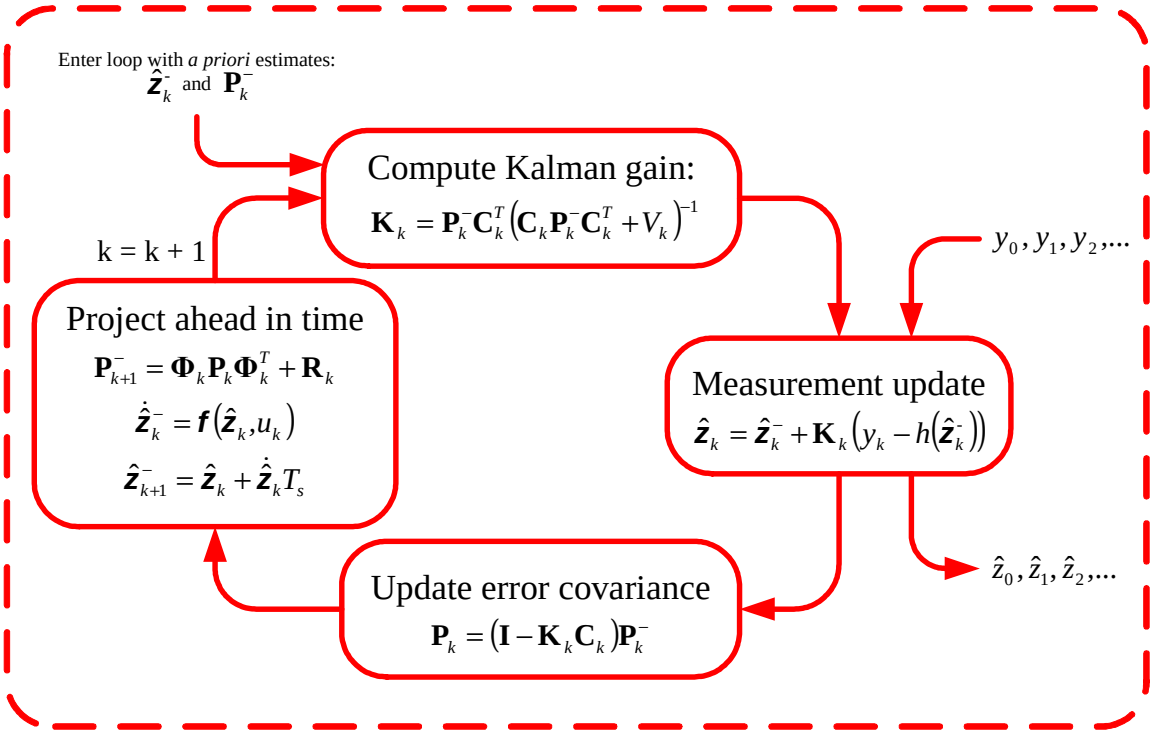

Figure 2.5: Extended Kalman filter loop

For both Kalman filters, measurement noise is simulated using the 'randn' command within Matlab. This command returns normally distributed random numbers with a mean of zero and standard deviation of one. To better simulate the noise of a current sensor, the random numbers can be multiplied by the standard deviation of an actual current sensor. Such a value was unavailable and the measurement noise was used

as a tuning parameter to adjust filter performance. In general, the process noise is also adjusted to produce desired filter performance. The $\mathbf{R}_k$ and V_k matrices used for both the linearized Kalman filter and extended Kalman filter are displayed in Appendix A.

2.4 ACTIVE DAMPING

To convert the estimated state into a damping input from the solenoid, a conversion gain (G) was tuned until satisfactory damping was accomplished. The control input based on the solenoid voltage command and estimated state is given as follows: (given in Eq. 2.46 and illustrated in Figure 2.6):

$$u = V - G\dot{\hat{x}}_p . \tag{2.46}$$

where G is the active damping gain (V-s/m).

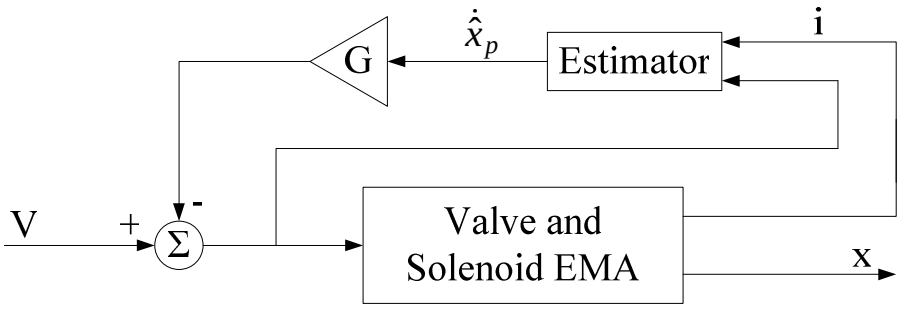

Figure 2.6: Active damping scheme

2.5 SIMULATION RESULTS AND DISCUSSION

2.5.1 Model

All modeling and simulations were carried out in the Matlab/Simulink environments. Using the 'eig' command within Matlab, the poles of the fourth order simplified model were determined to be: -3.64e6, -1.47e2, -2.35e1 + j4.10e2, and -2.35e1 - j4.10e2. Comparing the largest pole of -3.64e6 to the second largest pole of -1.47e2, it is evident that the dynamics of one of the state variables are considerably faster than the dynamics of the other state variables. Since electrical systems generally have faster dynamics than mechanical systems, it was initially assumed that the largest pole was associated with the dynamics of the EMA model. If the largest pole was associated with the dynamics of the EMA, these dynamics reach steady state much quicker than those of the other state variables. The dynamics of the EMA can be approximated as instantaneous and the λ state determined using a steady state equation. The steady state equation used to determine the λ state was derived by setting $\dot{\lambda}$ equal to zero in Eq. 2.5, then solving for λ to produce:

$$\lambda = \frac{\beta_2}{R_2(d+x)}u\,. \tag{2.47}$$

The replacement of the EMA's dynamics with Eq. 2.47 did not eliminate the largest pole. Since the elimination of the EMA's dynamics did not eliminate the largest pole and it was assumed that the complex-conjugate poles are associated with the states of the pilot poppet, it was theorized that the largest pole was associated with the pressure dynamics. The pressure dynamics in the cylinder were replaced by a steady state

equation, which was derived by setting $\Delta\dot{P}$ equal to zero in Eq. 2.9, substituting Eq. 2.10 into Eq. 2.9 for the *Q* variable, and then solving for ΔP to obtain:

$$\Delta P = \frac{\dot{x}8\mu L_p A}{\pi R^4} \tag{2.48}$$

This indeed eliminated the largest pole. To validate the reduced-order, simplified model (ROSM), the step responses of both models were compared at steps of 0.01 , 0.1 , and 1.0 *V*. The results, shown in Figure 2.7, demonstrate that there are negligible differences between the two models. Thus, the reduced-order, simplified model was used for the simulations that follow.

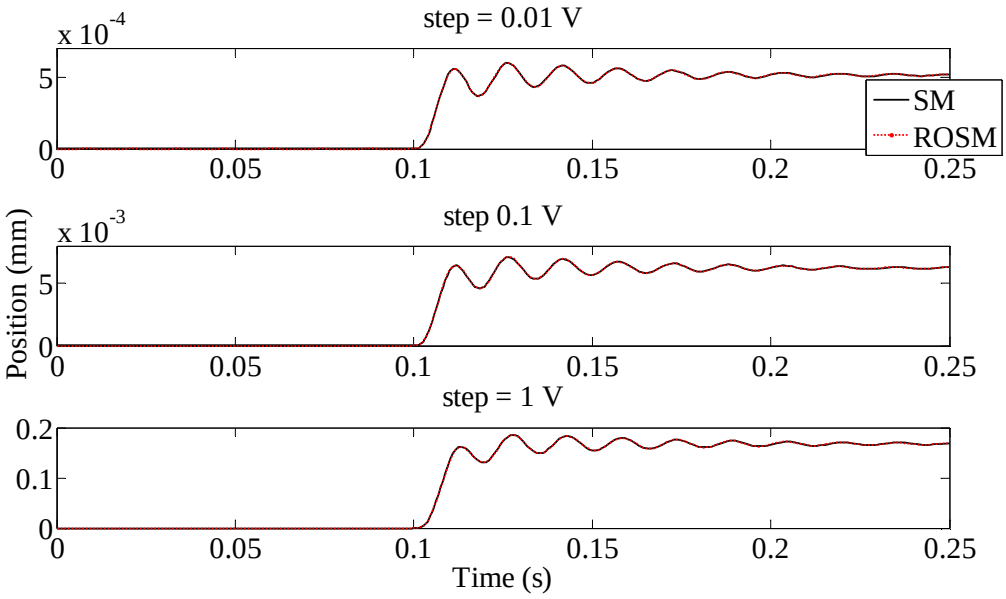

Figure 2.7: Simplified Model (SM) step response vs. Reduced-Order, Simplified Model step response (ROSM)

2.5.2 Self-Sensing Actuator Concept

The simulation results of the three types of estimators are shown in Figures 2.8 – 2.25. In these results the position and velocity of the nonlinear model are compared to the position and velocity of the estimators. Each estimator was tested at 0.01, 0.1, and 1.0 V steps from the operating point.

Comparing Figures 2.8 - 2.13 with Figures 2.14 - 2.19 indicates that the results for the pole placement estimator and the Kalman filter are the same. This is an expected result since the literature [23] reveals that the two estimator types are functionally the same. They differ in the determination of their estimator gain matrices, $\mathbf{K}_{le}$ and $\mathbf{K}_{k}$. The linear estimator is a suboptimal form of the Kalman filter where the choice of its gains does not optimize a performance criteria and it does not account for noise. The Kalman filter gain matrix is calculated to minimize the estimation error covariance matrix in the presence of white, Gaussian noise in the process and measurement. Since the inclusion of process and measurement noise sources creates a more realistic simulation, the Kalman filter is the superior of the two. From this point on, out of these two estimators, only the Kalman filter will be discussed.

The results of the Kalman filter and extended Kalman filter are presented in Figures 2.14 – 2.25. In the displayed results, the best estimation of position and velocity by the Kalman filter occurred at a step input level of 0.01 V (Figures 2.14 – 2.17). For the Kalman filter, at the 0.01 V step input level, there is transient and steady-state position estimation error. Compared to the Kalman filter position estimates at the other two step inputs, the Kalman filter's position estimation error at the 0.01 V step level is

small. For the Kalman filter's velocity estimate at the step input level of 0.01 V, there is indistinguishable error between the estimate and the nonlinear model state.

For the Kalman filter's position estimates, in response to the step level inputs of 0.1 and 1.0 V, there is increased transient and steady-state estimation error with the increase in input step, (Figures 2.15 and 2.16) . The Kalman filter's velocity estimate at the step level of 0.1 V displays peak-to-peak amplitude error relative to the nonlinear model state for the first 3 oscillations, (Figure 2.18). The peak-to-peak amplitude error decreases as the time after the step increases. The Kalman filter's velocity estimate in response to the step level of 1.0 V (Figure 2.19) is similar to the estimate at 0.1V. The Kalman filter's velocity estimation at both step levels exhibit peak-to-peak amplitude error with the error decreasing as steady-state is approached. However, the Kalman filter's velocity estimate at the step input level of 1.0 V has greater peak-to-peak amplitude error.

In contrast to the Kalman filter's position estimates, all of the Kalman filter's velocity estimates exhibit negligibly small steady state error. All of the Kalman filter's velocity estimates approach zero at steady state as does the nonlinear model state. At all three step level inputs, the extended Kalman filter produces estimates for both states which are indistinguishable from the nonlinear model's states (Figures 2.20 – 2.25).

Overall, these results show that the accuracy of the Kalman filter estimates degrade with step size. This is another expected outcome since the Kalman filter estimates the states of the linearized model. The ability of the linear model to approximate the states of the nonlinear model degrades with the deviation of the linear model's states from the operating point. Thus, the estimator is limited by the

linearization approximation. Here, the extended Kalman filter is not limited by a linearization about one operating point and so produces estimates, which appear in the Figures, as identical to the nonlinear model states at all three step level inputs.

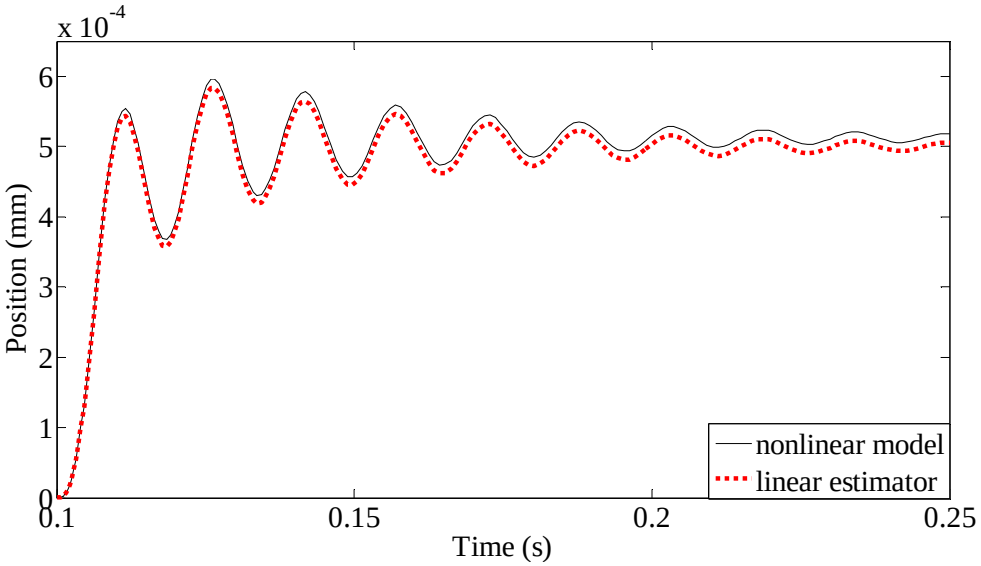

Figure 2.8: Linear estimator, position estimate in response to a step input level of 0.01 V

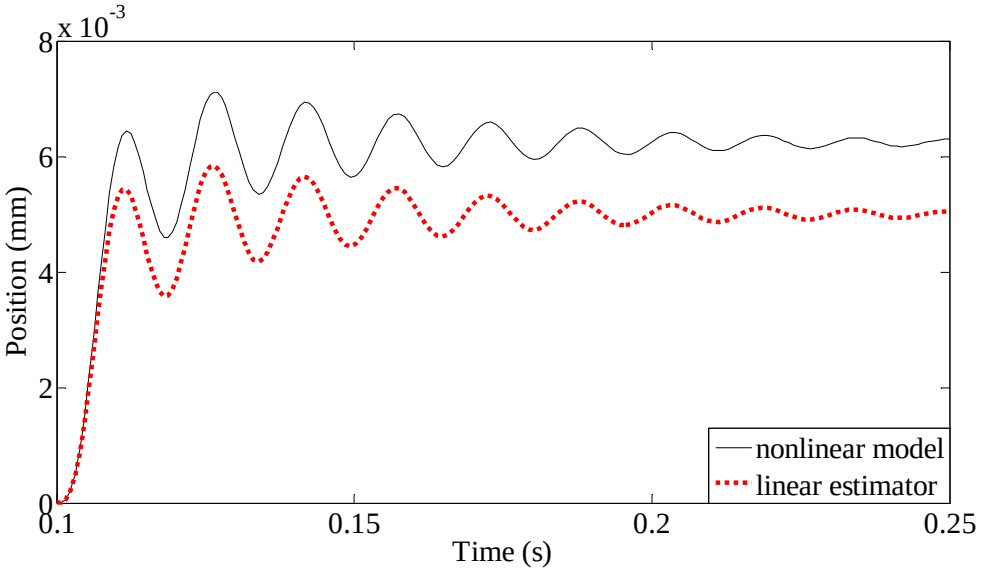

Figure 2.9: Linear estimator, position estimate in response to a step input level of 0.1 V

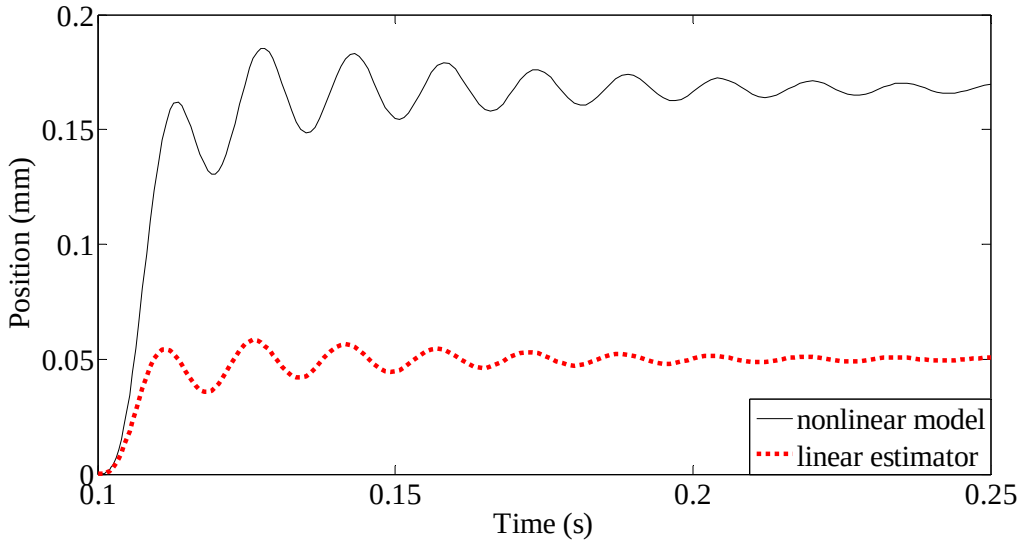

Figure 2.10: Linear estimator, position estimate in response to a step input level of 1.0 V

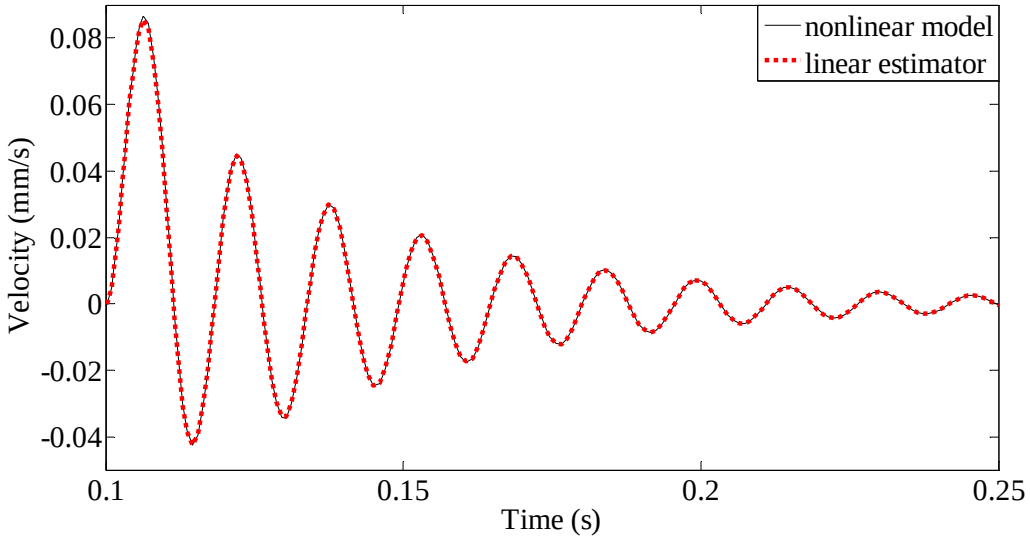

Figure 2.11: Linear estimator, velocity estimate in response to a step input level of 0.01 V

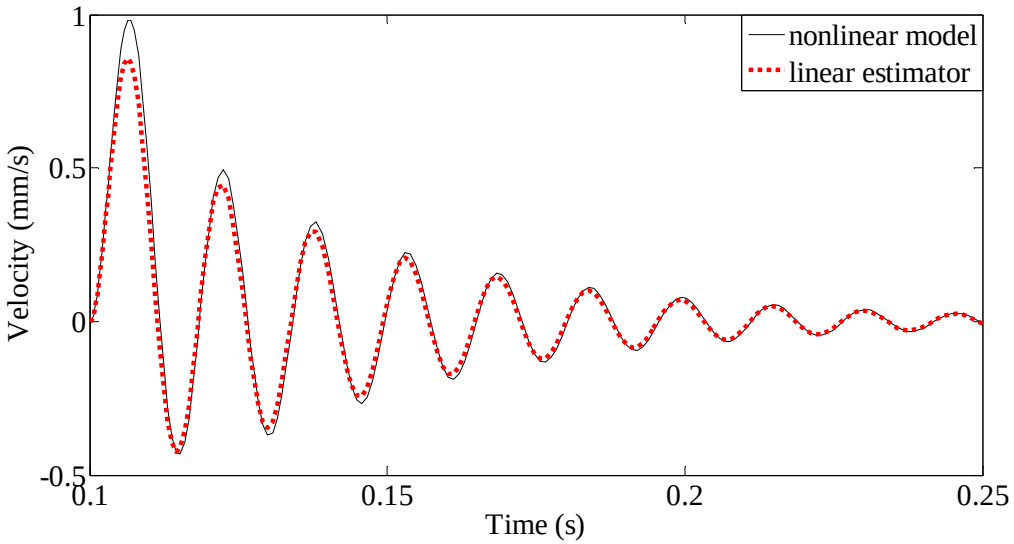

Figure 2.12: Linear estimator, velocity estimate in response to a step input level of 0.1 V

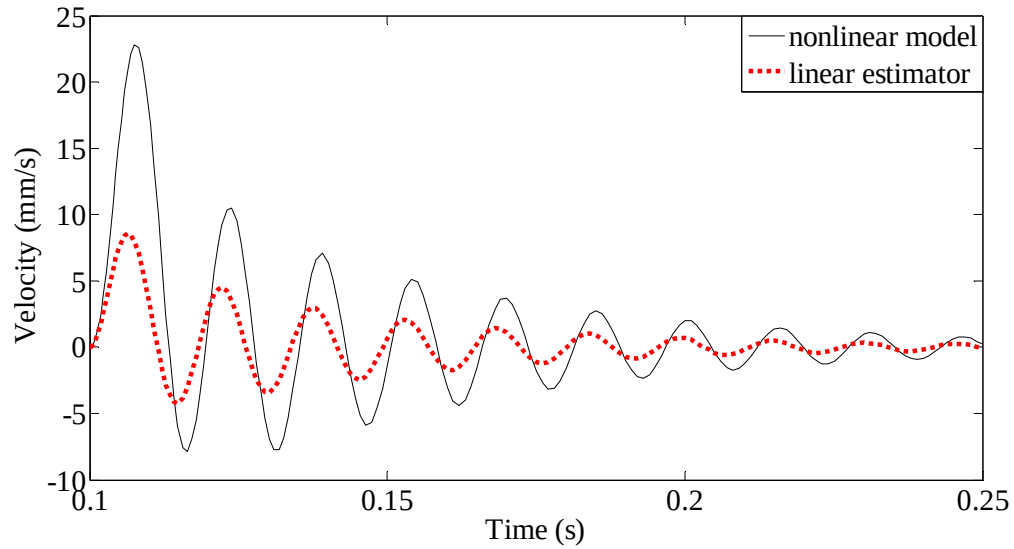

Figure 2.13: Linear estimator, velocity estimate in response to a step input level of 1.0 V

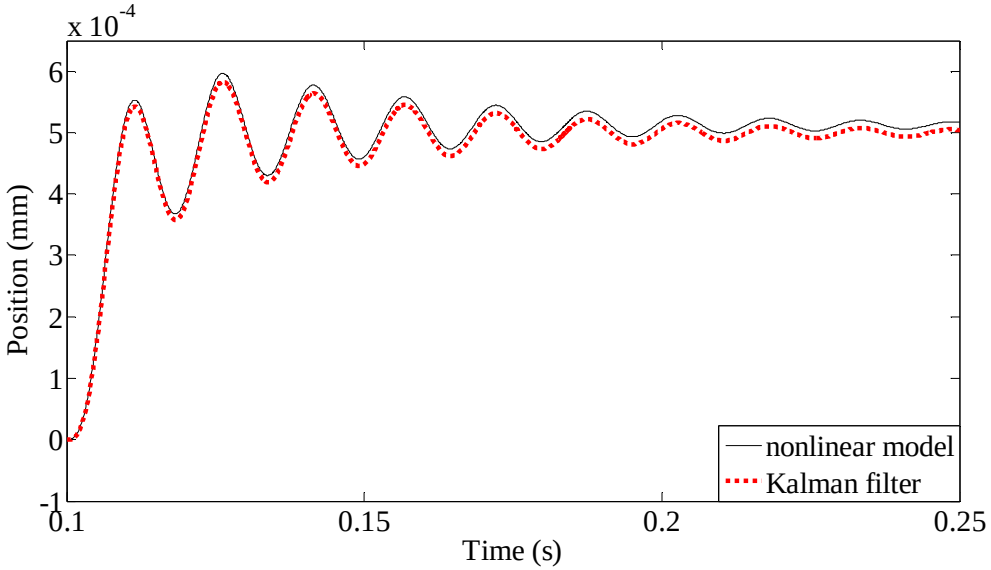

Figure 2.14: Kalman filter, position estimate in response to a step input level of 0.01 V

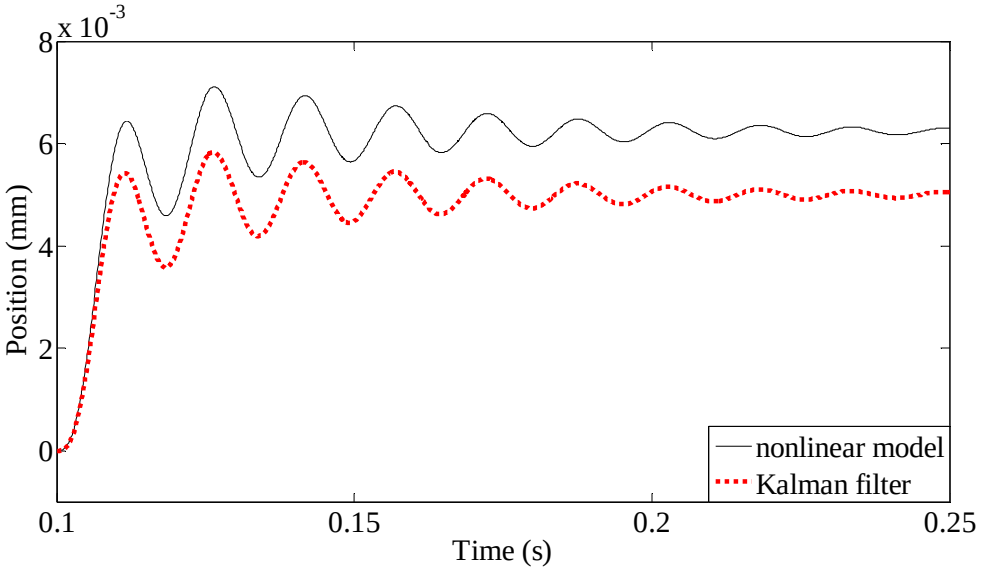

Figure 2.15: Kalman filter, position estimate in response to a step input level of 0.1 V

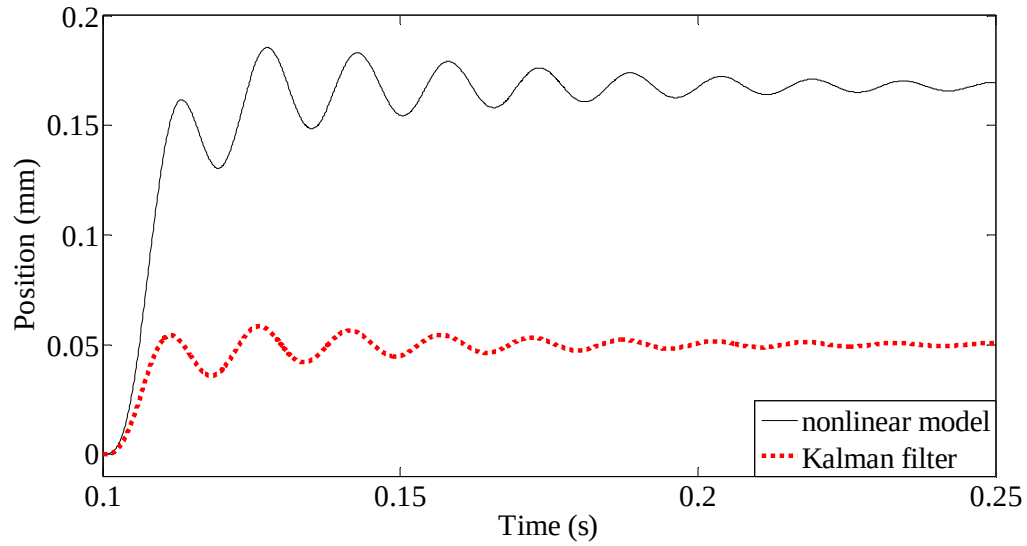

Figure 2.16: Kalman filter, position estimate in response to a step input level of 1.0 V

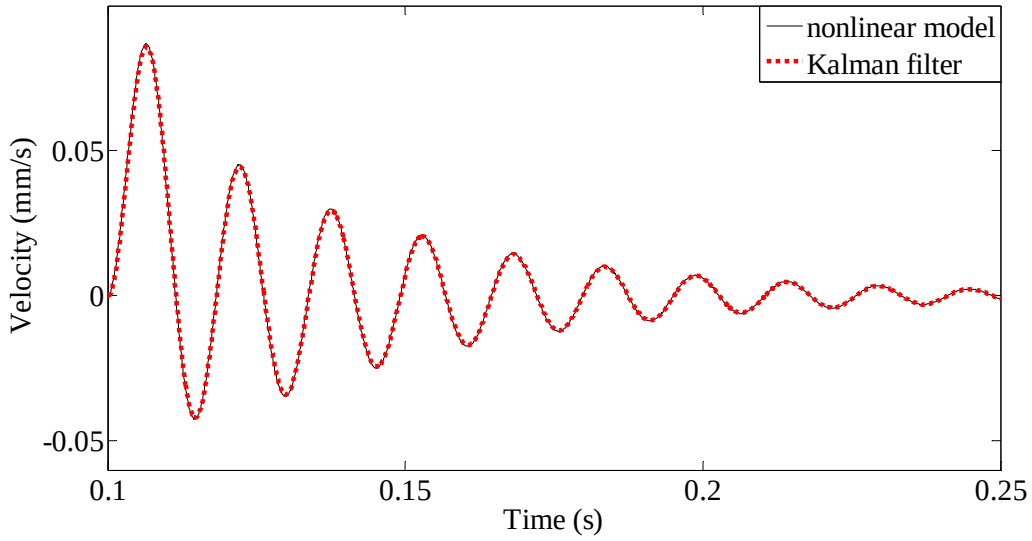

Figure 2.17: Kalman filter, velocity estimate in response to a step input level of 0.01 V

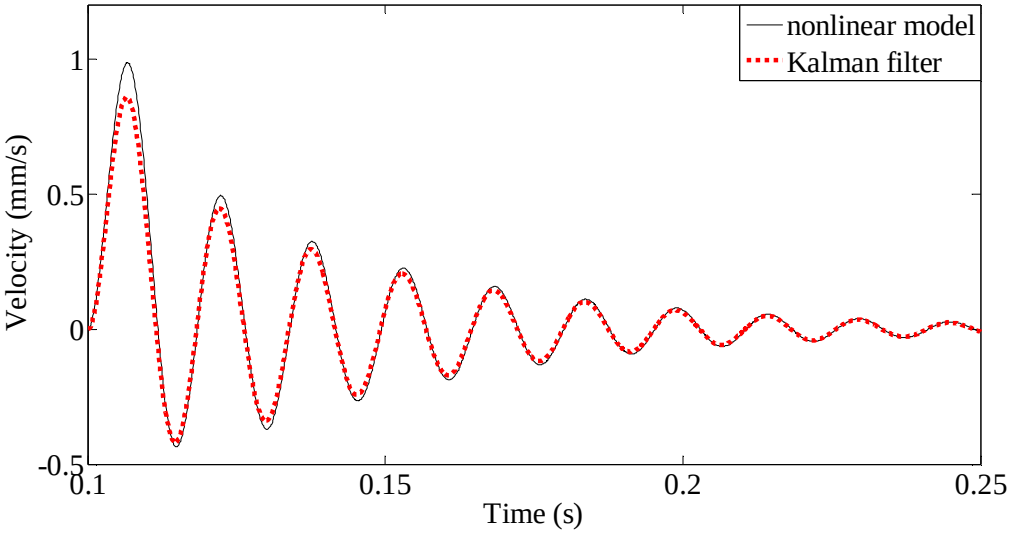

Figure 2.18: Kalman filter, velocity estimate in response to a step input level of 0.1 V

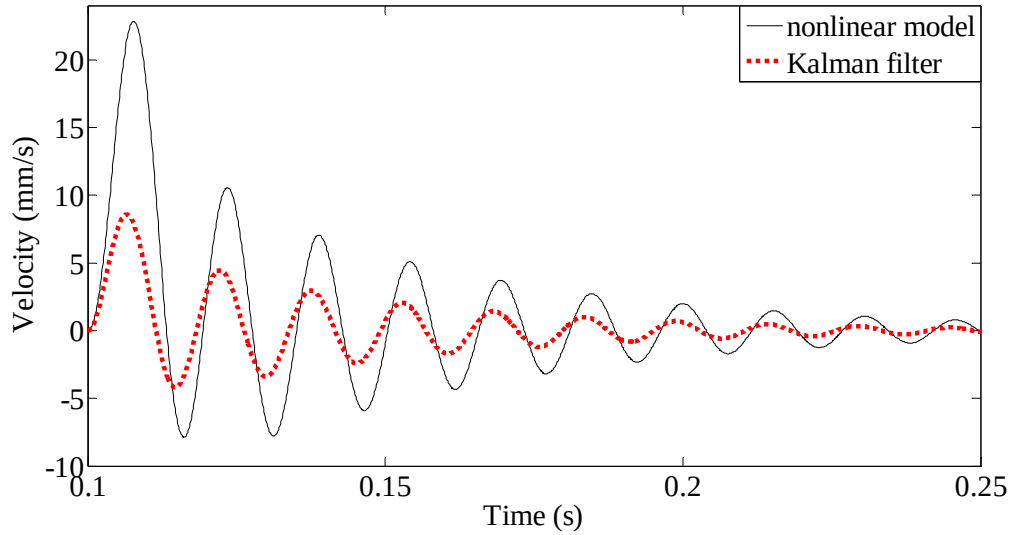

Figure 2.19: Kalman filter, velocity estimate in response to a step input level of 1.0 V

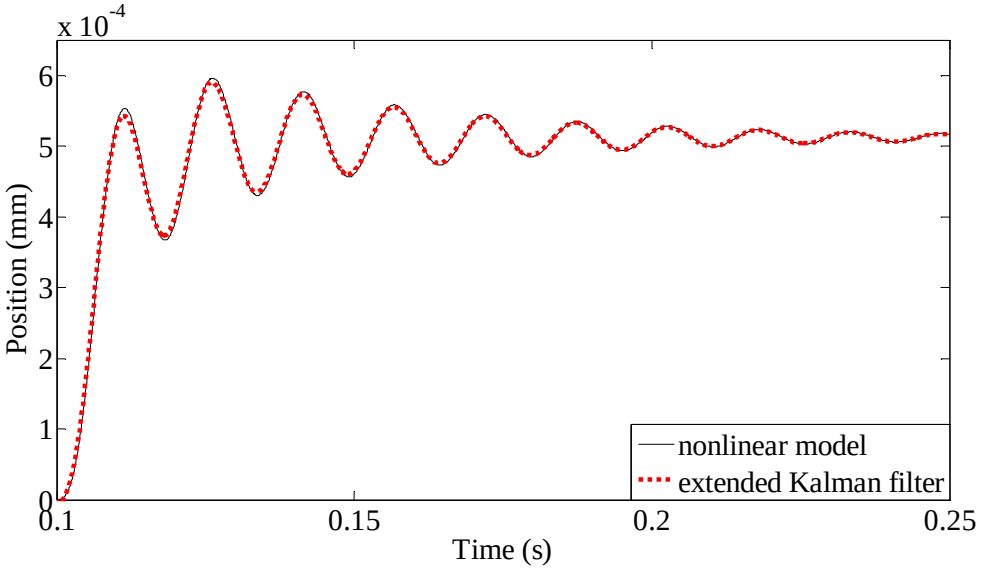

Figure 2.20: Extended Kalman filter, position estimate in response to a step input level of 0.01 V

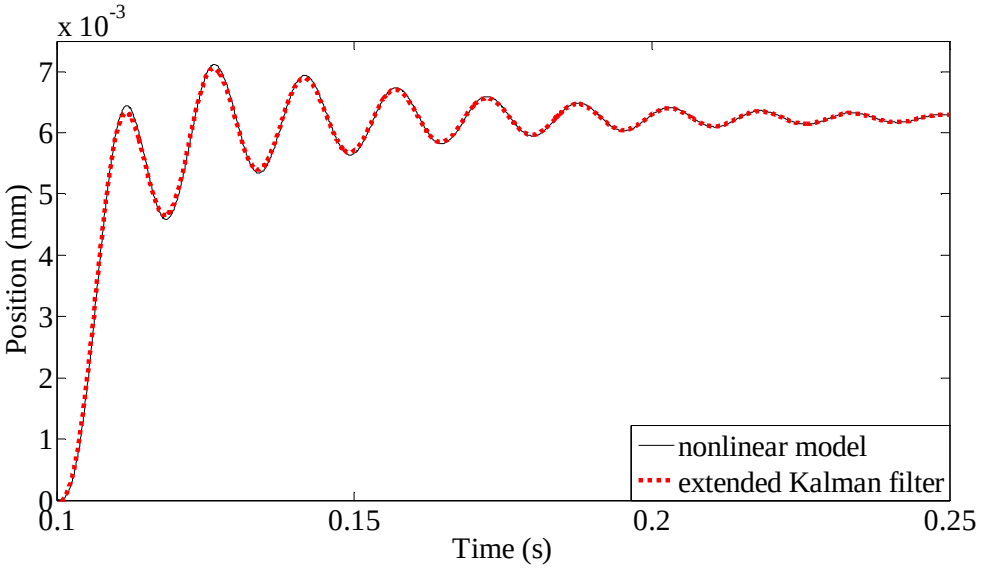

Figure 2.21: Extended Kalman filter, position estimate in response to a step input level of 0.1 V

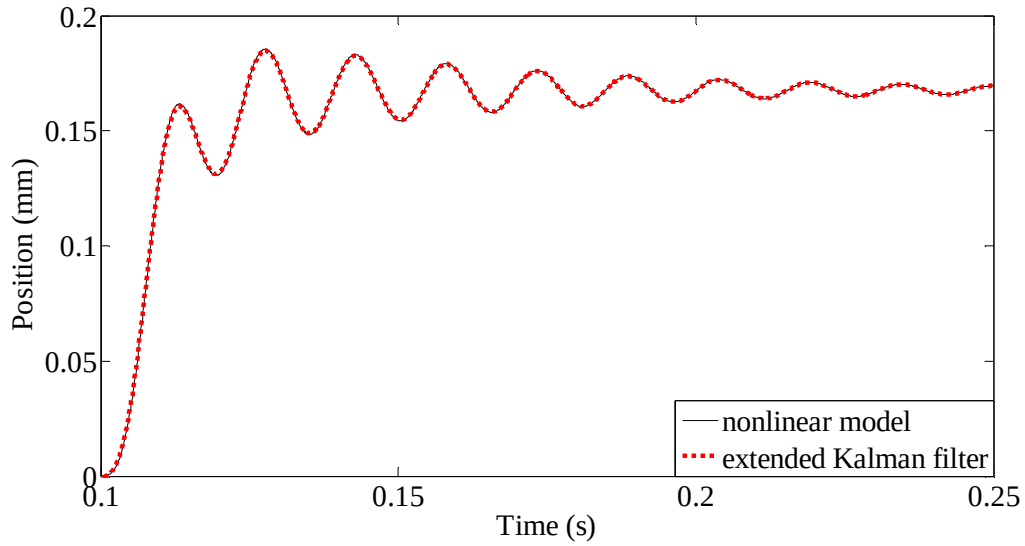

Figure 2.22: Extended Kalman filter, position estimate in response to a step input level of 1.0 V

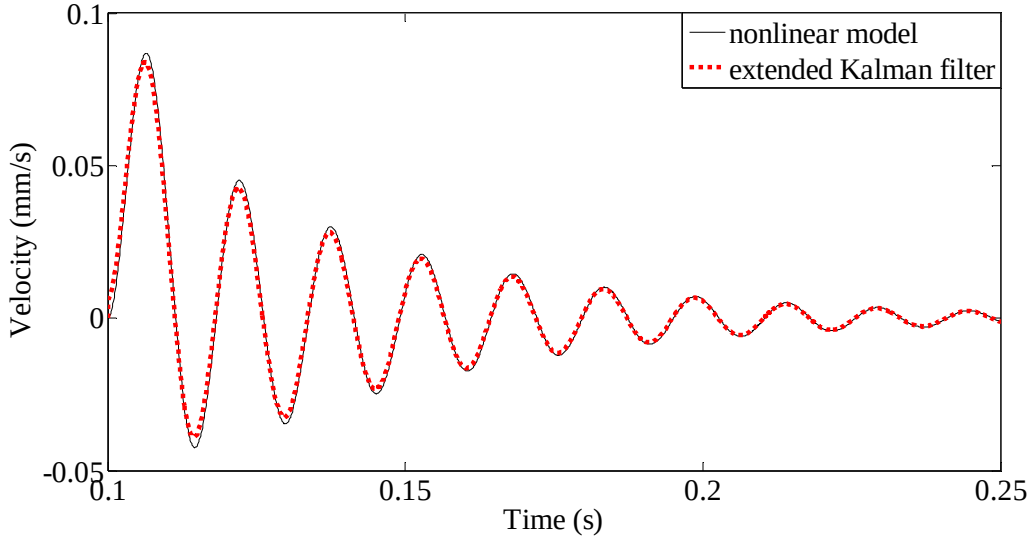

Figure 2.23: Extended Kalman filter, velocity estimate in response to a step input level of 0.01 V

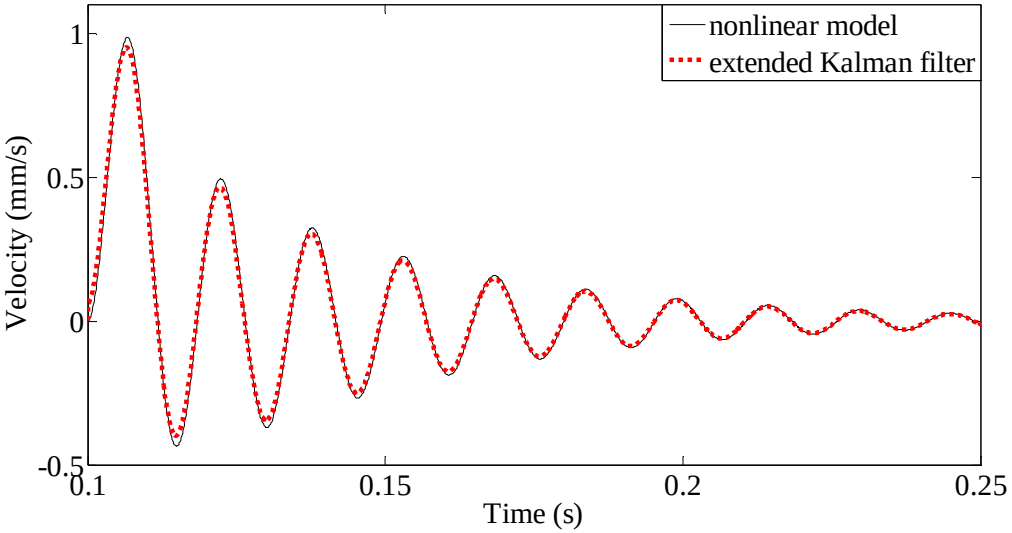

Figure 2.24: Extended Kalman filter, velocity estimate in response to a step input level of 0.1 V

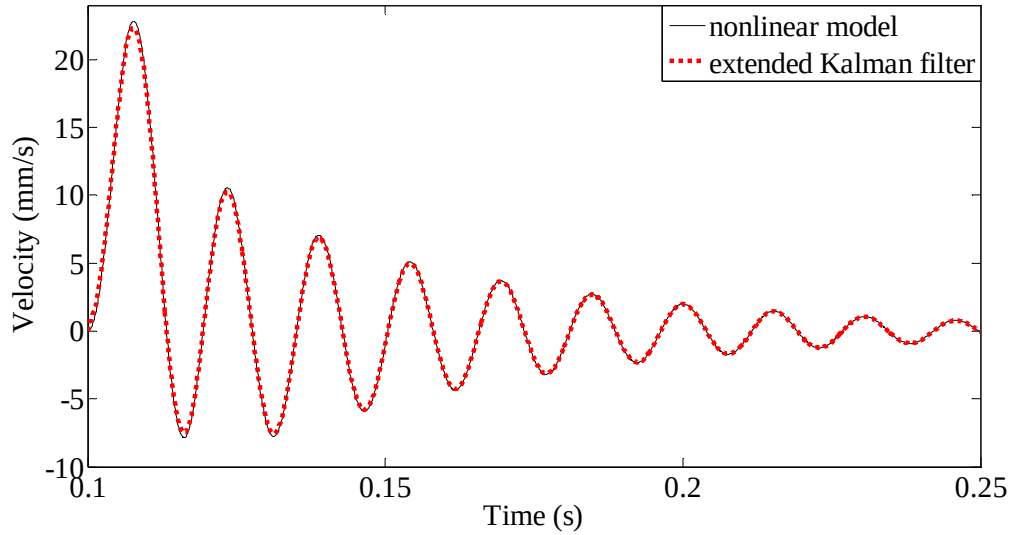

Figure 2.25: Extended Kalman filter, velocity estimate in response to a step input level of 1.0 V

2.5.3 Active Damping

The active damping results are displayed in Figures 2.26 and 2.28. During the implementation of the active damper, instability issues were encountered. It was determined that this was due to measurement noise affecting the velocity estimate before the step input. By keeping the active damper off during steady state and turning it on for transient inputs, this undesirable result was avoided. This noise induced instability problem may be eliminated by employing a low pass filter along with the active damping gain G. The addition of a low pass filter is left for future work.

At each step input level, the results show decreased peak-to-peak amplitudes and shorter settling times. Essentially, the amplitude and settling time became progressively smaller as the step input level was increased. In the real-world, peak-to-peak amplitudes and settling times are direct measures of the instabilities in the poppet position. The amplitude and settling time indicate the severity of the oscillations of the pilot poppet. Decreasing these indicators show that instabilities in the pilot poppet's position can be attenuated when the estimated velocity signal is used in an active damping scheme. The results also display a disadvantage of using this active damping scheme. For the position, the active damping scheme also decreased the rise time indicating that reduced oscillations come at the expense of system performance.

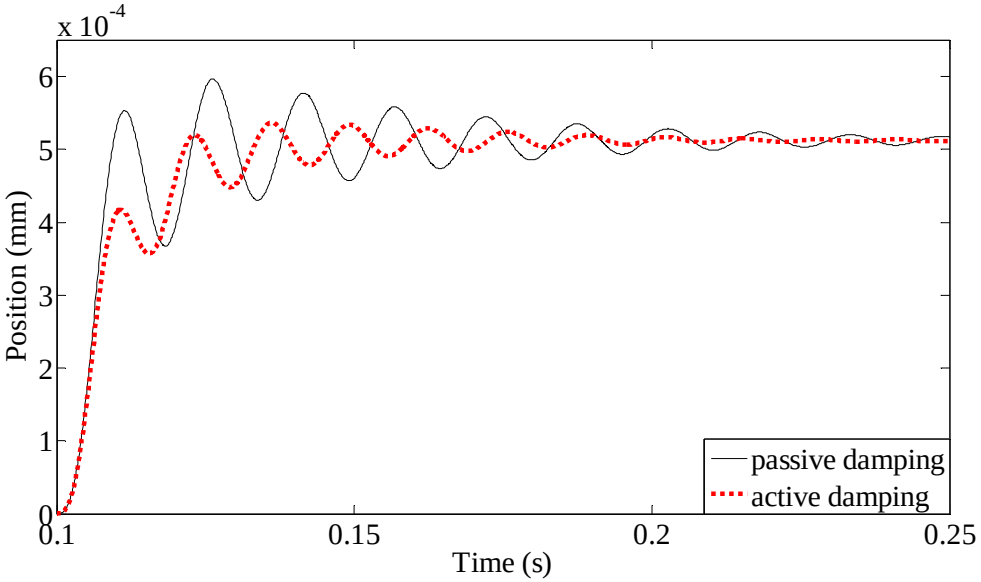

Figure 2.26: Active damping, position response to a step input level of 0.01 V

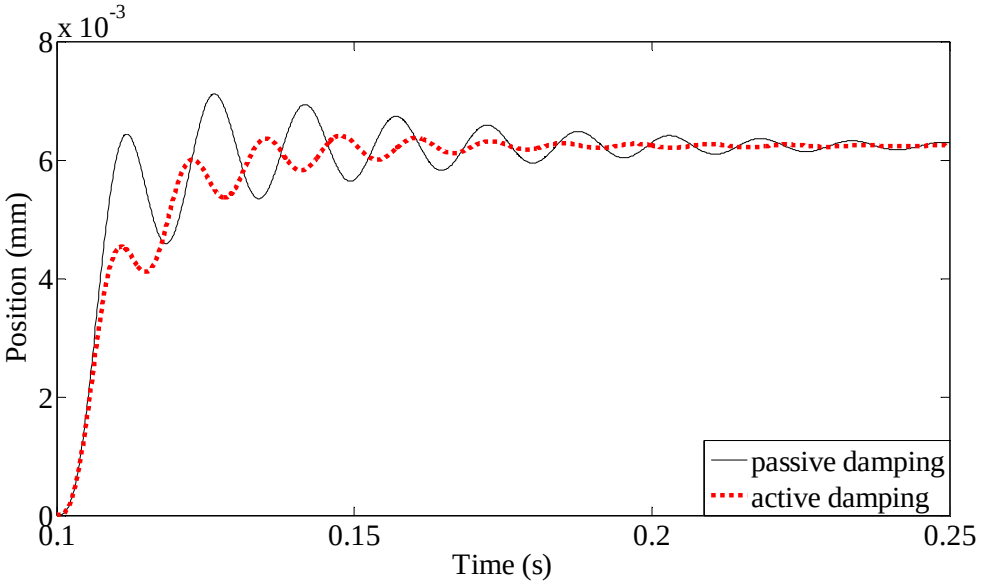

Figure 2.27: Active damping, position response to a step input level of 0.1 V

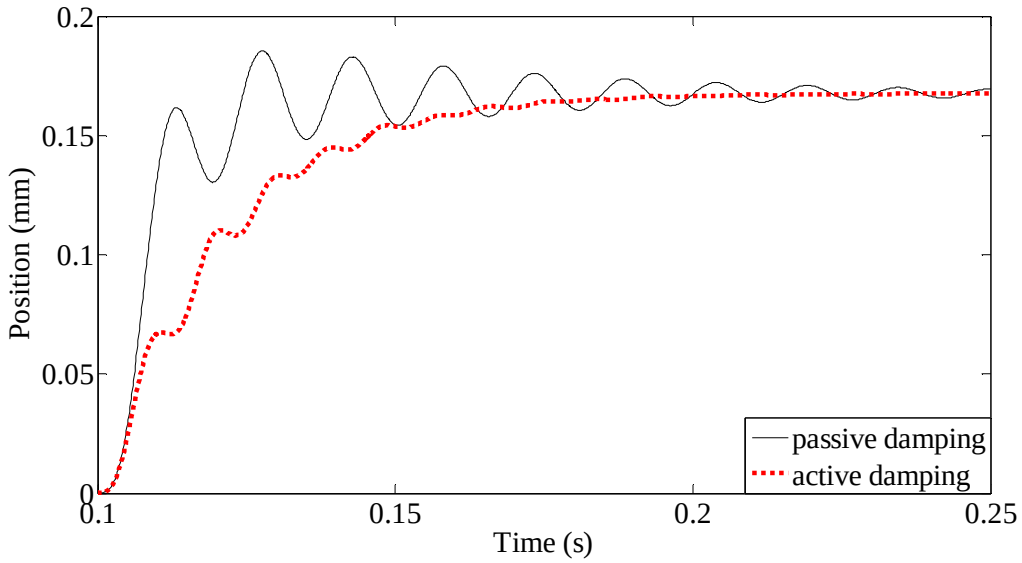

Figure 2.28: Active damping, position response to a step input level of 1.0 V

Since active damping involves the adjustment of the EMA input force on the pilot poppet, there is some concern that this will result in greater energy consumption. To examine the energy consumption, the solenoid power consumption ($P = Vi$) during active damping simulations was compared to the power consumption during passive damping simulations. As discussed above, the simplified model of the pilot poppet includes a tube in the pilot poppet mass to simulate pressure balancing and damping effects. To this point, the radius of the pilot poppet tube has been set at a value which promotes performance over damping. To simulate passive damping in the study of energy consumption, the pilot poppet tube radius was decreased to promote damping over performance. In order to obtain a proper energy consumption comparison, the pilot poppet tube radius was decreased until the position rise time equaled the position rise time with the active damping approach, Figure 2.29. Rise time is defined here as the time

it takes for the position to rise from ten percent of its steady-state value to ninety percent of its steady-state value.

In the results that follow, three damping cases will be referred to: two tube damping cases (large radius case and small radius case) and one active damping case. For the two tube damping cases, no active damping was included. For the large radius case the pilot poppet tube radius was set to 9e-4 m and for the small radius case the pilot poppet tube radius was set to 3.1 e-4 m. For active damping, the proportional damping scheme was used with a gain value of 0.23 V-s/m and the pilot poppet tube radius was set at 9e-4 m. A voltage step input of 1 V was used.

In Figure 2.29, it is shown that there is a transient difference in the rise of the position for the small radius case compared to the active damping case. The greater initial increase in the position from the active damping case is caused by the low, passive damping from the large radius pilot tube. The active damper/velocity controller responds with an initially small reaction to the velocity increase to attenuate the initial rise. Through the transient stage, the active damper slows the position rise to the point where the rise time is less than that for the large radius tube alone. Despite the transient difference, the active damping case and the small radius case have similar rise times, approximately 49.3 ms for the active damping case and 46.1 ms for the small radius case. In addition, the active damping case displayed no overshoot and a quick settling time.

Figure 2.30 shows that with tube damping, the solenoid inputs approximately the same power for both tube damping cases. Recall that, power is the product of the voltage and current. In the tube damping cases, the input voltage is the same. However, Eq. 2.6 and Eq. 2.5 show that because current is dependent on the position of the pilot poppet,

current is not the same in both tube damping cases. It turns out that the position dependence of the current only has a small effect. A significant zoom-in on the power plots, Figure 2.31, shows the influence of the position dependent current on the power.

To compare the two tube damping cases, consider Eq. 2.48

$$\Delta P = \frac{\dot{x} 8 \mu L_p A}{\pi R^4} \tag{2.48}$$

From Eq. 2.48 It can be seen that, at the onset of the EMA force input, for $R_a > R_b$:

$$\left\{ \begin{array}{l} \dot{x}_a \approx \dot{x}_b \\ \Delta P_a = \dfrac{\dot{x}_a 8 \mu L_p A}{\pi R_a^4} \\ \Delta P_b = \dfrac{\dot{x}_b 8 \mu L_p A}{\pi R_b^4} \end{array} \right\} \Rightarrow \Delta P_a < \Delta P_b$$

In the case of the smaller radius tube (R_b) relative to the case of the larger radius tube (R_a), there was a greater, initial build-up of pressure in the control volume relative to the pilot volume. By examining the effect of the ΔP term on the mechanical dynamics (Eq. 2.1), it can be seen that the greater pressure build-up in the smaller diameter case acted to dissipate kinetic energy faster than the case with the larger diameter tube. The faster dissipation of kinetic energy explains the observation of slower rise time, and no overshoot in the smaller radius case compared to quicker rise time, overshoot and oscillations in the larger radius case.

For active damping, the voltage and thus energy input is continuously adjusted by the velocity feedback term at the voltage input. In the small radius case, approximately the same amount of energy was input to the system as was input during the large radius case. In the small radius case, the hydraulic fluid removed the excess energy to produce

the desired response. In contrast to the small radius case, in the active damping case, only the energy that was needed to produce the response was input to the pilot poppet mass. Figure 30 shows that, with the simplified model and a proportional active damping scheme, active damping is more efficient than passive damping accomplished by tube flow in the pilot poppet. In Figure 30, power consumption for active damping is always less than the other cases. Therefore, less work is needed to accomplish the same task of moving from one position to another.

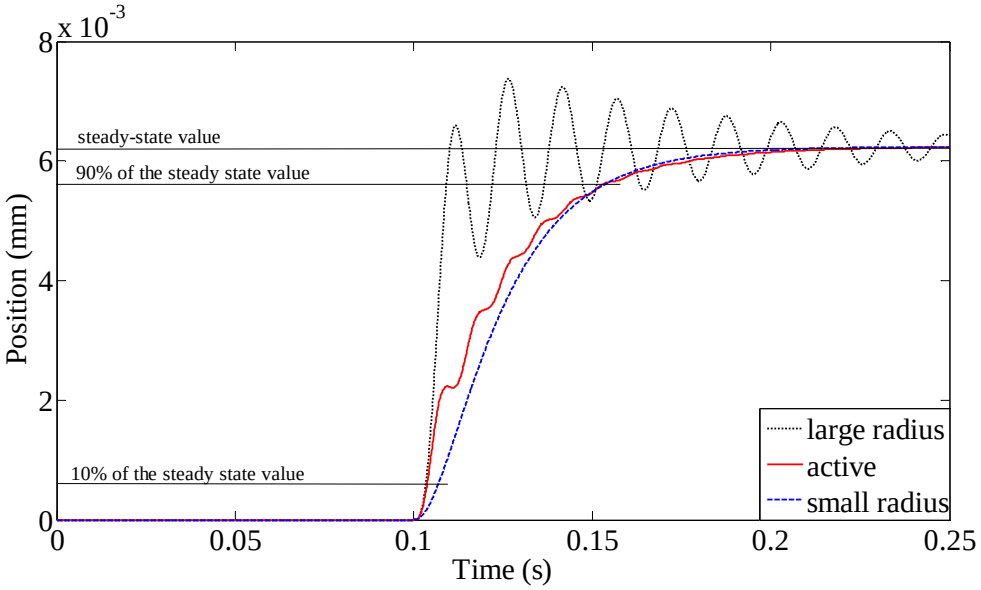

Figure 2.29: Position response to a 1.0 V step input level with a large radius pilot poppet tube, small radius pilot poppet tube, and active damping

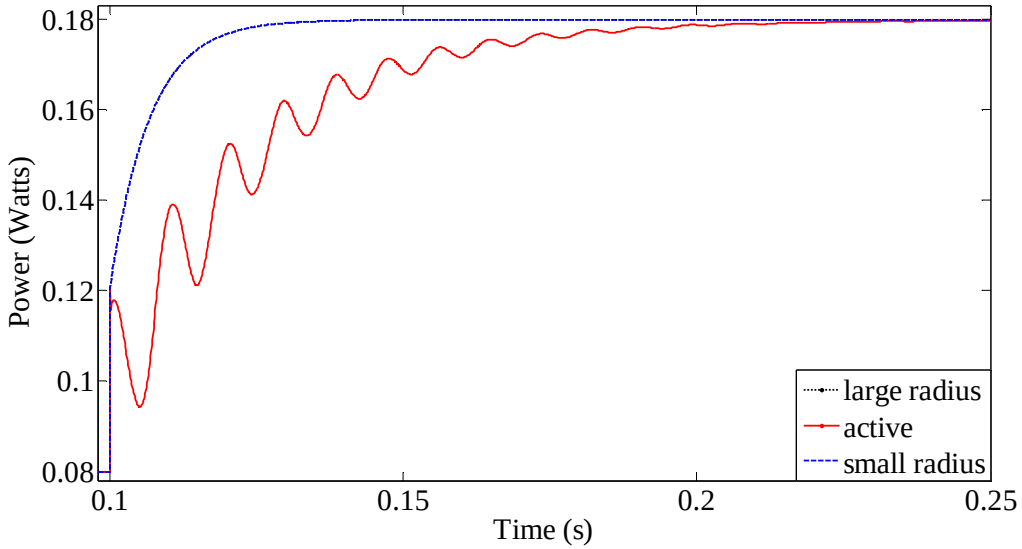

Figure 2.30: EMA power consumption at 1.0 V step input level with a large radius pilot poppet tube, small radius pilot poppet tube, and active damping

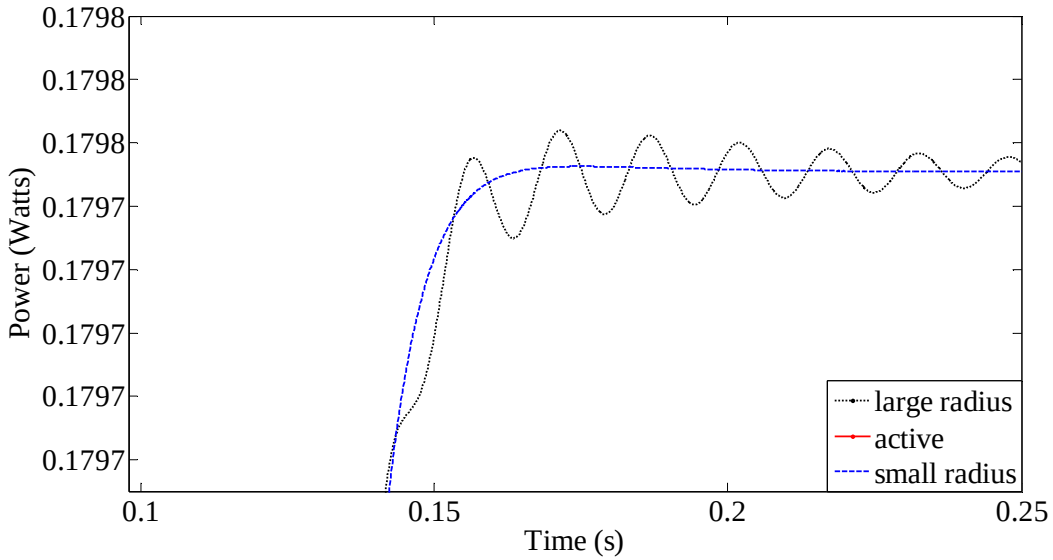

Figure 2.31: EMA power consumption at 1.0 V step input level with a large radius pilot poppet tube and small radius pilot poppet tube (zoom-in)

CHAPTER 3

SOLENOID DAMPING OF THE PILOT POPPET – EXPERIMENTAL STUDY

3.1 INTRODUCTION

A mechanical setup was developed as a testbed for the solenoid EMA. The EMA testbed was less complex than a hydraulic setup and so was less complex to develop and operate. In addition, the testbed allowed the characteristics of the solenoid to be determined in isolation. However, because the testbed isolated the solenoid EMA, the self-sensing actuator concept and active damping approach could not be validated in the proper hydraulic environment. Complete validation of the self-sensing actuator concept and the active damping approach applied to the MU valve would require a complete hydraulic circuit which includes an MU valve prototype. The complete validation with the MU valve prototype was planned. However, EMA characteristics prohibited the complete validation. The results presented below detail the experimental study conducted on the solenoid EMA testbed and discuss the impact of these results on future testing.

3.2 EXPERIMENTAL SET-UP

The physical configuration of the testbed is diagrammed in Figure 3.3. The solenoid is fixed to a table top and the solenoid pin (solenoid extension in contact with

the armature) is in contact with the LVDT rod. On the other end of the LVDT rod is connected the LVDT's magnetic core (also called an armature). The armature is free to translate within the LVDT housing providing measurement of the solenoid armature's displacement. The LVDT is fixed to the same table as the solenoid.

To provide a load for the solenoid, the setup is spring loaded with the forced-feedback metering poppet valve spring. To do this, a sleeve contacts the LVDT housing and has a washer fixed to the end not in contact with the LVDT housing (end-stop washer). A spring is placed concentric with the LVDT rod and in contact with the end-stop washer. This allows the spring to be compressed against the end-stop washer while allowing the LVDT rod to pass through. On the end of the spring not in contact with the end-stop washer is another washer (compression washer). The compression washer is fixed by the rod pin and a slight pre-compression of the valve spring such that it translates with the LVDT rod. This allows the solenoid armature to compress the spring when it is energized and be returned to its initial position when the current is removed. Return is important since the solenoid only forces in one direction. Figure 3.4 shows a photo of this testbed.

The solenoid EMA, pictured in figure 3.1, was supplied by Caterpillar®. It produces a push force with no internal return mechanisms. From the specifications sheet, the EMA has a maximum current rating of $2\ A$. The EMA can travel approximately 3 mm from one end-stop to the other end-stop. For the EMA used in the present study, a coil resistance of $5.1\ \Omega$ was measured at room temperature. Table 3.1 displays the steady-state, input-output values from the specifications sheet for the EMA and Figure 3.2 contains a simple diagram of the solenoid's primary components.

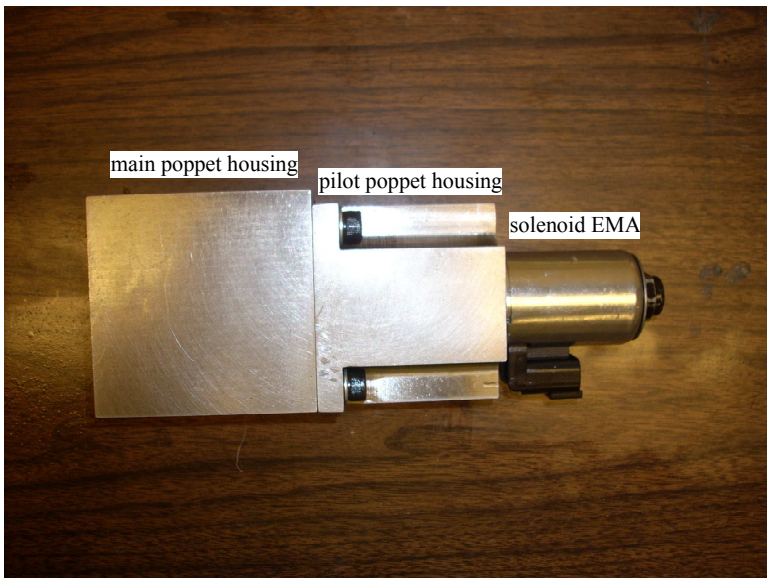

Figure 3.1: Forced-Feedback metering poppet valve prototype

stroke (mm)	force (N)	current (A)
0.8	45.0±2.5	1.5
0.8	10.0±2.5	0.5
2.2	45.0±2.5	1.5
2.2	10.0±2.5	0.5

Table 3.1: Steady-State input-output values for the solenoid (from the specifications)

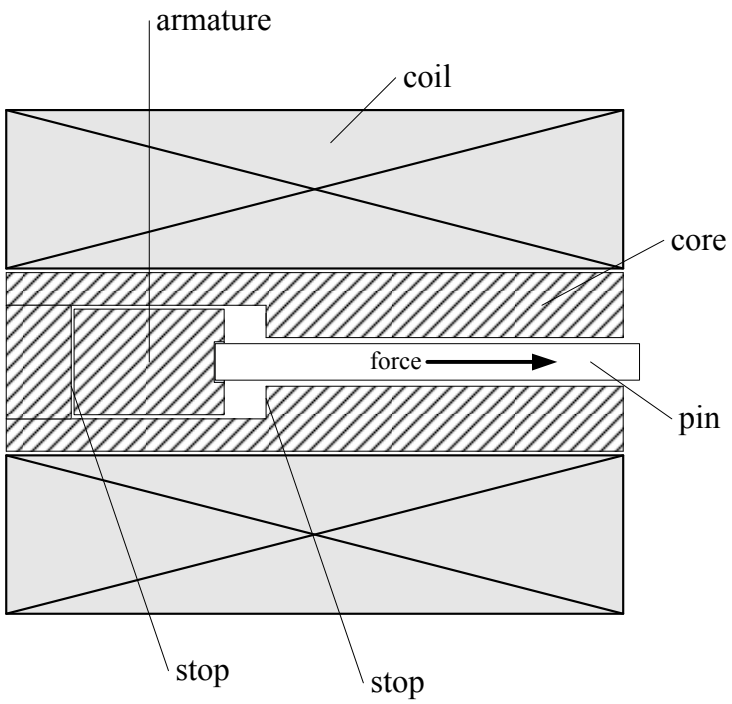

Figure 3.2: Primary solenoid components

3.2.1 Instrumentation

The testbed was instrumented to measure the voltage across and current through the solenoid coils and the position of the solenoid armature. Data was collected via a PC based data acquisition system which was also used for real time control of the solenoid, Figure 3.5.

Data acquisition and control was accomplished using Matlab/Simulink® with Real-time Windows Workshop software. For hardware, the National Instruments® PCI-6036E card with the SCB-68 shielded I/O connector block were used. This was all implemented on a desktop PC which executed both the roles of host and target computer. The sampling period was set to 0.1 ms. The analog input channels were set for differential input.

The solenoid EMA was controlled using an Advanced Motion Controls® Brush type PWM servo amplifier. The amplifier accepted a 24 VDC driver input from a voltage source and a ±10 VDC reference input from the DAQ system. Internally, the reference voltage was converted into a reference current which was the reference input to a feedback current controller. This controller then modulated the duty cycle/pulse width of a voltage pulse wave such that the average current in the coils of the EMA was equal to the reference current value. This is summarized in Figure 3.6. Actual current feedback was accomplished using a current control system which is integrated within the PWM amplifier. The affect of this current controller will be displayed in the results.

A 1 Ω resistance was placed in series with the solenoid coils as the initial approach to current sensing. It was determined that the resistance change and thus heating due to ohmic losses was too large. This caused the resistance value to increase during testing which introduced additional uncertainty and inaccuracy. Thus, current sensing was accomplished using the F.W. Bell® NT-5 magneto-resistive current sensor. This instrument offered relatively excellent accuracy, linearity, and a low sensitivity to temperature. In addition, it contained an extremely low load resistance of less than 2 mΩ. This translated to less than 0.235% of the solenoid resistance.

DC voltage measurements are generally straight forward given the nature of the DAQ system. In the present research the DC voltage was in the form of a 36 kHz pulse wave with amplitude of 24 VDC. This presented two challenges to the DAQ system. First, the input range of the AI channels was ±10 VDC. Second, with the system setup to perform data acquisition and control, it had an effective maximum sampling frequency of 10 kHz. In dealing with these challenges a voltage divider was used to obtain a

measurable magnitude and an analog, low-pass Butterworth filter with a cutoff frequency of 2.5 kHz was used to provide an average voltage signal. The voltage divider had an experimentally determined ratio of approximately 1:3 and due to a small amount of inductance of the resistors the voltage divider was found to behave like a filter with its own cutoff frequency of approximately 30 kHz.

To measure the displacement of the armature, a Linear Variable Differential Transformer (LVDT) was used. The Omega LD620-2.5 was chosen for its small range (±2.5 mm), DC input/output characteristics, and low friction characteristics. This LVDT features a guided core and an unusually large bore-to-core clearance which helps prevent misalignment and friction. The full testbed, with instrumentation, is pictured in Figure 3.7.

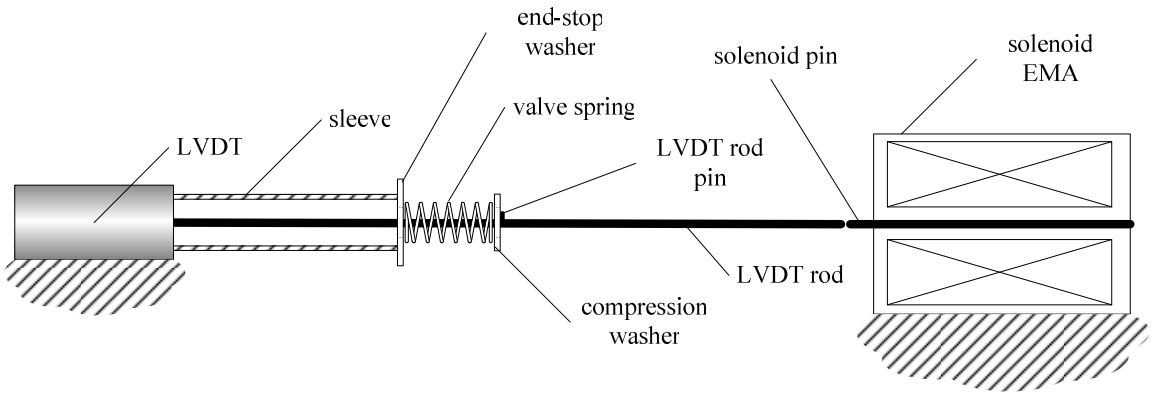

Figure 3.3: Solenoid EMA testbed

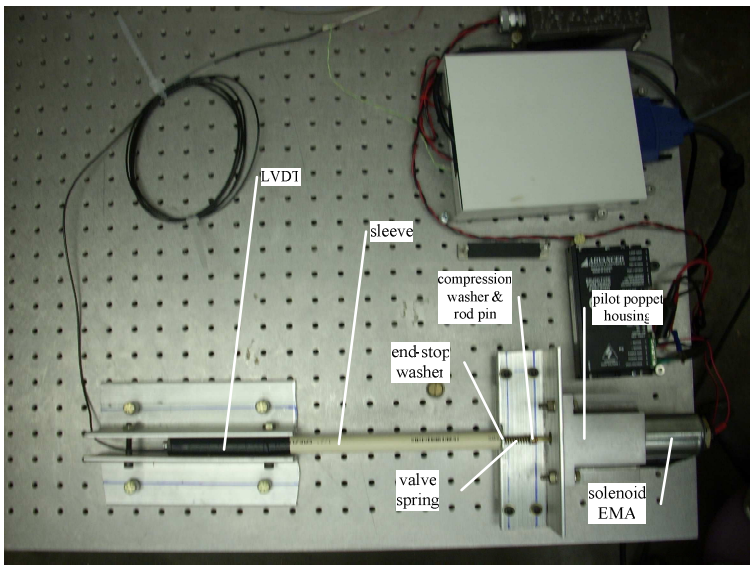

Figure 3.4: Solenoid EMA testbed

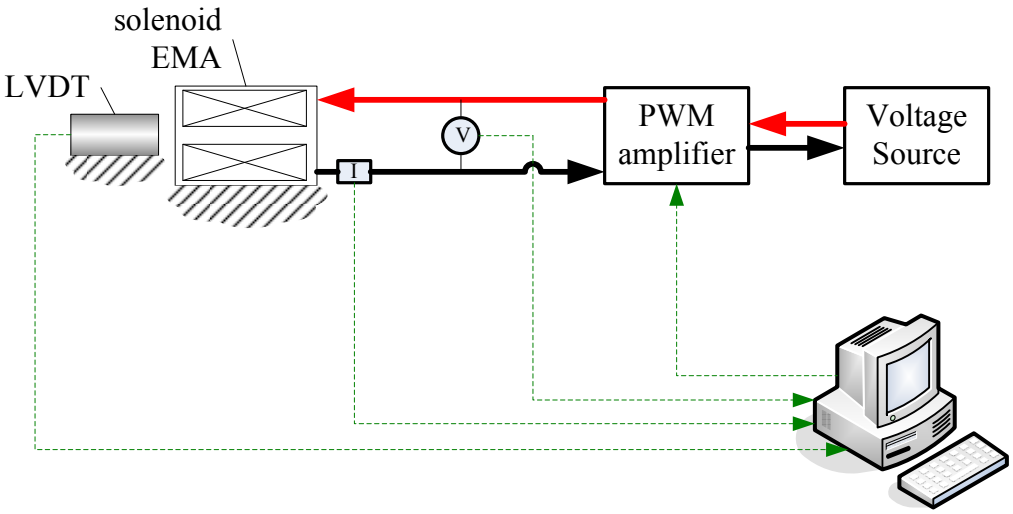

Figure 3.5: Solenoid EMA testbed instrumentation

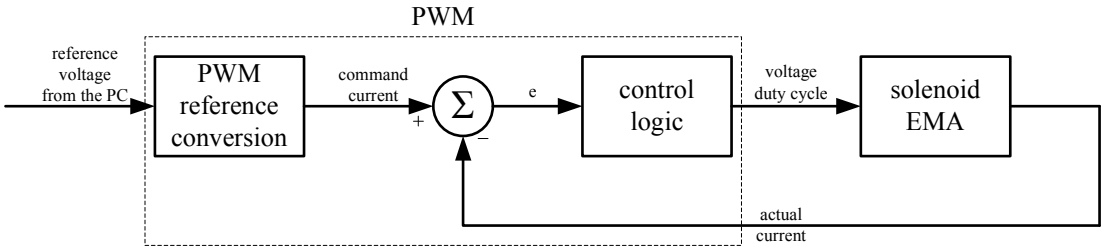

Figure 3.6: Current control via a pulse width modulation amplifier

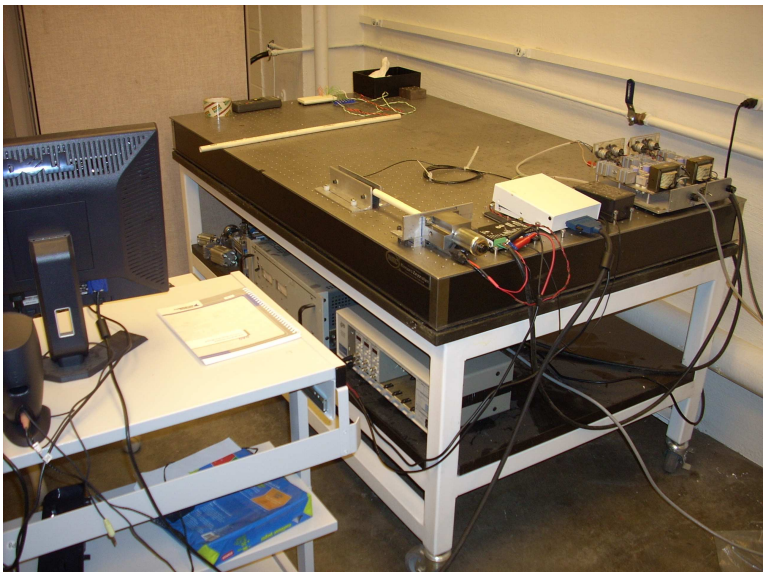

Figure 3.7: Solenoid EMA testbed with instrumentation

3.3 RESULTS AND DISCUSSION

To parameterize the model, the relationship between position and inductance must be determined. Initially, the assumption was made that the inductance for the EMA used in the present study has the same dependence on position as the EMAs used in the work

conducted by Yuan and Li [17-19]. Making such an assumption allowed for the use of the functional form of the inductance, Eq. 2.4, used in the model and for the use of the self-calibration procedure also developed by Yuan and Li [17]. The self-calibration procedure was developed to empirically determine the parameters (β_2 and d) of the functional relationship between position and inductance. The functional relationship was derived from first principles and intended to represent the position dependent inductance of a typical, commercially available EMA.

$$L(x_p) = \frac{\beta_2}{d + x_p} \tag{2.4}$$

As discussed in chapter 2, the electrical dynamics of the solenoid are modeled using an RL circuit. KVL applied to such a circuit produces a first order ODE. In the purely electrical case, simple model identification techniques could be used to identify the *L* parameter. However, in the present case, the *L* parameter changes with the position of the armature. Using the functional relationship of Eq. 2.4, Yuan and Li proposed a self-calibration procedure to determine the β_2 and *d* parameters. The self-calibration procedure offers certain advantages over conventional procedures: it takes seconds to conduct, it can be conducted with the solenoid in its normal operating set-up and it only requires hardware for measuring current, voltage, and positions of the end-stops of the solenoid. These advantages made the procedure attractive for the present study.

To conduct the procedure, the measurements of voltage, current, and position were monitored during a step input to the system. To determine the change in flux linkage, the voltage and current measurements were used in the following equation:

$$\Delta\lambda_e = \int_{t_k}^{t_{k+1}} \left(-i_e R_{e,2} + V_e\right) dt \,, \tag{3.1}$$

where $\Delta\lambda_e$ is the change in the flux linkage of the EMA used in the present study (Wb), i_e is the current of the EMA used in the present study (A), $R_{e,2}$ is the current resistance of the EMA used in the present study (Ω), and V_e is the voltage across the coil of the EMA used in the present study (V). Equation 3.1 was derived from Equation 2.3, which is restated here in a form that is applicable to the EMA used in the present study:

$$\dot{\lambda}_e = -i_e R_{e,2} + V_e \tag{3.2}$$

where λ_e is the flux linkage of the EMA used in the present study (Wb).

The procedure is based on the comparison of $\Delta\lambda_e$, determined from Eq. 3.1, with $\Delta\lambda_e$, determined algebraically. The calculation for determining $\Delta\lambda_e$ algebraically proceeds as follows. An equation for λ_e is derived by substituting Eq. 2.4 into Eq. 2.2 ($\lambda = Li$) to obtain the following equation:

$$\lambda_e = \frac{\beta_{e,2}}{d_e + x_p} i_e \tag{3.3}$$

where $\beta_{e,2}$ is the composite (β) solenoid parameter for the EMA used in the present study (see Appendix B.4) (H-m) and d_e is the composite (d) solenoid parameter for the EMA used in the present study (see Appendix B.4) (m). Equation 2.2 is restated for the EMA used in the present study as:

$$\lambda_e = L_e i_e \tag{3.4}$$

where L_e is the inductance for the EMA used in the present study (H).

If the $\beta_{e,2}$ and d_e parameters are known, then Eq. 3.3 can be used with the current and position measurements at t_k and t_{k+1} to determine the flux linkage at these time instants ($\lambda_{e,k}$ and $\lambda_{e,k+1}$). Finally, the change in flux linkage is calculated as $\Delta\lambda_e = \lambda_{e,k+1} - \lambda_{e,k}$. Since $\beta_{e,2}$ and d_e are not known, estimates ($\hat{\beta}_{e,2}$ and $\hat{d}_e$) can be chosen to produce an estimate of the change in the flux linkage:

$$\Delta\hat{\lambda}_e = \hat{\lambda}_e(t_{k+1}) - \hat{\lambda}_e(t_k) = \frac{\hat{\beta}_{e,2}}{\hat{d}_e + x_p(t_{k+1})} i_e(t_{k+1}) - \frac{\hat{\beta}_{e,2}}{\hat{d}_e + x_p(t_k)} i_e(t_k) \tag{3.5}$$

The parameters can be determined by minimizing the objective function ($\bar{J}$), Eq. 3.6.

$$\bar{J}(\hat{\beta}_{e,2}, \hat{d}_e) = \left[\hat{\lambda}_e(t_{k+1}) - \hat{\lambda}_e(t_k) - \Delta\lambda_e\right]^2 \tag{3.6}$$

To increase the accuracy of the parameters determined, data from *N* steps was collected and the objective function in Eq. 3.7 minimized.

$$J(\hat{\beta}_{e,2}, \hat{d}_e) = \sum_{k=0}^{N-1}\left[\hat{\lambda}_e(t_{k+1}) - \hat{\lambda}_e(t_k) - \Delta\lambda_e\right]^2 \tag{3.7}$$

In using the self-calibration procedure in the present study, the input to the PWM was a 2 Hz square wave with an offset of 3.5 V and amplitude of 1 V. The test duration was 12 s. The results are plotted in Figures 3.8 – 3.12. The voltage (V_e), current (i_e), rate of change of flux linkage ($\dot{\lambda}_e$), and flux linkage (λ_e) are plotted with just 1 s of the 12 s test shown.

The voltage stepped up from a steady-state value of approximately 2.31 V to a steady-state value of approximately 4.32 V while the current stepped up from a steady-state value of approximately 0.465 A to a steady state value of approximately 0.87 A. Both variables consistently assumed these values at all 24 cycles. When viewing the

results for λ_e and $\dot{\lambda}_e$ it is important to remember that voltage and current are measured, whereas the rate of change of flux linkage is algebraically calculated, and flux linkage is the result of numerical integration. To verify the results, the steady-state form of Eq. 3.2 can be used. This is simply Ohm's law, $V_e = i_e R_{e,2}$, where $R_{e,2}$ was measured as 5.1 Ω. This information is also contained in Figure 3.10. At steady-state, this plot should tend to approach zero. This is approximately the case.

Qualitatively, the first observation to note is the large overshoots and undershoots in response to the steps up and down. The amplifier is designed to control current. Therefore, voltage and current overshoot are likely due to the performance of the current control system integrated into the amplifier (Figure 3.8 and 3.9).

The second important observation is the trends in the λ_e result, Figure 3.12. If $\dot{\lambda}_e$ has a nonzero average value at steady-state, it will manifest its self as a slope in λ_e. Closer inspection of the $\dot{\lambda}_e$ result, Figure 3.11, reveals a small negative average value at steady-state, accounting for the negative slopes in λ_e. Mathematically, this means that V_e does not exactly equal $i_e R_{e,2}$ at steady-state. This is likely due to slight measurement errors in V_e and i_e. In addition, $R_{e,2}$ was determined at room temperature and is assumed to be constant. In reality, heating of the coil occurs due to ohmic losses. This increase in temperature will increase the effective $R_{e,2}$ value. This can produce the type of error in $\dot{\lambda}_e$ that is seen in the results.

For parameterization, these errors can be ignored. Equation 3.7 indicates that it is the change in λ_e ($\Delta\lambda_e$) that is needed for the calculations. In the one second window,

$\Delta\lambda_e$ was determined to be approximately 0.0874 Wb. Finally, to complete parameterization, the armature displacement is needed. This result is shown in Figure 3.13. The armature steps from approximately 1.27 mm to 2.79 mm.

The optimization failed to uniquely converge (changed with small changes in the starting point). The failure to converge lead to the theory that the inductance of the EMA used in the present study does not have the same functional dependence on position as that used by Yuan and Li. To determine the functional dependence for the inductance in the present study, a more conventional system identification technique was conducted. This technique does not identify $\beta_{e,2}$ and d_e. It identifies the system time constant (τ). Once the time constant τ is determined, the inductance can be calculated using the following equation:

$$\tau_e = \frac{L_e}{R_{e,2}} \tag{3.8}$$

where τ_e is the time constant for the EMA used in the present study (s).

When parameterizing the model using system identification techniques, the position dependence of the inductance must be considered. To account for the position dependence of the inductance, the armature was fixed at regular, known positions across its range. Multiple model identification tests were run at each position.

τ_e can be determined directly using a step response or indirectly from the frequency response. τ_e was initially sought directly from the step response. The experimental approach was to give the model a step input and record its response. From this, the time constant can be determined as the time at which the response was 63% of the way from the initial value to the steady-state value. Figure 3.9 shows the system's

step response. As discussed above, the system responds to a step-up with an overshoot of the steady-state value. It was theorized that this was the result of the high gain current controller integrated into the PWM. To avoid this, the frequency response approach was conducted.

To conduct the frequency response approach, sine waves with frequencies ranging from 1 to 10 Hz stepping 1 Hz and 10 to 60 Hz stepping 10 Hz were supplied to the solenoid. The amplitude ratios ($\frac{A_{out}}{A_{in}}$, where A_{in} is the amplitude of the input sine wave (V) and A_{out} is the amplitude of the output sine wave (A)) were determined at each frequency and used to construct frequency response magnitude plots. From these plots, the bandwidth (ω_{bw}) was determined as the frequency at which the frequency response magnitude dropped 3 dB from the DC gain magnitude. Inductance (L_e) was calculated using the following equation:

$$\omega_{bw}(Hz) = \frac{1}{\tau_e * 2\pi} = \frac{R_{e,2}}{L_e}\frac{1}{2\pi}. \tag{3.9}$$

This procedure was conducted at three different positions relative to the pilot poppet housing: 0, 1.408 and 2.804 mm.

The data from the frequency response system identification tests are displayed in Figures 3.14 – 3.16 along with fitted first order magnitude curves. As a means of validation, the bandwidths from the EMA used in the present study were compared with the bandwidths of the solenoid used by Yuan and Li. Eq. 2.4 is plotted in Figure 3.17 with the parameters β_2 = 2.64e-4 H-m and d = 7.76e-3 m taken from the literature [19]. For the position (x_p), the position range of the EMA used in the present research was

used, 0 mm < x_p < 3 mm. The bandwidth for the solenoid used in the literature was determined using Eq. 3.9, where R = 0.5 Ω was also taken from the literature [19]. A plot of the position dependent bandwidth is shown in Figure 3.17. Similar to the results obtained in the present research, the bandwidth for the solenoid used by Yuan and Li is less than 10 Hz for the 0 to 3 mm position range.

In regards to model identification, the results from the present research show that at all three positions, the data is very close at all frequencies. From the fitted first order magnitude curves, the bandwidths at the positions of 0, 1.408, and 2.804 mm are 8.603, 8.543, and 9.181 Hz, respectively. Figure 3.18 shows the fitted first order magnitude curves plotted together for comparison.

Results from the present study were inconclusive in determining a functional relationship between position and inductance. The change in bandwidth with position was small, 0.578 Hz for a 2.8 mm displacement of the armature. It was theorized that the 0.578 Hz change in the bandwidth was a result of the displacement of the armature, instrumentation measurement error, or both.

If the observed change in bandwidth, in the present results, was the result of instrumentation measurement error, there is no functional relationship between armature position and inductance. The manufacture's specifications for the solenoid EMA used in the present study indicate that the electromagnetic force is independent of the armature's position, Table 3.1. It is possible that the EMA also has an inductance that is independent (or at least close to independent) of the armature's position. Examining Figure 3.19 reveals that the position independent EMA force does not adversely affect the self-sensing actuator concept. Examining Figures 3.19 and 3.20 together indicate that a

position independent inductance is detrimental to the self-sensing actuator concept. In Figures 3.19 and 3.20 it is graphically shown that for the system used in the present study, with the output defined as the current, observability is maintained as long as the inductance is dependent on position.

If the observed change in bandwidth, in the present study, was the result of both the change in armature position and instrumentation measurement error, the position dependence of the inductance is too weak to be determined with the instrumentation of the present setup. This case invokes a question: How weak can the relationship between armature position and inductance be before the system's observability is lost? The analysis and results presented next answer this question.

To test how weak the inductance's dependence on armature position can become before observability is lost, the rank of the observability test matrix (N) was calculated for increasingly weaker relationships between armature position and inductance. For the system to be observable, the observability test matrix must be full rank. For the present test, the reduced-order, simplified model was used and thus it was necessary for the observability test matrix to have a rank of 3. The observability test matrix was calculated as follows:

$$N = \left[\mathbf{C}_\rho{}^T \quad \mathbf{A}_\rho{}^T \mathbf{C}_\rho{}^T \quad \left(\mathbf{A}_\rho{}^T\right)^2 \mathbf{C}_\rho{}^T \right] \tag{3.10}$$

where $\mathbf{A}_\rho$ is the 3 x 3 system matrix of the linearized reduced order, simplified model and $\mathbf{C}_\rho$ is the 1 x 3 output matrix of the linearized reduced order, simplified model [23].

To conduct this analysis the functional relationship of the inductance used by Yuan and Li, Eq. 2.4, was approximated by a linear fit. A plot of the linear fit and

original functional relationship, Eq. 2.4, is displayed in Figure 3.21. The equation of the linear fit was determined to be:

$$L_l\left(x_p\right) = -3.1285x_p + 0.0335 \tag{3.11}$$

where L_l denotes the inductance determined by the linear fit (H), the units for the slope are $\frac{H}{m}$, and the unit for the y-intercept is H. To weaken the relationship between the inductance and the armature position, the slope of the linear fit was decreased. The force produced by the EMA was given the same equation as is shown in Figures 3.19 and 3.20. This equation was not altered as the slope was altered. The force equation is presented here as:

$$F\left(i, x_p\right) = \frac{\beta_2 i^2}{2\left(d + x_p\right)^2} \tag{3.12}$$

The observability test matrix was calculated in Matlab using the 'obsv' command and the rank was determined using the 'rank' command.

The results showed that the rank of the observability test matrix changed from 3 to 2 when the slope of the linear fit was decreased to a level between -1.0e-12 and -1.0e-13 $\frac{H}{m}$. Numerically, these values are approximately zero indicating that for the linearized, reduced-order, simplified model, the system is observable for any practical, linear relationship between armature position and inductance. A practical linear relationship is a linear relationship which can be measured. For the hypothetical, solenoid EMA, with a linear relationship between position and inductance having a slope of -1.0e-12 $\frac{H}{m}$, the relationship cannot be measured and therefore the relationship is not

practical. Furthermore, if the relationship can't be measured, the system is not observable in the practical sense. In summary, if the solenoid EMA has a measurable, linear relationship between armature position and inductance, simulations indicate that the system is observable.

In the present experimental study, a relationship between armature position and inductance could not be determined with any confidence. Without a functional relationship between inductance and armature position, the self-sensing actuator concept is not applicable. Without the self-sensing actuator concept, an active damping scheme would be very complex in practice. The inability to determine a relationship between position and inductance for the solenoid used in the present study prohibited further testing of the active damping approach

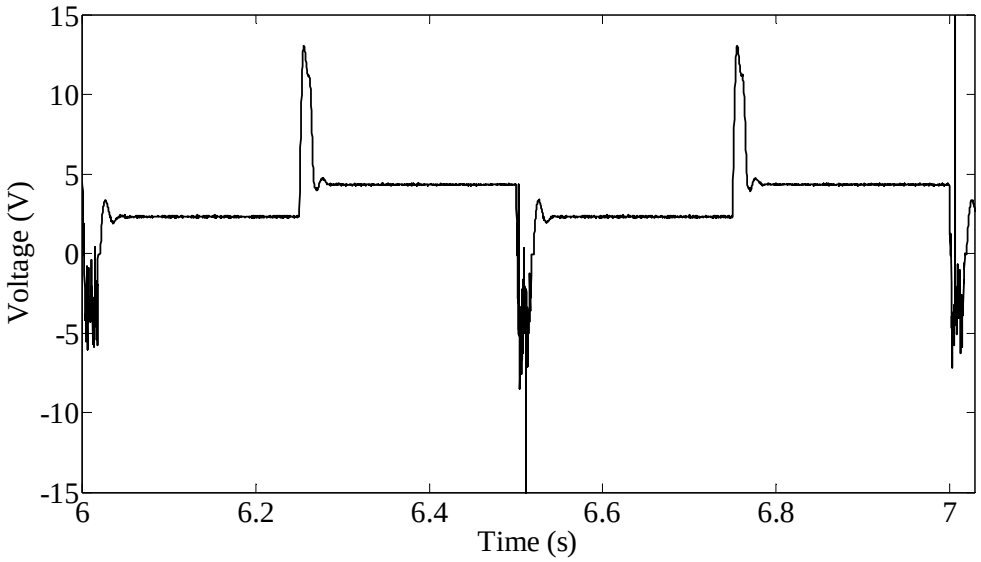

Figure 3.8: Parameterization test -measured voltage across the solenoid EMA coil

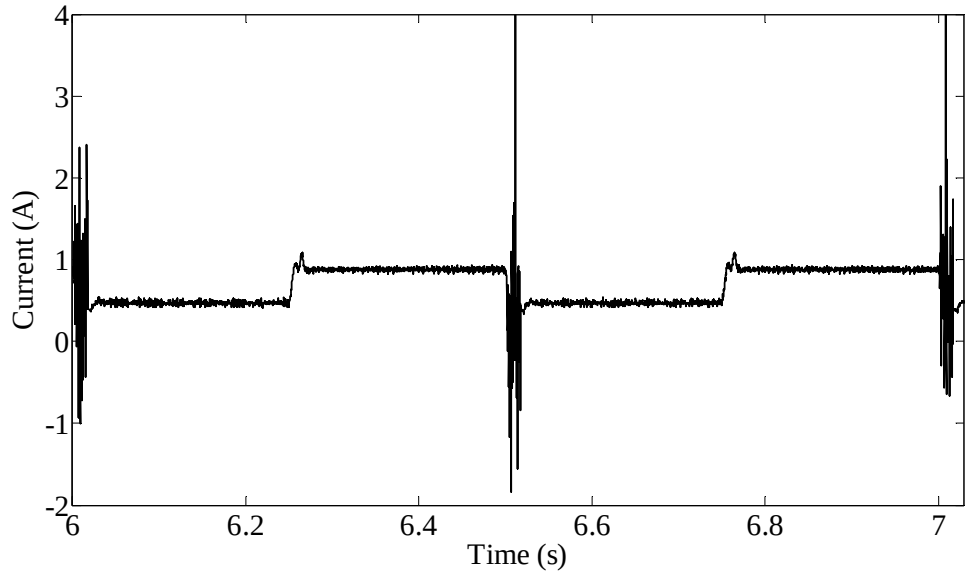

Figure 3.9: Parameterization test - measure current across the solenoid EMA coil

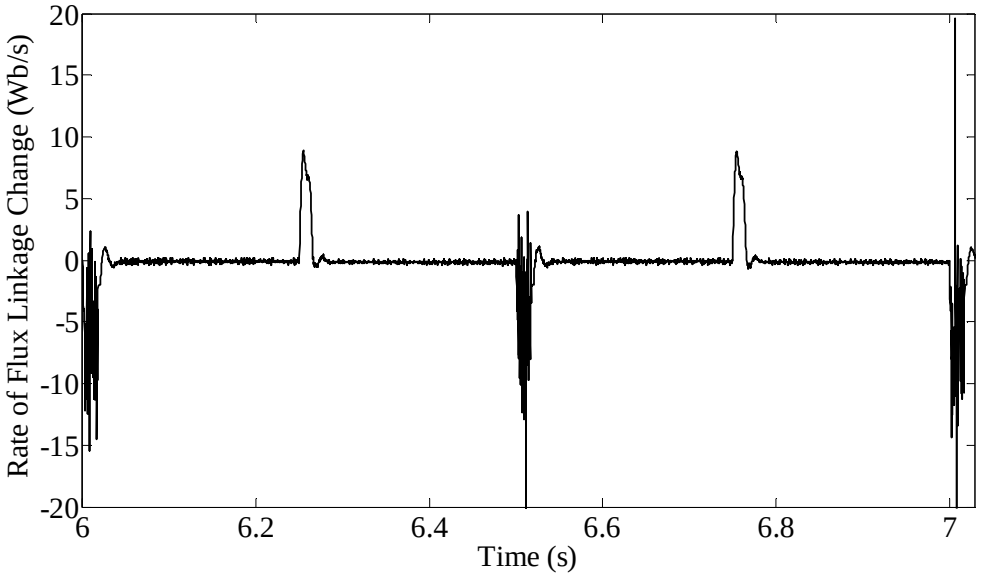

Figure 3.10: Parameterization test - calculated rate of change of the EMA flux linkage

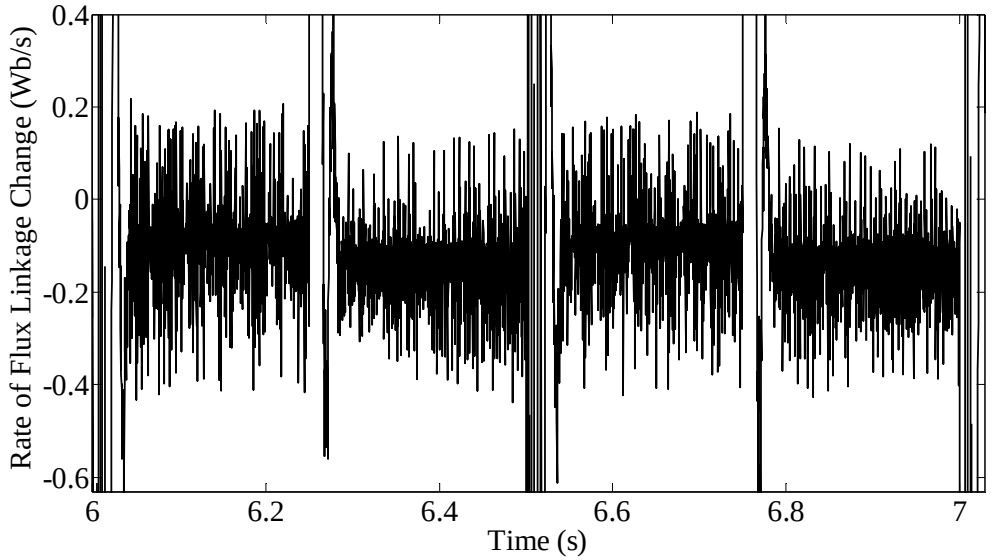

Figure 3.11: Parameterization test - calculated rate of change of the EMA flux linkage (zoom-in)

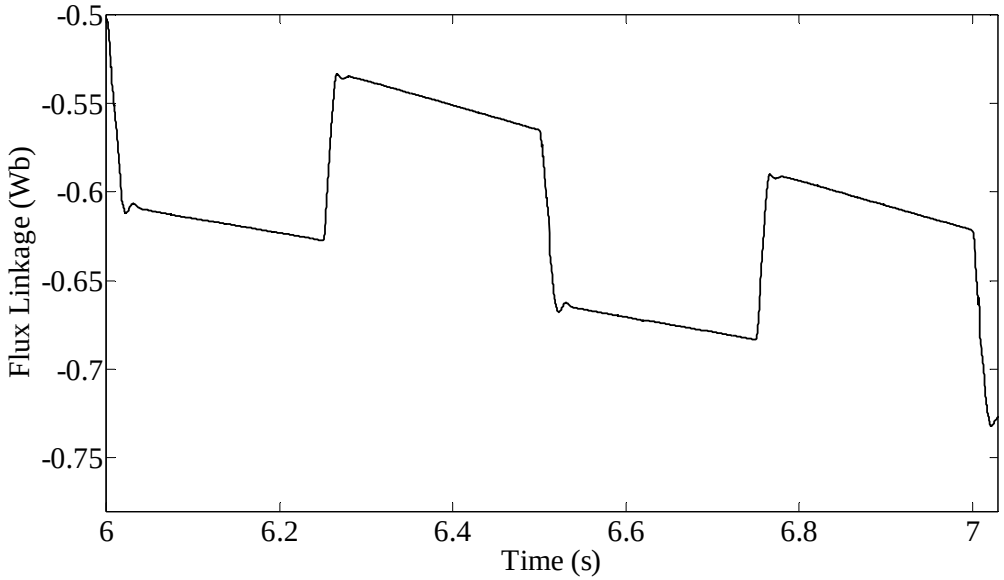

Figure 3.12: Parameterization test - calculated EMA flux linkage

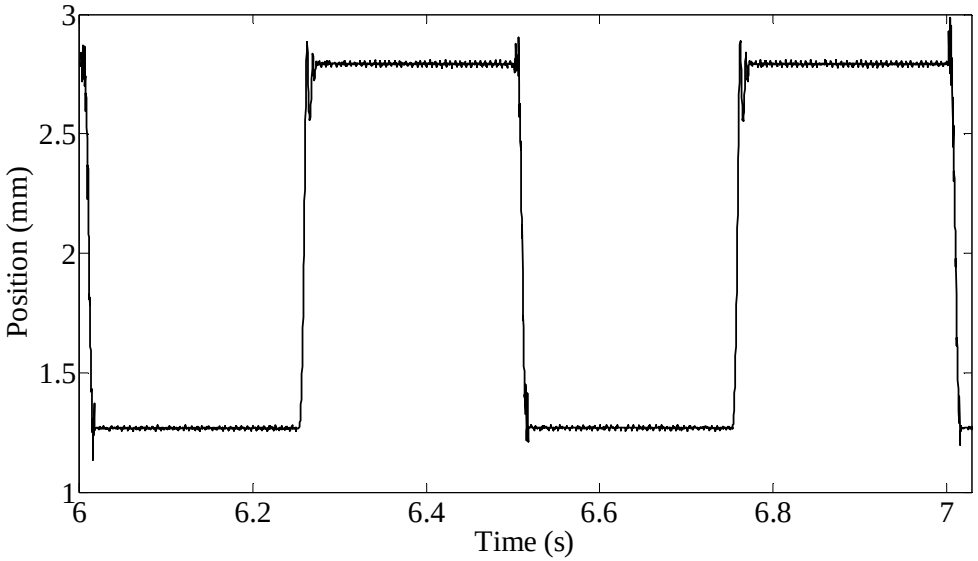

Figure 3.13: Parameterization test - armature position

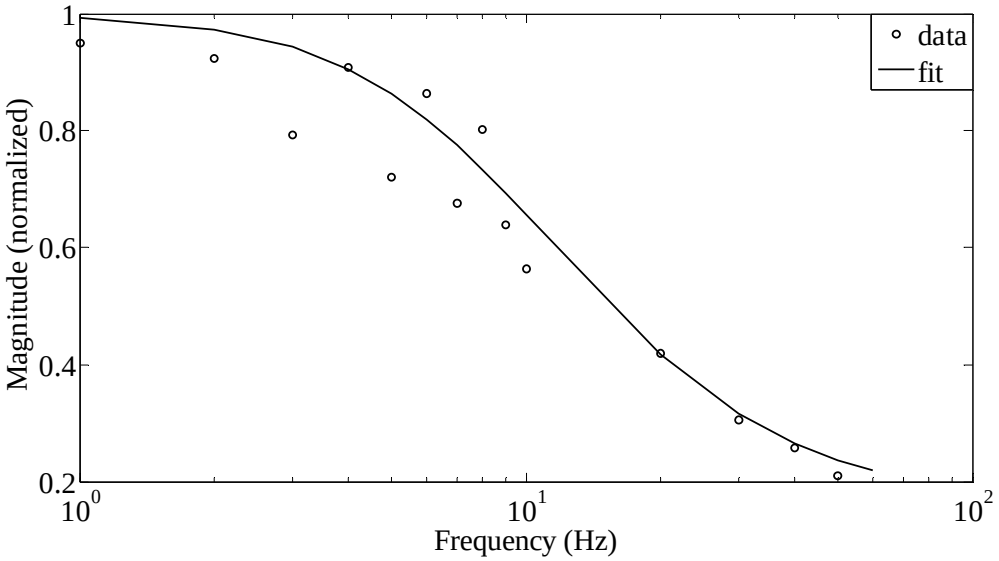

Figure 3.14: Magnitude frequency response magnitude at 0 mm

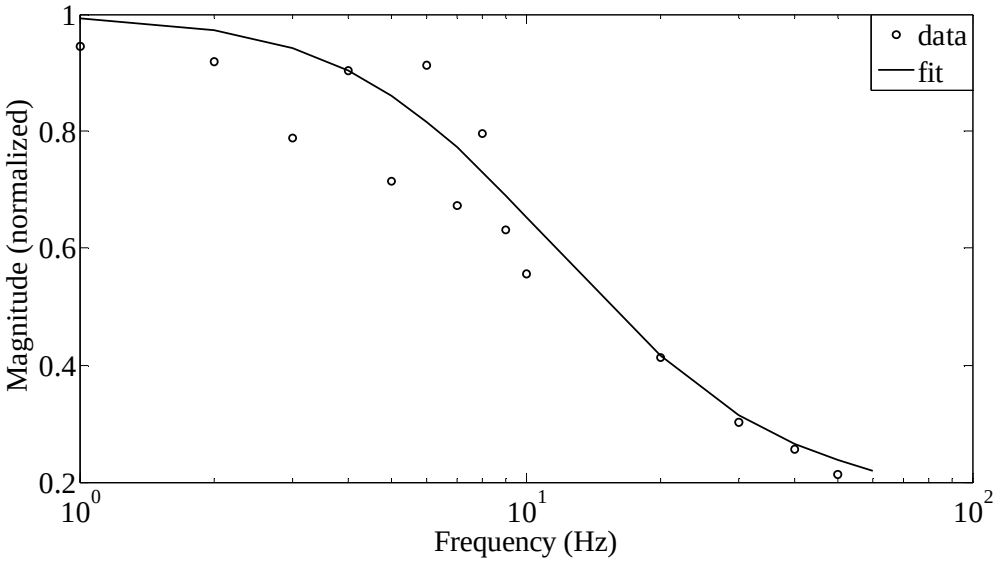

Figure 3.15: Magnitude frequency response magnitude at 1.41 mm

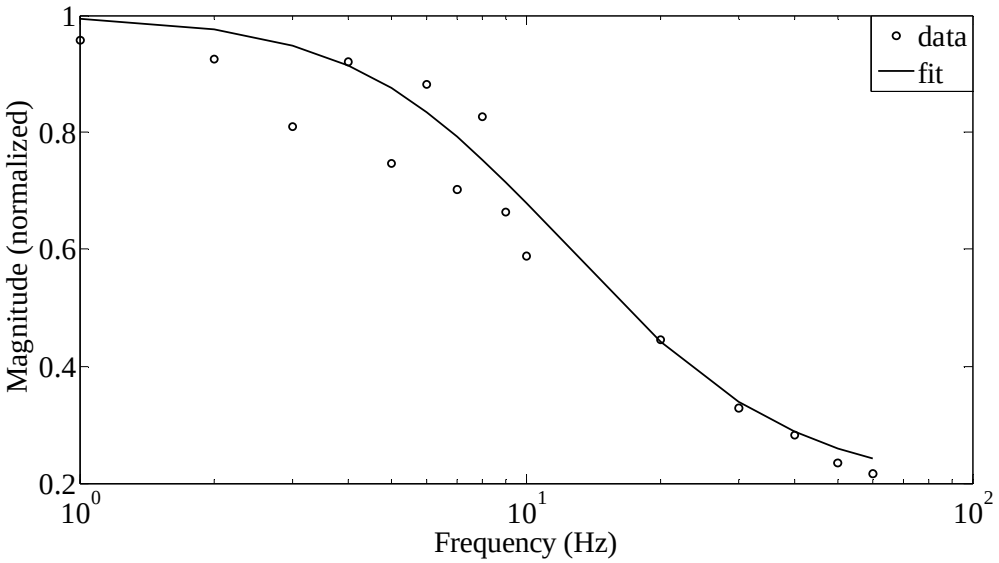

Figure 3.16: Magnitude frequency response magnitude at 2.80 mm

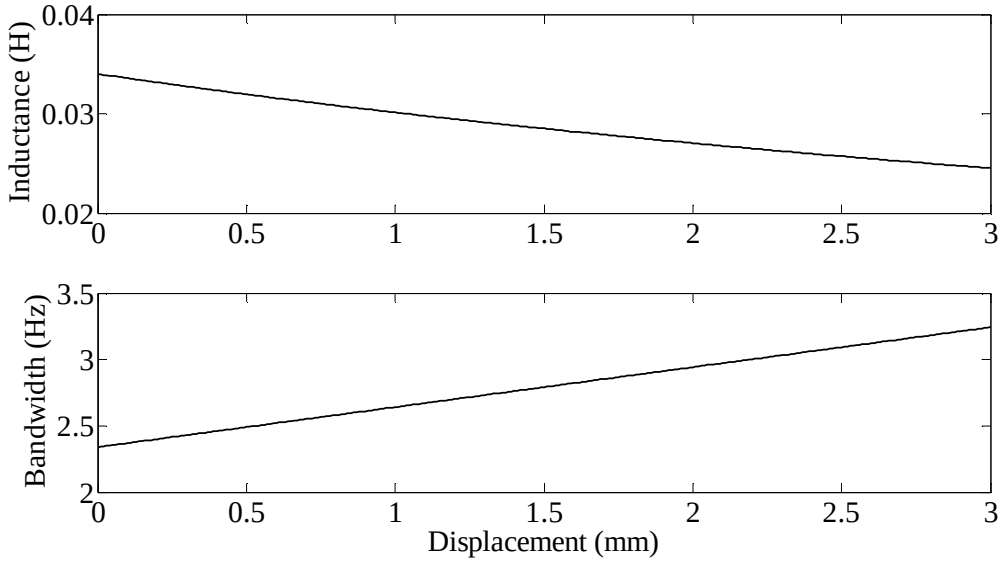

Figure 3.17: Inductance and bandwidth of the solenoid used by Yuan and Li [17]

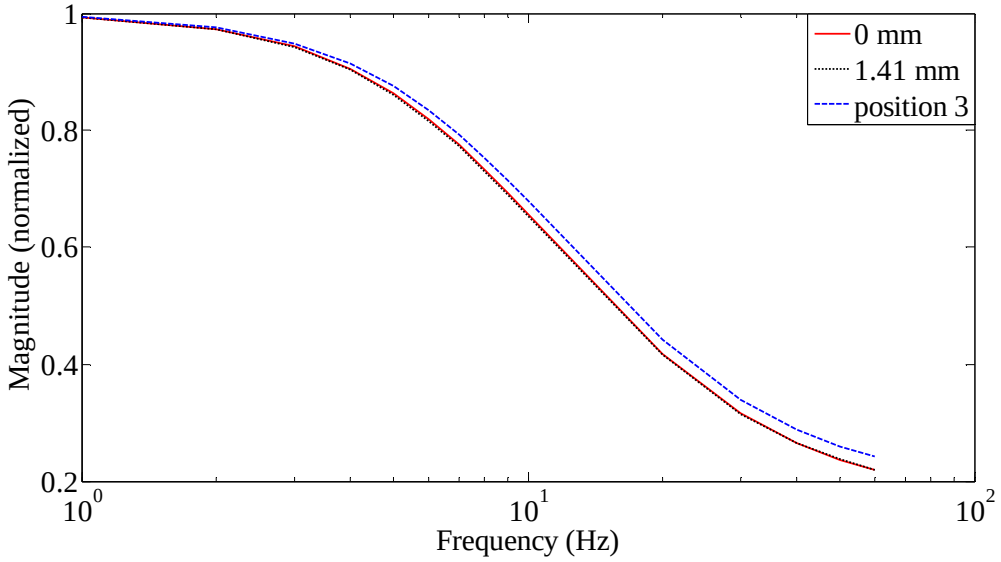

Figure 3.18: Magnitude frequency response comparison

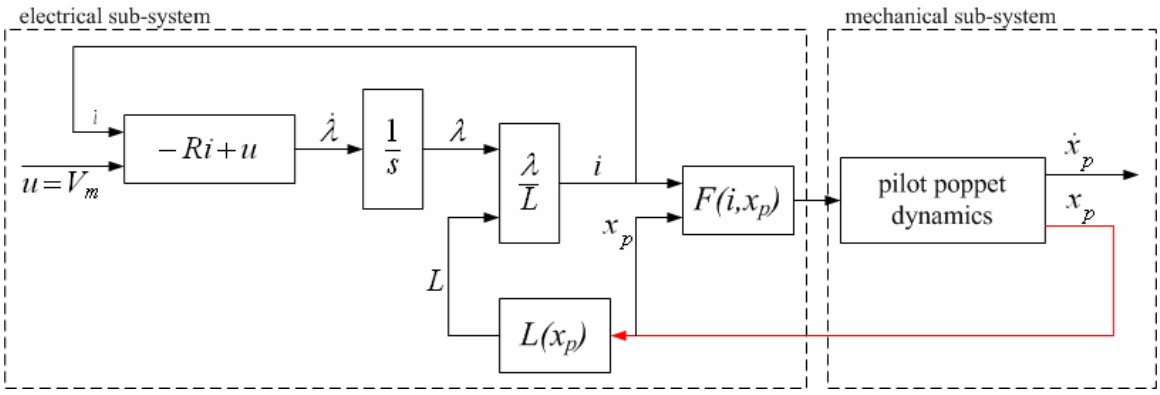

Figure 3.19: Simplified model, two-way coupling between the electrical and mechanical subsystems

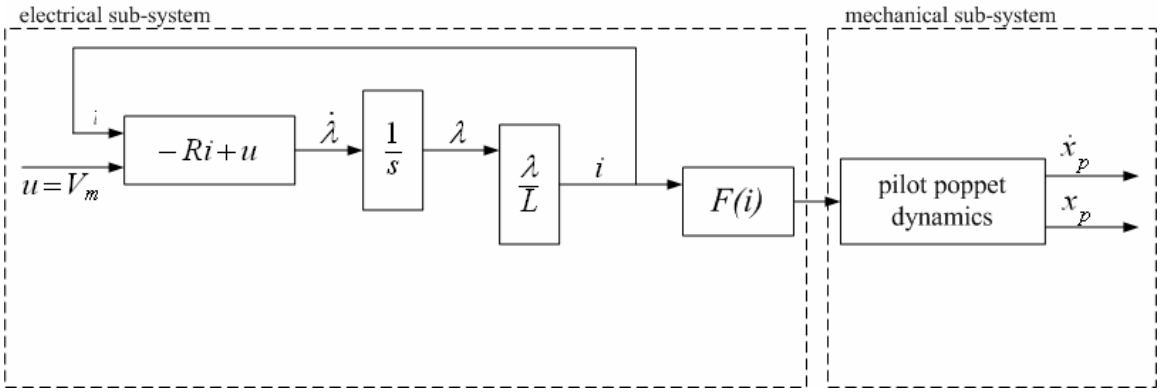

Figure 3.20: Simplified model, one-way coupling between the electrical and mechanical subsystems

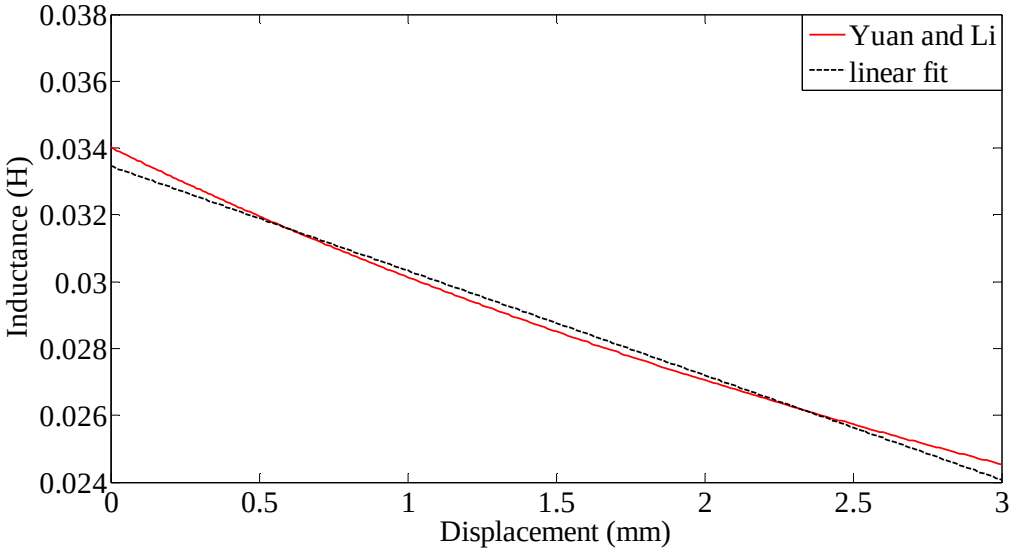

Figure 3.21: Linear fit of the inductance relationship determined by Yuan and Li [17]

CHAPTER 4

NONLINEAR CONTROL OF THE METERING POPPET VALVE

4.1 INTRODUCTION

Metering poppet valve systems can present a number of control challenges. From the literature review, poppet valve hydraulic circuits can operate in regions too far from equilibrium points for the complete behavior of the system to be captured by linearizations about equilibrium points [7]. In addition, it has been shown that the speed of flow response and steady state flow error can increase with the pressure drop across the valve [12]. These challenges indicate that any controller designed for a metering poppet valve control system would need to change with the system's dynamics in order to maintain optimal performance [12] One control concept which addresses these challenges is input-output feedback, linearization. Input-output feedback linearization linearizes the input-output map of a system using mathematical expressions of the system dynamics and feedback of the system states [25].

In the case of a metering poppet valve, if the nonlinear mechanisms which affect global behavior are well modeled, the input-output feedback linearization controller could be used to neutralize these effects in the input-output map. In this way, the input-output, feedback linearization controller is expected to handle global behavior. In addition, the input-out map would be linear and thus, well established linear techniques would be available for control design applications.

With a linear input-output map, the closed-loop system output response would behave in a linear fashion. Linear-time invariant system responses do not change with operating conditions. In this way, it is expected that the metering poppet valve system's output dynamics would be robust to the operating conditions. Speed of response and steady state flow error should remain approximately the same for different pressure drops and supply pressures.

The research presented in this chapter uses simulation methods to explore the possibility of using an input-output, feedback linearization controller to control the flow across the MU valve. Although this linearization method avoids approximations as seen in the more familiar Jacobian linearization technique, it does assume perfect knowledge of the valve's state equations. Since it is not possible to have this knowledge, such factors as parameter uncertainties and unmodeled dynamics can be detrimental to the success of the controller. Thus, the results include an analysis of the robustness of the controller due to parameter variations.

4.2 MATHEMATICAL MODEL

The model used to simulate the forced-feedback metering poppet valve is a 6^{th} order model composed of four, governing equations: two mass-spring-damper equations of motion for the main and pilot poppets, a pressure rise rate equation for the control volume, and a pressure rise rate equation for the load volume. Positive displacements for the poppets were defined as displacements into the control volume. Both poppets are prohibited from negative displacements by their poppet seats ($x_m \geq 0$, $x_p \geq 0$).

For the main poppet, Newton's second law of motion was applied with terms accounting for linear damping forces ($b_m \dot{x}_m$), the feedback spring force ($k\left(x_m + x_p + X_{sid}\right)$), pressure forces above and below the poppet ($P_c A_c$, $P_s A_s$, and $P_L A_L$) and flow forces ($0.72 C_d^2 h_3 x_m \left(P_s - P_L\right)$). The governing equation of motion for the main poppet is as follows:

$$\begin{aligned} M\ddot{x}_m = &-b_m \dot{x}_m - k\left(x_m + x_p + X_{sid}\right) - P_c A_c + P_s A_s + P_L A_L \\ &- 0.72 C_d^2 h_3 x_m \left(P_s - P_L\right) \end{aligned} . \tag{4.1}$$

where M is the mass of the main poppet (kg), x_m is the position of the main poppet (m), x_p is the position of the pilot poppet (m), b_m is the linear damping coefficient (N-s/m), k is the feedback spring constant (N/m), X_{sid} is the feedback spring preload (m), P_c is the pressure in the control volume (Pa), P_s is the supply pressure (Pa), P_L is the load pressure (Pa), A_c is the main poppet area exposed to the control volume (m), A_s is the main poppet area exposed to the supply pressure (m), A_L is the main poppet area exposed to the load pressure (m), C_d is the orifice discharge coefficient, and h_3 is the main poppet orifice slope (m).

The pilot poppet was modeled similarly with terms accounting for damping forces ($B_p \dot{x}_p$), the feedback spring force ($k\left(x_m + x_p + X_{sid}\right)$), flow forces ($0.72 C_d^2 h_2 x_p \left(P_c - P_L\right)$), and the solenoid actuator force (F). The governing equation of motion for the pilot poppet is as follows:

$$m\ddot{x}_p = -B_p \dot{x}_p - k\left(x_m + x_p + X_{sid}\right) - 0.72 C_d^2 h_2 x_p \left(P_c - P_L\right) + F . \tag{4.2}$$

where m is the mass of the pilot poppet (kg), B_p is the damping coefficient for the pilot poppet (N-s/m), and h_2 is the pilot poppet orifice slope (m).

The solenoid force was confined to a range between 0 and 60 Newtons in order to approximate the physical limitations of commercially available solenoids. In addition, the simplifying assumption was made that the pilot poppet is instantly pressure balanced. This eliminates the dynamics of a pressure volume above the pilot poppet and fluid flow between this volume and the control volume. The flow between these two volumes would traverse an orifice in the pilot poppet and act as a nonlinear damping effect on this poppet. This damping is lumped with the linear damping and represented as B_p in the model.

The dynamics of the control volume pressure were simulated by the following equations:

$$\dot{P}_c = \frac{\beta}{V_c - A_c x_m}\left(Q_1 - Q_2 + A_c \dot{x}_m\right), \tag{4.3}$$

$$\text{where } Q_1 = K_1\sqrt{P_s - P_c} \;\&\; Q_2 = K_2 x_p \sqrt{P_c - P_L}\,. \tag{4.4), (4.5}$$

and β is the fluid bulk modulus (Pa), V_c is the initial fluid volume of the control volume (m^3), K_1 is the flow gain for the control volume inlet orifice ($m^4/s\sqrt{N}$), K_2 is the flow gain for the pilot poppet orifice ($m^3/s\sqrt{N}$), Q_1 is the flow rate through the control volume inlet orifice (m^3/s), and Q_2 is the flow rate through the pilot poppet orifice (m^3/s).

The assumption has been made that the volume change of the control volume resulting from pilot poppet movement is small compared to its nominal volume and therefore the volume change here is due solely to main poppet movement. The further

simplification was made to neglect the flow contribution from the pilot poppet's movement due to its comparatively small area and displacement relative to the main poppet.

The load volume dynamics were simulated by a fixed volume connected to a tank through an orifice. The dynamics of the load volume were simulated as follows:

$$\dot{P}_L = \frac{\beta}{V_L}(Q_2 + Q_3 - Q_4), \tag{4.6}$$

$$\text{where } Q_3 = K_3 x_m \sqrt{P_s - P_L} \ \& \ Q_4 = K_4 \sqrt{P_L - P_t}\ . \tag{4.7), (4.8}$$

and V_L is the volume between the valve and load orifice (m^3), K_3 is the flow gain for the main poppet orifice ($m^3/s\sqrt{N}$), K_4 is the flow gain for the load orifice ($m^4/s\sqrt{N}$), Q_3 is the flow rate through the main poppet orifice (m^3/s), Q_4 is the flow rate through the load orifice (m^3/s), and P_t is the pressure in the tank (Pa).

All flows (Eqs. 4.4, 4.5, 4.7, and 4.8) were simulated with the classic orifice equation with the flow gains calculated as follows:

$$K_1 = a_1 C_d \sqrt{\frac{2}{\rho}},\ K_2 = h_2 C_d \sqrt{\frac{2}{\rho}}, \tag{4.9),}$$

(4.10)

$$K_3 = h_3 C_d \sqrt{\frac{2}{\rho}},\ K_4 = a_4 C_d \sqrt{\frac{2}{\rho}}\ . \tag{4.11),}$$

(4.12)

where a_1 is the area of the control volume inlet orifice (m^2), a_4 is the area of the load orifice (m^2), and ρ is the density of the fluid (kg/m^3) Although it is possible to simulate bidirectional flow through the valve, flow was restricted as shown in Figure 1.2 and

pressures were restricted as follows ($P_t \le P_L \le P_c \le P_s$). The total flow out of the valve is the sum of the flows across the pilot and main poppets (Eq. 4.13).

$$Q_{out} = Q_2 + Q_3 \tag{4.13}$$

For controller design, the model was represented in the state space form. In addition, the load dynamics were dropped and represented by a fixed load pressure parameter, P_L. The state space variables are defined as: $w_1 = x_m$, $w_2 = \dot{x}_m$, $w_3 = P_c$, $w_4 = x_p$, and $w_5 = \dot{x}_p$. The state space equations were determined as follows:

$$\boldsymbol{w} = \begin{bmatrix} w_1 & w_2 & w_3 & w_4 & w_5 \end{bmatrix}^T = \begin{bmatrix} x_m & \dot{x}_m & P_c & x_p & \dot{x}_p \end{bmatrix}^T, \tag{4.14}$$

$$\dot{\boldsymbol{w}} = \boldsymbol{f}(\boldsymbol{w}) + \boldsymbol{g}(\boldsymbol{w}) u_w, \tag{4.15}$$

$$y_w = h(\boldsymbol{w}), \tag{4.16}$$

where $\boldsymbol{w}$ is the 5 x 1 state vector. The nonlinear state function vectors were determined to be:

$$\boldsymbol{f}(\boldsymbol{w}) = \begin{bmatrix} w_2 \\ \frac{1}{M}[-b_m w_2 - k(w_1 + w_2 + preload) - w_3 A_c + P_s A_s + P_L A_L \\ -0.72 C_d^2 h_3 w_1 (P_s - P_L)] \\ \frac{\beta}{V_c - A_c w_1}\left(K_1 \sqrt{P_s - w_3} - K_2 w_4 \sqrt{w_3 - P_L} + A_c w_2\right) \\ w_5 \\ \frac{1}{m}\left[- B_p - k(w_1 + w_2 + preload) - 0.72 C_d^2 h_2 w_4 (x_3 - P_L)\right] \end{bmatrix}, \tag{4.17}$$

$$\boldsymbol{g}(\boldsymbol{w}) = \begin{bmatrix} 0 & 0 & 0 & 0 & \frac{1}{m} \end{bmatrix}^T, \tag{4.18}$$

$$u_w = F, \tag{4.19}$$

$$y_w = h(\boldsymbol{w}) = K_2 w_4 \sqrt{w_3 - P_L} + K_3 w_1 \sqrt{P_s - P_L}. \tag{4.20}$$

4.3 INPUT-OUTPUT, FEEDBACK LINEARIZATION CONTROLLER

Eqs. 4.14-4.20 represent the force-feedback metering poppet valve system used in the present study. The state-space form of the metering poppet valve system is a form which is suitable for development of an input-output, feedback linearization controller. The steps that need to be taken to complete the development of the controller are a change of variables and a state feedback control law. The development of the change of variables will be discussed next. The state feedback control law used to linearize the input-output map will be clear from the transformed system.

Define a transformation map $\boldsymbol{T}$:

$$\boldsymbol{T}(\boldsymbol{w}) = \begin{bmatrix} \boldsymbol{\varphi}(\boldsymbol{w}) \\ \boldsymbol{\psi}(\boldsymbol{w}) \end{bmatrix} = \begin{bmatrix} \boldsymbol{\eta} \\ \boldsymbol{\xi} \end{bmatrix}, \tag{4.21}$$

where $\boldsymbol{\varphi}$ and $\boldsymbol{\psi}$ are functions which transform the state vector ($\boldsymbol{w}$) into internal ($\boldsymbol{\eta}$) and external ($\boldsymbol{\xi}$) dynamic variables, respectively. The transformed system will take the form of Eqs. 4.22 – 4.25 below, also known as the normal form:

$$\dot{\boldsymbol{\eta}} = \boldsymbol{f}_0(\boldsymbol{\eta}, \boldsymbol{\xi}), \tag{4.22}$$

$$\dot{\boldsymbol{\xi}} = \mathbf{A}_c \boldsymbol{\xi} + \mathbf{B}_c \gamma(\boldsymbol{w})[u_w - \alpha(\boldsymbol{w})], \tag{4.23}$$

$$y_w = \mathbf{C}_c \boldsymbol{\xi}, \tag{4.24}$$

$$\text{where } \mathbf{A}_c = \begin{bmatrix} 0 & 1 & 0 & \dots & 0 \\ 0 & 0 & 1 & \dots & 0 \\ \vdots & & \ddots & & \vdots \\ \vdots & & & 0 & 1 \\ 0 & \dots & \dots & 0 & 0 \end{bmatrix}, \mathbf{B}_c = \begin{bmatrix} 0 \\ 0 \\ \vdots \\ 0 \\ 1 \end{bmatrix}, \mathbf{C}_c = \begin{bmatrix} 1 \\ 0 \\ \vdots \\ 0 \\ 0 \end{bmatrix}^T \tag{4.25}$$

To complete the development of the transformation ($\boldsymbol{T}$) the vector functions $\boldsymbol{\varphi}$, $\boldsymbol{\psi}$ and scalar functions α, γ need to be determined. To determine the vector and scalar functions, the input-output map must be derived. The input-output map was obtained by taking successive time derivatives of the output equation (Eq. 4.20) ($\dot{y}_w$ $\ddot{y}_w \ldots y_w^{(\theta)}$) until *u* appeared with a nonzero coefficient:

$$y_w^{(\theta)} = -\gamma(\boldsymbol{w})\alpha(\boldsymbol{w}) + \gamma(\boldsymbol{w})u_w. \tag{4.26}$$

Here, θ is referred to as the relative degree. For the metering poppet valve system defining output as in Eq. 4.20, the relative degree is 2 and thus Eq. 4.20 was differentiated to the second derivative to obtain:

$$\ddot{y}_w = -\gamma(\boldsymbol{w})\alpha(\boldsymbol{w}) + \gamma(\boldsymbol{w})u_w, \tag{4.27}$$

where,

$$\gamma(\boldsymbol{w}) = \frac{K_2\sqrt{w_3 - P_L}}{m}, \tag{4.28}$$

$$\alpha(\boldsymbol{w}) = -\frac{m}{K_2\sqrt{w_3 - P_L}}\{(\dot{w}_1)dh_{w_1} + (\dot{w}_2)dh_{w_2} + (\dot{w}_3)dh_{w_3} + (\dot{w}_4)dh_{w_4} + \frac{1}{m}(-B_p - k(w_1 + w_4 + X_{sid}) - 0.72C_d^2 h_2 w_4(w_3 - P_L))dh_{w_5}\}, \tag{4.29}$$

$$dh_{w_1} = \frac{A_c\beta K_2 w_4}{2(V_c - A_c w_1)^2\sqrt{w_3 - P_L}}(K_1\sqrt{P_s - w_3} - K_2 w_4\sqrt{w_3 - P_L} + A_C w_2), \tag{4.30}$$

$$dh_{w_2} = K_3\sqrt{P_s - P_L} + \left(\frac{A_c\beta}{V_c - A_c w_1}\right)\frac{K_2 w_4}{2\sqrt{w_3 - P_L}}, \tag{4.31}$$

$$dh_{w_3} = -\frac{\beta K_2 w_4}{4(V_c - A_c w_1)\sqrt{w_3 - P_L}}\left(\frac{K_1}{\sqrt{P_s - w_3}} + \frac{K_2 w_4}{\sqrt{w_3 - P_L}}\right), \\ -(\dot{w}_3)\frac{K_2 w_4}{4(w_3 - P_L)^{3/2}} + (\dot{w}_4)\frac{K_2}{2\sqrt{w_3 - P_L}} \tag{4.32}$$

$$dh_{w_4} = -\frac{\beta K_2^2 w_4}{2(V_c - A_c w_1)} + (\dot{w}_3)\frac{K_2}{2\sqrt{w_3 - P_L}}, \tag{4.33}$$

$$dh_{w_5} = K_2\sqrt{w_3 - P_L}\ . \tag{4.34}$$

At this point, it is important to note that examination of Eq. 4.28 indicates that $\theta = 2$ for $w_3 \neq P_L$. This defines a necessary set ($D_0 = \{\boldsymbol{w} \in \Re^5 \mid P_L < w_3 \leq P_s\}$) for the valid operation of this input-output, feedback linearization controller.

The normal form decomposed the system into an external part Eqs. 4.23 and 4.24 and an internal part Eq. 4.22. This decomposition was determined by the relative degree and thus the external state variable was a 2 x 1 transformed state vector. The transformation that maps to the external part consisted of the time derivatives of the output equation:

$$\boldsymbol{\xi} = \boldsymbol{\psi}(\boldsymbol{w}) = \begin{bmatrix}\xi_1 \\ \xi_2\end{bmatrix} = \begin{bmatrix}\psi_1(\boldsymbol{w}) \\ \psi_2(\boldsymbol{w})\end{bmatrix} = \begin{bmatrix}y_w(\boldsymbol{w}) \\ \dot{y}_w(\boldsymbol{w})\end{bmatrix}. \tag{4.35}$$

Since the system is a 5th order system, the internal state variable was a 3 x 1 transformed state vector:

$$\boldsymbol{\eta} = \boldsymbol{\varphi}(\boldsymbol{w}) = \begin{bmatrix}\eta_1 \\ \eta_2 \\ \eta_3\end{bmatrix} = \begin{bmatrix}\phi_1(\boldsymbol{w}) \\ \phi_2(\boldsymbol{w}) \\ \phi_3(\boldsymbol{w})\end{bmatrix}. \tag{4.36}$$

The transformation for the internal part should be chosen to exclude the input *u* from these dynamics and thus the criterion for choosing $\boldsymbol{\varphi}(\boldsymbol{w})$ is:

$$\frac{\partial \boldsymbol{\varphi}(\boldsymbol{w})}{\partial \boldsymbol{w}} \boldsymbol{g}(\boldsymbol{w}) = 0. \tag{4.37}$$

The internal dynamics are uncontrollable and thus the system must be minimum phase for the input-output, feedback linearization controller to be plausible. The internal dynamics are thus useful for checking whether or not the system is minimum phase. Whether or not the system is minimum phase can be determined without the internal dynamics. Thus, in the present work, a transformation for the internal part was not developed. Whether or not the system is minimum phase will be addressed below, using the zero dynamics.

In the present research, the control objective was to design a state feedback control law such that the output asymptotically tracks a reference signal $r_s(t)$. For output tracking of a reference signal, a further change of variables was defined:

$$\boldsymbol{e}_w = \boldsymbol{\xi} - \boldsymbol{R}_s \text{, where } \boldsymbol{R}_s = \begin{bmatrix} R_{s,1} \\ R_{s,2} \end{bmatrix} = \begin{bmatrix} r_s \\ \dot{r}_s \end{bmatrix}, \tag{4.38}$$

$$\Rightarrow \dot{\boldsymbol{\eta}} = \boldsymbol{f}_0(\boldsymbol{\eta}, \boldsymbol{e}_w + \boldsymbol{R}_s) \tag{4.39}$$

$$\dot{\boldsymbol{e}}_w = \mathbf{A}_c \boldsymbol{e}_w + \mathbf{B}_c \{\gamma(\boldsymbol{w})[u - \alpha(\boldsymbol{w})] - \ddot{r}_s\} \tag{4.40}$$

$$\text{where } \mathbf{A}_c = \begin{bmatrix} 0 & 1 \\ 0 & 0 \end{bmatrix}, \mathbf{B}_c = \begin{bmatrix} 0 \\ 1 \end{bmatrix} \tag{4.41}$$

The input-output map was then linearized by the following control law:

$$u_w = \alpha(\boldsymbol{w}) + \beta(\boldsymbol{w})(v + \ddot{r}_s) \tag{4.42}$$

$$\text{where } \beta(\boldsymbol{w}) = \gamma^{-1}(\boldsymbol{w}) \text{ and } v \text{ is the inner controller.} \tag{4.43}$$

producing the results:

$$\dot{\boldsymbol{\eta}} = \boldsymbol{f}_0(\boldsymbol{\eta}, \boldsymbol{e}_w + \boldsymbol{R}_s) \tag{4.44}$$

$$\dot{\boldsymbol{e}}_w = \mathbf{A}_c \boldsymbol{e}_w + \mathbf{B}_c v \tag{4.45}$$

Substitution of $\boldsymbol{e}_w$, $\dot{\boldsymbol{e}}_w$, $\mathbf{A}_c$, and $\mathbf{B}_c$ produces the controlled form of the input-output map:

$$\ddot{y}_w = v + \ddot{r}_s . \tag{4.46}$$

Controller design was completed by choosing *v* to be a Proportional Derivative (PD) controller ($v = -\mathbf{K}_{PD}\boldsymbol{e}_w$) such that $\mathbf{A}_c - \mathbf{B}_c\mathbf{K}_{PD}$ was Hurwitz and the internal state variable $\boldsymbol{\eta}(t)$ was bounded for all $t \geq 0$. Determining $\mathbf{K}_{PD}$ to satisfy the criterion was straightforward. However, to insure that $\boldsymbol{\eta}(t)$ was bounded, the system must be minimum phase. This is addressed next.

4.4 ANALYSIS OF ZERO DYNAMICS

The system is minimum phase if its zero dynamics have an asymptotically stable equilibrium point in D_0. The zero dynamics are determined by setting $\boldsymbol{\xi} = \boldsymbol{0}$ in Eq. 4.44 to obtain:

$$\dot{\boldsymbol{\eta}} = \boldsymbol{f}_0(\boldsymbol{\eta}, \boldsymbol{0}). \tag{4.47}$$

In the present research, the zero dynamics were determined using the system prior to the transformation by restricting $\boldsymbol{w}$ to the set: $Z^* = \{\boldsymbol{w} \in D_0 \mid y_w = \dot{y}_w = 0\}$ and setting $u_w = \alpha(\boldsymbol{w})|_{\boldsymbol{w}\in Z^*}$ in Eqs. 4.14 & 4.15. Using Eq. 4.20 and its first time derivative with the necessary set of validity D_0, it was determined that $Z^* = \{\boldsymbol{w} \in D_0 \mid w_1 = w_2 = w_4 = w_5 = 0\}$. In order for w_2 and w_5 to be maintained at zero, $\dot{w}_2$ and $\dot{w}_5$ must also be zero. The zero dynamics are thus:

$$kX_{sid} + w_3 A_c = P_s A_s + P_L A_L + F_{stm}, \tag{4.48}$$

where F_{stm} is the force of the main poppet seat,

$$\dot{w}_3 = \frac{\beta}{V_c}\left(K_1\sqrt{P_s - w_3}\right). \tag{4.49}$$

If the flow is restricted to zero, both poppets must be closed and not moving. If this happens at a time just after the main poppet has closed, but prior to the supply line and control volume reaching equilibrium, high pressure fluid will pour into the control volume (Q_1) until equilibrium is reached at $w_3 = P_s$. The increased pressure force from the control volume on the head of the already closed main poppet will be balanced by the force of the seat, represented in Eq. 4.48 as F_{stm}. It is thus clear that in the set D_0 the zero dynamics have an asymptotically stable equilibrium point at $w_3 = P_s$ and the system is minimum phase. To complete the discussion, $\boldsymbol{\eta}(t)$ is only bounded for sufficiently small $\mathbf{e}_w(0)$, $\boldsymbol{\eta}(0)$, and $\mathbf{R}_s(t)$. The set in which $\mathbf{e}_w(0)$, $\boldsymbol{\eta}(0)$, and $\mathbf{R}_s(t)$ are sufficiently small must be a subset of D_0 and the necessary and sufficient set of operation for this input-output, feedback linearization controller. In the present research $\mathbf{w}(0) = \mathbf{0}$ and $\mathbf{R}_s(0) = \mathbf{0}$ thus, $\mathbf{e}_w(0) = \mathbf{0}$ and $\boldsymbol{\eta}(0) = \mathbf{0}$. $r_s(t)$ was restricted to the range between 0 and 90 L/min and was sufficiently small.

4.5 RESULTS AND DISCUSSION

The control strategy developed above has been tested in a series of simulations. The attention focused on the response of controller tracking under different operating conditions, parameter perturbations, and disturbances. In the results that follow, the

reference trajectory was the step response of a linear second order system with a damping ratio of 0.5 and natural frequency of 50 Hz. The step occurred at 0.2 s. Nominal operating conditions were chosen to be: supply pressure (P_s) = 21 MPa and pressure drop across the valve (ΔP) = 2.1 MPa. These conditions were chosen as nominal due to the fact that valve geometry produces a flow of 120 LPM with the main poppet fully open at a pressure drop of 2.1 MPa. To serve as a benchmark, a PID controller was tuned.

For nominal conditions, the responses of both controllers are plotted in Fig. 4.1. The input-output controller performed well, with close tracking to the reference trajectory. This result indicates that for these conditions, the system nonlinearities were canceled by the controller causing the closed loop system to behave like the second order linear system it was tracking. Shortly after the step applied to the reference system at 0.2 s, a small deviation of the flow from the reference trajectory occurred. The deviation of the flow from the reference trajectory is pictured more closely in Fig. 4.2. This flow deviation occurred when the main poppet opened. An analytical explanation follows.

As discussed above, the solenoid force was confined to a range between 0 N and 60 N. This range served to limit the controller's output and thus the expression for the controller in Eqs. 4.42 and 4.43 is incomplete. To complete this expression, Eq. 4.42 is redefined:

$$u_{w,T} = \alpha(\boldsymbol{w}) + \beta(\boldsymbol{w})(v + \ddot{r}_s). \tag{4.50}$$

The effective controller output is then defined as follows:

$$u_w = u_{w,T} + F_s \tag{4.51}$$

$$\text{where } F_s = \begin{Bmatrix} 0, & if \quad 0 \le u_{w,T} \le 60 \\ -u_{w,T} + 60, & if \quad u_{w,T} > 60 \\ -u_{w,T}, & if \quad u_{w,T} < 0 \end{Bmatrix} \tag{4.52}$$

With this completed controller expression, Eq. 4.46 must be corrected:

$$\ddot{y}_w = v + \ddot{r}_s + \gamma(\boldsymbol{w})F_s = \begin{Bmatrix} v + \ddot{r}_s, & if \quad 0 \le u_{w,T} \le 60 \\ -\gamma(\boldsymbol{w})\alpha(\boldsymbol{w}) + \gamma(\boldsymbol{w})60, & if \quad u_{w,T} > 60 \\ -\gamma(\boldsymbol{w})\alpha(\boldsymbol{w}), & if \quad u_{w,T} < 0 \end{Bmatrix}. \tag{4.53}$$

Eq. 4.53 is the final equation needed for an analytical understanding of the flow deviation that occurred when the main poppet opened. Eqs. 4.29 and 4.31 for $\alpha(\boldsymbol{w})$ indicate that when the main poppet opens, its acceleration ($\dot{w}_2$) causes a dramatic decrease in $\alpha(\boldsymbol{w})$ and thus u_w driving both variables to negative values. The controller action is reasonable in light of the dramatic flow increase that accompanies the opening of the main poppet. The controller is seeking to attenuate the flow increase and maintain reference signal tracking. However, the effective input signal saturates at zero. Eq. 4.53 indicates that $\ddot{y}_w = -\gamma(\boldsymbol{w})\alpha(\boldsymbol{w})$ when $u_w = 0$. With $\alpha(\boldsymbol{w})$ becoming increasingly more negative, $\ddot{y}_w$ becomes increasingly more positive and thus y increases when the effective input saturates at zero due to $\alpha(\boldsymbol{w})$. As the main poppet slows, its decreased acceleration allows the effective input u_w to rise above zero and resume reference tracking. As the results show, this effect was present in all simulations to varying degrees.

It is believed that an inherent system time delay is the underlying mechanism responsible for the flow deviation. The time delay occurs between the actuation of the pilot stage and the response of the main stage, immediately following the opening of the main poppet. When the main poppet opened, its acceleration caused the controller to allow the pilot poppet to be closed by the feedback spring. With the closing of the pilot poppet, the pressure in the control volume increased and this pressure slowed and reversed the acceleration of the main poppet. In terms of flow, when the main poppet opened there was an accompanying dramatic increase in flow. The controller responded to the dramatic flow increase by indirectly increasing the pressure in the control volume to slow the main poppet opening and thus the flow increase. However, there was a time delay between controller action at the pilot stage and flow control at the main stage.

Displayed in Fig. 4.3 are the results of controller tracking at four different conditions: (1) P_s = 21 MPa, ΔP = 2.1 MPa; (2) P_s = 28.9 MPa, ΔP = 10 MPa; (3) P_s = 30 MPa, ΔP = 20 MPa; (4) P_s = 35 MPa, ΔP = 35 MPa. In all conditions, tracking was close until the main poppet opened and the controller saturated at its lower limit. Upon controller saturation, the flow spiked with the magnitude of the spike dependent on the ΔP. Following the flow deviation, the controller reestablished tracking of the dynamic time behavior of the reference signal. The flows at all four conditions exhibited the same rise time and settling time as the reference signal.

Despite the dynamic time behavior being reestablished, full recovery was not achieved due to tracking error in all conditions. The magnitude of the tracking error was also dependent on the ΔP as was the magnitude of the flow deviation. This suggests that the tracking error was dependent on controller saturation as was the flow deviation.

However, this is unclear. In conditions 2, 3 and 4, where tracking error is increasingly noticeable, the valve flow oscillates with high frequency and low amplitude. Examination of the controller in these conditions revealed that the controller continuously saturated at its lower limit.

To test the response of the system when stepped from different operating points, a profile with multiple changes in the step level was applied to the system. The results of this simulation are displayed in Figure 4.4. Since the input-output map was linearized, it was expected that the system should have the same step response despite its operating point. Qualitatively, this is confirmed everywhere except at the first step. Again, the large overshoot is a result of the opening of the main poppet and the time delay between controller actuation and main valve response.

The analytical analysis above indicates that the controller is saturated at its lower bound during the first step up. The analytical analysis also indicates that when controller saturation occurs at its lower bound, the input-output map is no longer linear. From Eq. 4.53, it reverts to its pre-linearization form. To test the linearization in the present numerical analysis, it was important to insure that lower-bound saturation was avoided during the steps. Unfortunately, this was not possible and decreasing degrees of saturation occurred as the operating point increased. This explains slight differences in the steps, particularly between the step-ups and the step-downs. Quantitatively, the step-ups averaged a rise time of ~4.4 ms while the step-downs averaged a fall time of ~6.6 ms. During the step-ups, the controller saturated at its lower bound and during the step-downs, the controller saturated at its upper bound.

To further test the linearization, the step responses from the model with the input-output feedback linearization controller (closed-loop system) were compared to the step responses from the model without the controller (open-loop system). Step responses were compared at each of the four conditions defined above. Due to the linearization, it is expected that the closed-loop system be more robust to the changing pressure conditions than the open-loop system. This means that the closed-loop system should reach approximately the same steady-state flow value under all four conditions, where as the open-loop system will likely not achieve approximately the same steady-state flow value under all four conditions.

To make an accurate comparison between the open-loop and closed-loop systems a step input at condition 1 was applied to the open-loop system and the simulation run until the open-loop system reached steady-state. The steady-state flow value was noted and used in the closed-loop case. In the closed-loop case, a step reference input, having a final value equal to the steady-state flow observed in the open loop case, was applied to the controller. The objective was to guarantee that the flow in the open-loop and closed-loop systems, had the same initial and final values.

Figures 4.5 – 4.8 show that both the open-loop and closed-loop systems exhibit a steady-state flow that was dependent on the pressure conditions. In the closed-loop system, the pressure dependence of the flow is attenuated by the controller as the flow in the closed-loop relative to the open-loop case more closely tracks the steady-state value of approximately 10.5 L/min. In the open-loop case, the speed of response of the flow increases with increasing pressure drop across the valve. In addition to the increase in response speed, the open loop valve exhibits slight overshoots and damped oscillations at

conditions 2, 3, and 4. With the closed-loop system, the input-output feedback linearization controller produces and even greater rise time than the open-loop system under all four conditions. In addition, it appears that the closed-loop system's rise times are approximately the same under all four conditions. However, in the closed-loop cases, the controller caused the actual flow to overshoot the reference value. The magnitude of this overshoot increased with increasing pressure drop across the valve. The closed-loop results of flow overshoot are consistent with what has been observed during the opening of the main poppet in previous simulations.

To test the response of the controller to disturbances, two simulations were run during which the supply pressure was increased at 1 s to 23 MPa and 28.9 MPa from the nominal condition. The results of the simulations are shown in Fig. 4.5. The response to the disturbance in each simulation was a transient spike which lasted no longer than 50 ms. For the increase to 28.9 MPa, the spike was twice as large with a slightly longer duration. In both simulations controller saturation accounted for the magnitude of the height of the spikes. Close steady state tracking was restored in both cases. It should be noted that the pressure disturbance occurred after reaching steady state conditions. This, along with the nominal operating conditions, likely explains the ability of the controller to reestablish reference tracking. This is in contrast to cases following initial pressure deviations of lower magnitude at more extreme operating conditions, Fig. 4.9.

To test the robustness of the model, certain parameters in the model were separately increased by as much as 50 % and decreased by as much as 40 %. Simulations were then run in the nominal conditions. The parameters chosen were those which might have the most variation in time and from valve to valve based on real world

considerations: the area of the inlet orifice to the control volume (a_1), the slope for the pilot poppet orifice (h_2), and the slope for the main poppet orifice (h_3). The results of these simulations are displayed in Figs. 4.10 & 4.11. Not displayed are robustness results to variations in h_3 because the controller proved to be very robust to changes in this parameter. The results can be explained as follows: for those parameters which are changed in the model, the terms which they are associated with in the input-output map will not be eliminated. Instead, there will be residual nonlinear terms multiplied by the parameter perturbations remaining in the input-output map. These residuals affect the response of the closed loop system and, if large enough, will destabilize it.

In examining the transition to main orifice flow and the control error the transition caused, another approach to flow control was discovered. If the position of the main poppet were to be controlled using feedback linearization then flow control can be conducted as follows. First, assume a desired flow value, Q_d. Further, realize that the feedback linearization can be applied to the output equation, $y_w = x_m$, using the same approach discussed above. A linearized input-output map of the form of Eq. 4.46 ($y_w^{(\theta)} = v + r_s^{(\theta)}$) would result. Then, the flow equation (Eq. 4.13) can be solved using Q_d to obtain a reference value (r_s) for the linearized input-output map, Eq. 4.54.

$$r = \frac{Q_d - K_2 w_4 \sqrt{w_3 - P_L}}{K_3 \sqrt{P_s - P_L}} \tag{4.54}$$

It is expected that the delay which affects the flow control will not be as pronounced in position control. In addition, preliminary calculations show that the system is full-state feedback linearizable when the main poppet position is defined as the output. This means

that the complete system will be feedback linearized and all states controllable. This is left as future work.

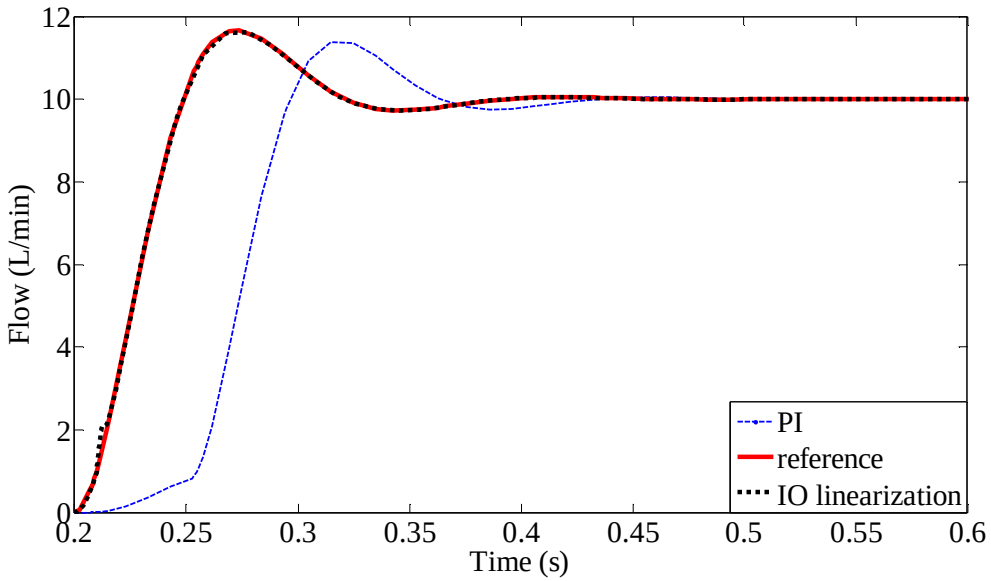

Figure 4.1: Controller comparison at a supply pressure of 21 MPa and a pressure drop of 2.1 MPa

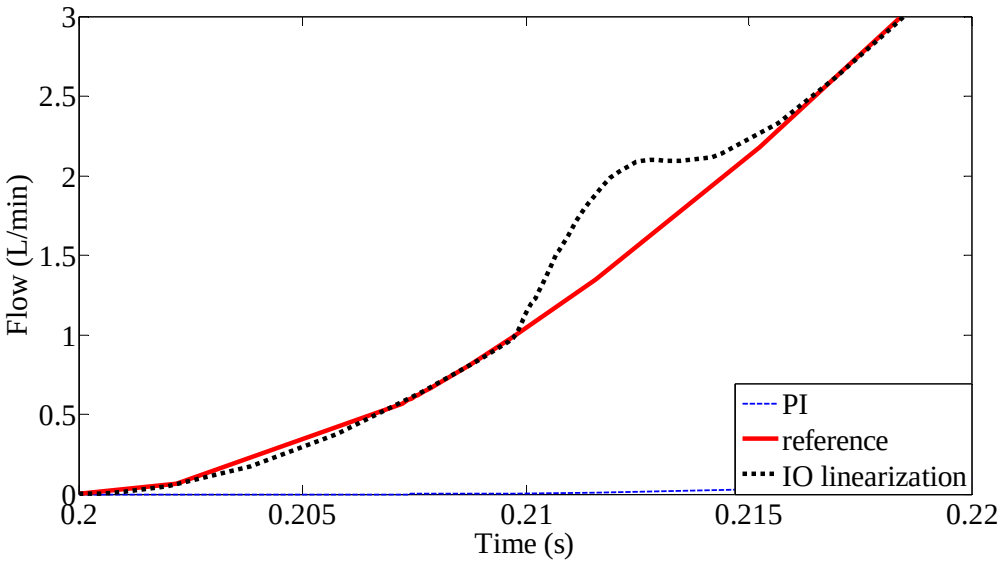

Figure 4.2: Controller comparison at a supply pressure of 21 MPa and a pressure drop of 2.1 MPa, effect of controller saturation

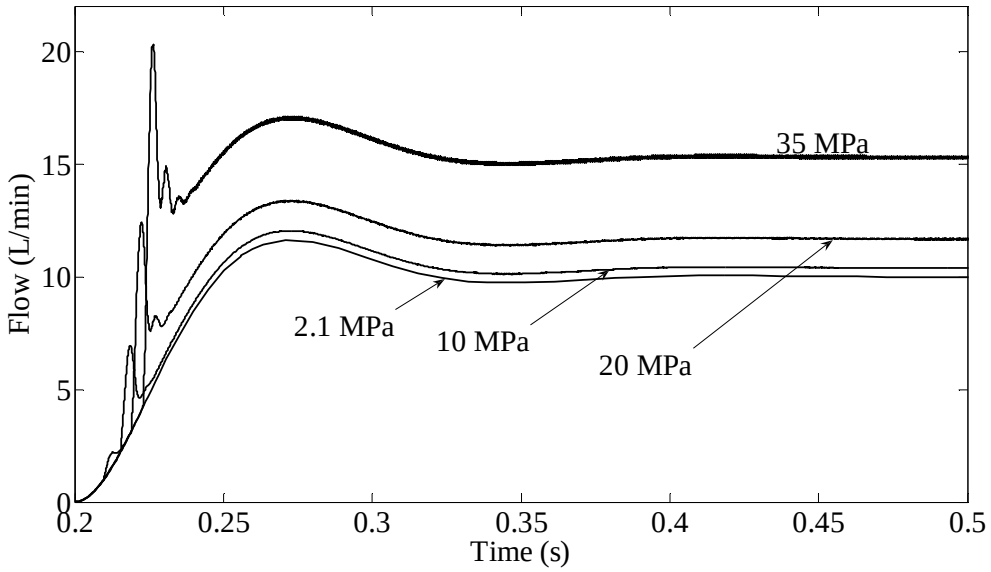

Figure 4.3: Response in different operating conditions

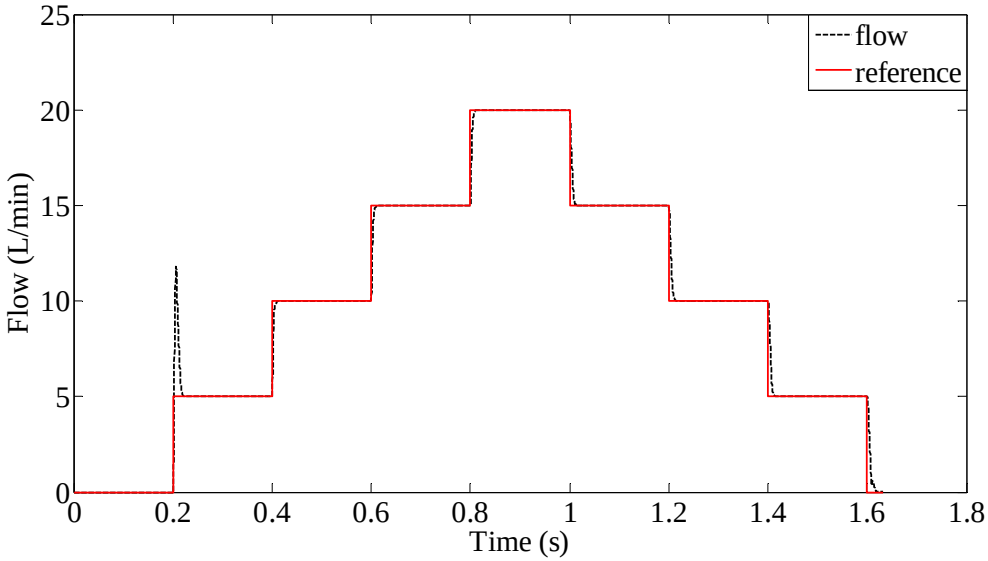

Figure 4.4: Closed-loop system response at different operating points

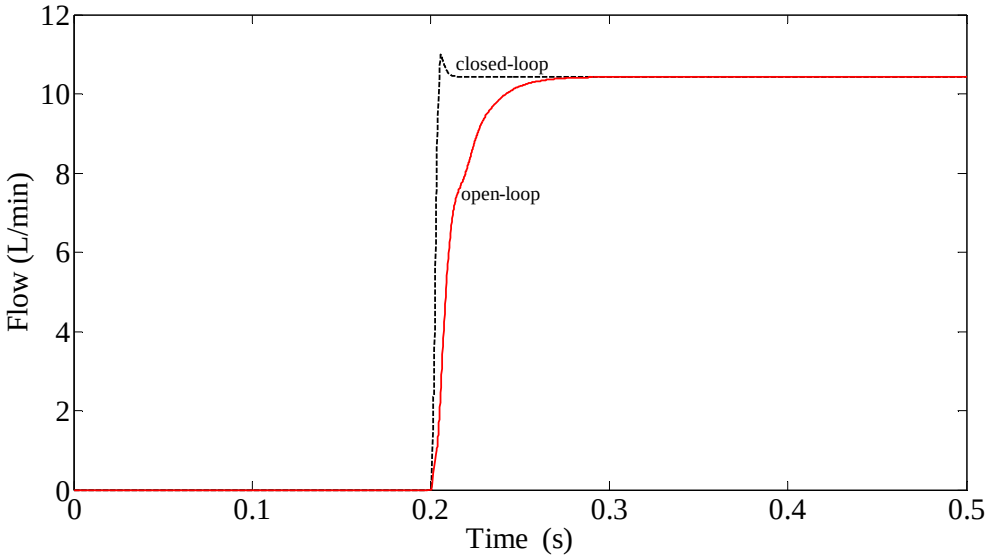

Figure 4.5: Open-loop and closed-loop step response in condition 1

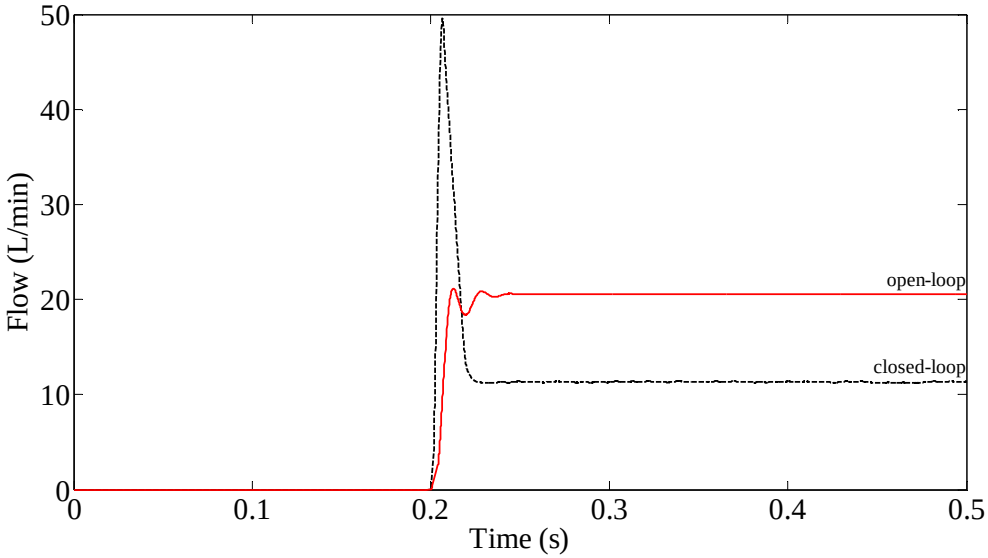

Figure 4.6: Open-loop and closed-loop step response in condition 2

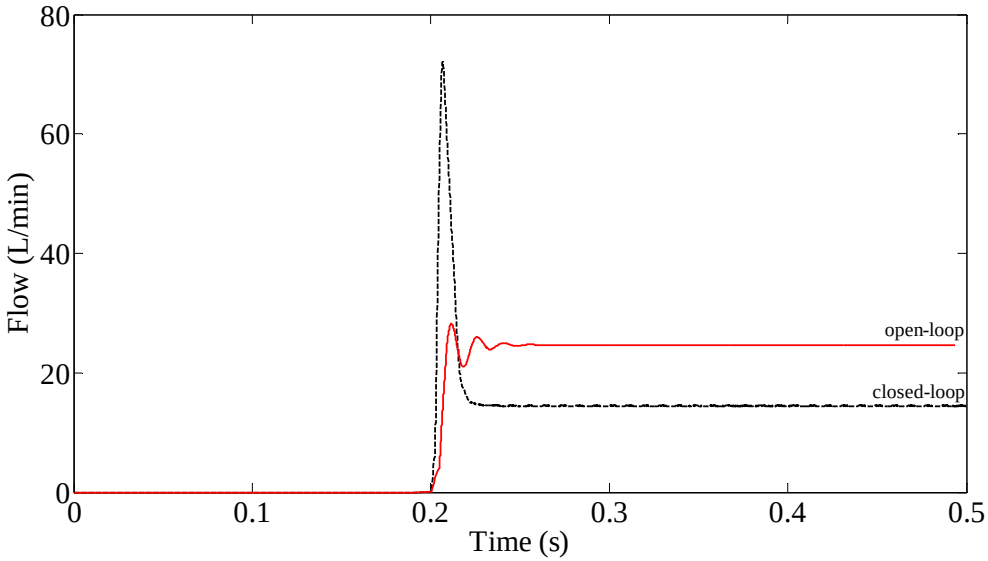

Figure 4.7: Open-loop and closed-loop step response in condition 3

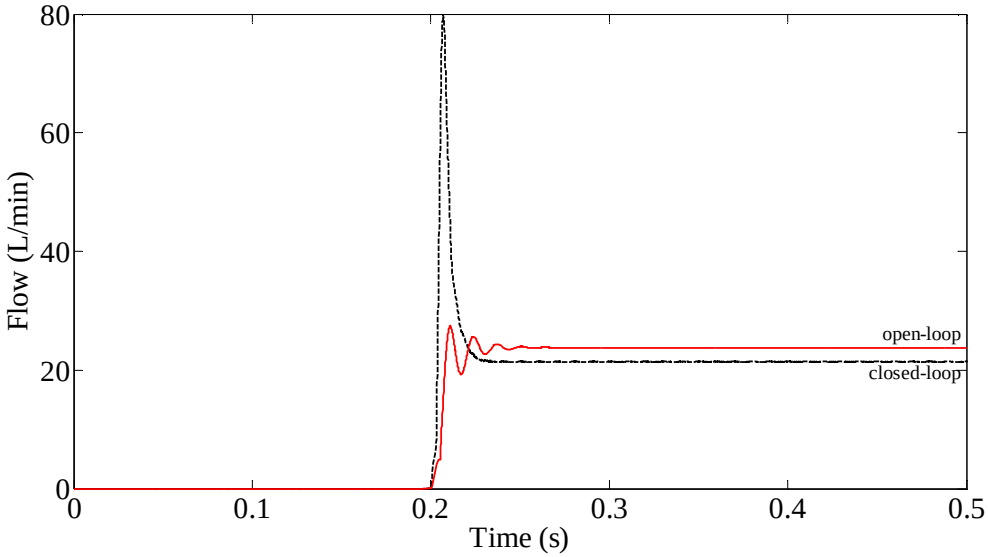

Figure 4.8: Open-loop and closed-loop step response in condition 4

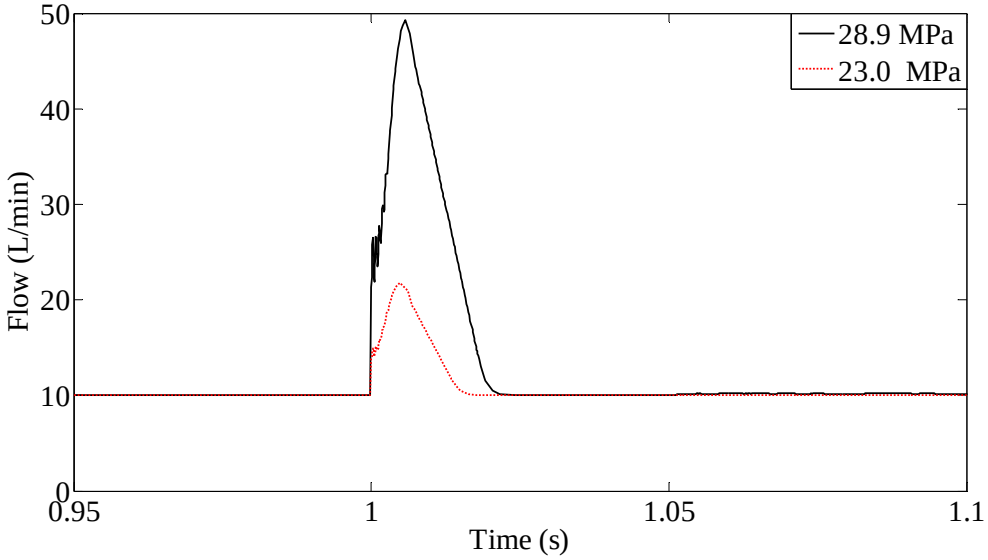

Figure 4.9: Closed-loop **r**esponse to supply pressure disturbances

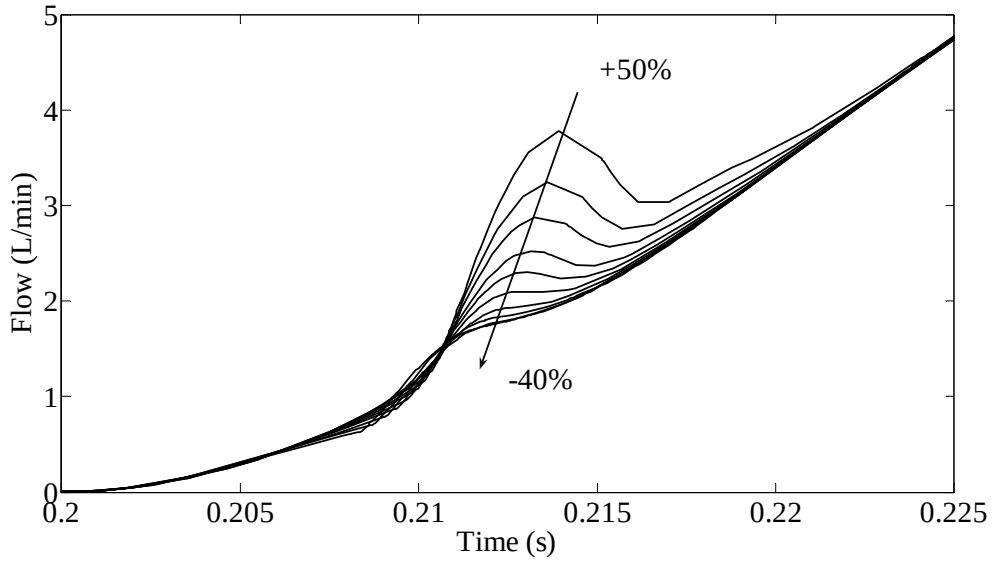

Figure 4.10: Robustness to changes in the area of the inlet orifice to the control volume

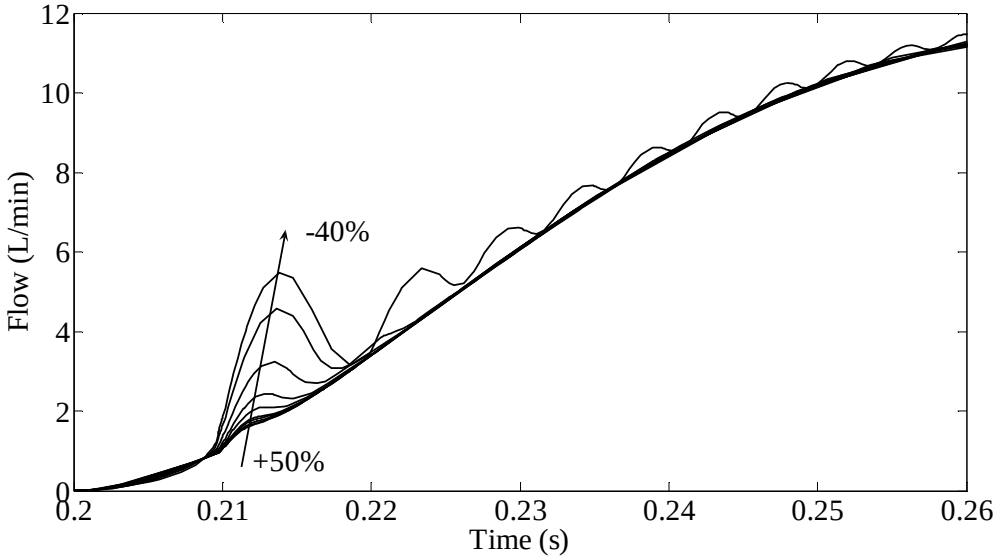

Figure 4.11: Robustness to changes in the slope for the pilot poppet orifice

CHAPTER 5

CONCLUSIONS

5.1 INTRODUCTION

A metering poppet valve has been developed at the University of Missouri-Columbia to perform flow control in place of more commonly used spool valves. Metering poppet valves offer certain advantages over spool valves which makes them more attractive in the flow metering role over spool valves. Performance and stability issues need to be addressed before metering poppet valves are fully accepted in the flow control role.

In the present research, active damping and input-output, feedback linearization control were both studied to test the ability of these approaches to maintain the MU valve's stability and good performance at the same time. Here, stability in the classical sense, poles located in the left-half plane, is guaranteed. The stability issues observed from the MU valve and other metering poppet valves are undesirable oscillations in the valve's position response which can adversely affect "down stream" components. The time domain specifications of overshoot, settling time, and peak-to-peak amplitude were used to analyze the results of the present work. The performance of the metering poppet valve is important for flow control and disturbance rejection. Here, performance was synonymous with the speed of response. The time domain specification of rise time was used as an indicator.

5.2 ACTIVE DAMPING

In this work, active damping took the form of solenoid damping of the pilot poppet using velocity feedback. Velocity is desirable in the active damping role because it carries the dynamic information of the pilot poppet. The velocity of the pilot poppet is not easily obtained and in this research, it was proposed that the self-sensing actuator concept be used. In the present research velocity control was desired over position control because it was expected that velocity could be better estimated than position. The Kalman filter results allowed a conclusion to be drawn regarding this expectation.

The Kalman filter results showed that both position and velocity were poorly estimated at sufficiently large steps away from the operating point. The position estimation errors took the form of transient and steady errors. For the Kalman filter's velocity estimate, only transient error was present. With the velocity estimate in a proportional active damping scheme, a level of damping would be provided by the transient portion of the estimate. For active damping with position control, the transient portion of the position estimate would also provide a level of damping. However, the steady-state estimation error of the position estimate would result in steady-state position error.

In addition, direct position control of the pilot poppet in a forced-feedback metering poppet valve is not desirable. With the forced-feedback metering poppet valve, the function of the feedback spring is to adjust the pilot poppet position in response to the main poppet opening for the purpose of balancing the force applied to the pilot poppet by the solenoid. A position controller would negate this function.

With the extended Kalman filter, it was shown that the self-sensing actuator concept is a viable approach to determining the position and velocity of a poppet if certain conditions are met. First, the poppet must be directly controlled by an EMA. Second, the position and velocity must be observable from the EMA current measurement. For a solenoid EMA, this means that the inductance must have a measurable position dependence.

In the MU valve, damping of the pilot poppet is also achieved via flow of hydraulic fluid through a tube in the pilot poppet. In the present research this was referred to as passive damping. With passive damping in the MU valve, results showed that the radius of the tube in the pilot poppet affects the trade-off between performance and stability. With a larger radius tube, there was a shorter rise time and longer settling time relative to the case with a smaller radius tube.

It was the original goal to explore active damping because it was expected that active damping would allow a coordinated dissipation of energy while preserving the performance of the system. The results from the present research do not fully support that expectation. Active damping attenuated the peak-to-peak amplitude and decreased the settling time of the position response. However, the rise time of the position response was increased.

Despite the results of the present study, the active damping scheme is still very promising. Here, only a simplified proportional damping scheme was tested. It is expected that more sophisticated, frequency based, damping schemes will help to realize the original goal of a valve designed for performance while incorporating active damping for coordinated energy dissipation.

Results have shown that active damping might also be desirable for energy conservation. It was shown that the proportional damping scheme exhibits efficient characteristics by consuming only the energy that is needed to achieve a certain response. In addition to this advantage, the active damping approach avoids one important draw-back to the passive damping approach. With passive damping, the flow of hydraulic fluid through the pilot poppet tube is dependent on the viscosity of the fluid. Fluid viscosity is dependent on such factors as fluid composition and temperature. Thus, tube damping is dependent on such factors as fluid composition and temperature. These factors can change with fluid contamination and operating environment. Active damping avoids the uncertainty of fluid viscosity and is thus a robust damping approach with respect fluid viscosity.

Finally, with the active damping approach, more work is needed. A lot of study and optimization is possible. Here, the first steps have been taken towards providing a technique which will allow a metering poppet valve to be designed for performance while active damping is used for energy dissipation. These first steps include: 1. the first use of active damping with the estimated velocity state through the use of current and voltage measurement in a valve, 2. the first use of active damping with a forced-feedback metering poppet valve, and 3. a unique and promising approach to producing a metering poppet valve capable of attaining both performance and stability.

In the right conditions, this approach will be very useful. Success could be achieved by developing the system from the ground up with this approach in mind rather than retrofitting this approach to an existing system. Developing from the ground up would include designing a solenoid EMA which provides a controllable electromagnetic

force and has an armature with position dependent inductance which allows for accurate observation of the position and velocity of the armature.

5.3 FEEDBACK LINEARIZATION CONTROL

With the MU valve and input-output feedback linearization there is the potential for the neutralization of problematic nonlinearities. This would allow the input-output map to behave in a linear fashion and produce a system with good flow control and flow disturbance rejection. To assess this potential, reference tracking was attempted with four different pressure conditions.

Although the results are promising, the controller exhibited some troubling characteristics. First, the closed-loop system responded to the opening of the main poppet with flow deviations. This behavior was unique to the input-output, feedback linearization closed-loop system since the open-loop system did not exhibit such deviations when the main poppet opened. Analytically, it was shown that the acceleration of the main poppet causes the controller to quickly saturate. When the controller saturates, the input-output map is no longer linear and reference tracking is temporarily lost. Physically it was proposed that an inherent system delay between control action at the pilot poppet and pressure increase in the control volume was the underlying mechanism behind the flow deviations.

Second, at higher pressure drops across the valve, transient and steady-state tracking error occurred. The magnitude of the tracking error was shown to be dependent on the magnitude of the pressure drop. This result was unexpected since the input-output

map was linear. It was expected that the valve would exhibit the same response in any pressure condition. Controller saturation is theorized to also be responsible for the unexpected tracking results. In all of the cases where tracking error occurred, controller saturation also occurred. It was shown that when controller saturation occurred, the input-output map ceased to be linear. This explains the nonlinear response of the closed-loop system to different operating conditions. In addition, it was shown that when controller saturation was largely avoided, the input-output map behaved in a mostly linear fashion despite its current operating point.

Despite these issues, the controller was shown to perform reference tracking while remaining stable. The controller moderately recovered from the flow deviations, never allowing the deviations to exponentially increase unchecked. In addition, in comparison to the open-loop system, the closed-loop system performed better flow tracking. Disturbance rejection was achieved in limited simulations and robustness was demonstrated through numerical simulations. In the future, the input-output map from force (F) to main poppet position (x_m) should be used to apply feedback linearization to the complete system. In this way all states will be controllable. Also, alternative feedback linearization approaches which neutralize specific nonlinearities should be investigated. System nonlinearities which have a positive effect on valve performance and stability should not be neutralized. The feedback linearization results presented in the present work represent the first attempt to neutralize nonlinearities using feedback linearization in a metering poppet valve.

APPENDIX A – NOMENCLATURE

$\mathbf{A}$ Linearized, simplified model, state matrix (4x4)

$\hat{\mathbf{A}}$ Linear estimator, state matrix (4x4)

$\mathbf{A}_c$ Feedback linearized model, system matrix (2x2)

$\mathbf{A}_\rho$ Linearized, reduced-order, simplified model, system matrix (3x3)

A For the simplified model, $A = A_c = A_p$ (5e-5 m^2)

A_c Main poppet area exposed to the control volume (5e-5 m^2)

A_{in} Amplitude of the sine wave input to the solenoid testbed (V)

A_L Main poppet area exposed to the load pressure (1.9e-4 m^2)

A_{out} Amplitude of the sine wave output from the solenoid testbed (A)

A_p Pilot poppet area exposed to the pilot volume (5e-5 m^2)

A_s Main poppet area exposed to the supply pressure (1.9e-4 m^2)

a_1 Control volume, inlet orifice, area (4.375e-7 m^2)

a_4 Load orifice area (5e-6 m^2)

$\mathbf{B}$ Linearized simplified model, input matrix (4x1)

$\hat{\mathbf{B}}$ Linear estimator, input matrix (4x1)

$\mathbf{B}_c$ Feedback linearized model, input matrix (2x1)

$\mathbf{B}_k$ Linearized, discretized, simplified model input matrix (4x1)

B_p Pilot poppet damping coefficient (15.75 N-s/m)

b_m Main poppet linear damping coefficient (1.8 N-s/m)

$\mathbf{C}$ Linearized simplified model, output matrix (1x4)

$\mathbf{C}_c$ Feedback Linearized model, output matrix (1x2)

$\mathbf{C}_k$ Linearized, discretized, simplified model output matrix (1x4)

$\mathbf{C}_\rho$ Linearized, reduced-order, simplified model, output matrix (1x3)

C_d Orifice discharge coefficient (0.62)

d Solenoid parameter (7.76e-3 m) (see Appendix B.4)

F Solenoid EMA force on the pilot poppet (N)

F_s Solenoid EMA saturation term

F_{stm} Force from the main poppet seat (N)

G Linear, active damping gain (V-s/m)

h_2 Pilot poppet orifice slope (8.16e-4 m)

h_3 Main poppet orifice slope (6.38e-3 m)

i Current in the coil of the solenoid EMA (A.)

i_e Current in the coil of the solenoid EMA used in solenoid testbed (A)

$\mathbf{K}_k$ Kalman gain matrix (4x1)

$\mathbf{K}_{le}$ Linear estimator gain matrix (4x1)

$\mathbf{K}_{PD}$ Proportional derivative controller gain matrix (1x2)

K_1 Control volume inlet orifice flow gain (1.33e-8 $\mathrm{m}^4/\mathrm{s}\sqrt{\mathrm{N}}$)

K_2 Pilot poppet orifice flow gain (2.45e-5 $\mathrm{m}^3/\mathrm{s}\sqrt{\mathrm{N}}$)

K_3 Main poppet orifice flow gain (1.94e-4 $\mathrm{m}^3/\mathrm{s}\sqrt{\mathrm{N}}$)

K_4 Load orifice flow gain (1.52e-7 $\mathrm{m}^4/\mathrm{s}\sqrt{\mathrm{N}}$)

k Feedback spring constant (7000 N/m^2)

$L(\cdot)$ Solenoid EMA inductance (H)

L_e Inductance of the solenoid EMA used in the solenoid testbed (H)

L_l Inductance determined by a linear fit to the relationship from the literature (H)

L_p Pilot poppet tube length (0.02 m)

M Main poppet mass (0.166 kg)

m Pilot poppet mass (0.0415 kg)

N Observability test matrix for the linearized, reduced order simplified model (3x3)

$\mathbf{P}_k$ Kalman filter error covariance matrix (4x4)

P_c Control volume pressure (Pa)

P_L Load volume pressure (Pa)

P_p Pilot volume pressure (Pa)

P_s Supply pressure (Pa)

P_t Tank pressure (Pa)

ΔP Net pressure acting on the pilot poppet in the simplified model (Pa)

Q Pilot poppet tube flow rate (m^3/s)

Q_{out} Valve total out flow rate (L/min)

Q_1 Control volume, inlet orifice, flow rate (m^3/s)

Q_2 Pilot poppet orifice flow rate (m^3/s)

Q_3 Main poppet orifice flow rate (m^3/s)

Q_4 Load orifice flow rate (m^3/s)

$\mathbf{R}_k$ Process noise covariance matrix (4x4) (diag([0.75e3 m^2 1e2 m^2/s^2 2e5 Wb^2])),

note: for the simulation results the 3rd-order ROSM was used

$\mathbf{R}_s$ Reference trajectory vector

$\boldsymbol{r}_k$ Process noise vector (4x1)

R Pilot poppet, tube radius (9e-4 m)

$R_{e,2}$ Resistance of the coil of the solenoid EMA used in the solenoid testbed (5.1 Ω)

R_2 Resistance of the coils of the solenoid EMA (0.5 Ω)

r_s Reference trajectory (L/min)

T_s Numerical integration time step (0.0001 s)

V Voltage applied across the solenoid EMA coil (Volts)

V_c Control volume fluid volume (8.36e-6 m^3)

V_e Voltage applied across the solenoid EMA coil used in the solenoid testbed (Volts)

V_k Measurement noise variance (2.89e-16 A^2)

V_L Volume between valve and load orifice (0.002 m^3)

V_o Initial volume below the pilot poppet in the simplified model (8.36e-6 m^3)

v Inner controller

v_k Measurement noise scalar (1.7e-8 A)

x_c Pilot poppet initial position in the simplified model (0.01 m)

x_m Main poppet position (0 – 0.007 m)

x_p Pilot poppet position (0 – 0.003 m)

X_{sid} Feedback spring preload (5e-6 m)

β_2 Solenoid parameter (0.264e-4 H-m) (see Appendix B.4)

β Hydraulic fluid bulk modulus (1.334e9 Pa)

δ In front of a variable, denotes a perturbation

θ Relative degree

λ Flux linkage (Wb)

λ_e Flux linkage of the solenoid EMA used in the solenoid testbed (Wb)

μ Hydraulic fluid viscosity (0.01 N-s/m^2)

ρ Hydraulic fluid density (833 kg/m^3)

$\mathbf{\Phi}_k$ Linearized, discretized, simplified model state transition matrix (4x4)

τ_e Time constant of the solenoid EMA used in the solenoid testbed (s)

$\wedge$ Above a variable, denotes an estimate

$*$ Superscript to a variable, denotes an operating point

$^-$ Superscript to a variable, denotes an *a priori* estimate

$_k$ Subscript to a variable, denotes a discrete variable

APPENDIX B – RELATED DERIVATIONS

B.1 JACOBIAN LINEARIZATION FORMS

To derive the linearized state equations for:

$$\dot{\boldsymbol{z}} = \boldsymbol{f}_o(\boldsymbol{z}, u) \tag{B.1}$$

$$y = h_o(\boldsymbol{z}) \tag{B.2}$$

define perturbations:

$$\boldsymbol{\delta z} = \boldsymbol{z} - \boldsymbol{z}^* \tag{B.3}$$

$$\Rightarrow \boldsymbol{\delta}\dot{\boldsymbol{z}} = \dot{\boldsymbol{z}} - \dot{\boldsymbol{z}}^* \tag{B.4}$$

$$\delta u = u - u^* \tag{B.5}$$

$$\delta y = y - y^* \tag{B.6}$$

where $\boldsymbol{z}^*, u^*$, and y^* are time varying or constant reference trajectories.

Calculate the Taylor Series expansion of $\boldsymbol{f}_o(\boldsymbol{z}, u)$ about $\boldsymbol{z}^*$ and u^*, neglecting higher order terms:

$$\boldsymbol{f}_o(\boldsymbol{z}, u) \cong \boldsymbol{f}_o(\boldsymbol{z}^*, u^*) + \left(\frac{\partial \boldsymbol{f}_o}{\partial \boldsymbol{z}}\right)_{\boldsymbol{z}=\boldsymbol{z}^*} \boldsymbol{\delta z} + \left(\frac{\partial \boldsymbol{f}_o}{\partial u}\right)_{u=u^*} \delta u \tag{B.7}$$

From Eq. B.1:

$$\dot{\boldsymbol{z}}^* = \boldsymbol{f}_o(\boldsymbol{z}^*, u^*) \tag{B.8}$$

Substitute Eqs. B.1 and B.8 into Eq. B.7:

$$\dot{\boldsymbol{z}} \cong \dot{\boldsymbol{z}}^* + \left(\frac{\partial \boldsymbol{f}_o}{\partial \boldsymbol{z}}\right)_{\boldsymbol{z}=\boldsymbol{z}^*} \boldsymbol{\delta z} + \left(\frac{\partial \boldsymbol{f}_o}{\partial u}\right)_{u=u^*} \delta u \tag{B.9}$$

In Eq B.9, subtract $\dot{\boldsymbol{z}}^*$ from the left and right sides and substitute Eq. B.4 into the left side:

$$\boldsymbol{\delta}\dot{\boldsymbol{z}} \cong \left(\frac{\partial \boldsymbol{f}_o}{\partial \boldsymbol{z}}\right)_{\boldsymbol{z}=\boldsymbol{z}^*} \boldsymbol{\delta z} + \left(\frac{\partial \boldsymbol{f}_o}{\partial u}\right)_{u=u^*} \delta u \tag{B.10}$$

Defining:

$$\mathbf{A} = \left(\frac{\partial \boldsymbol{f}_o}{\partial \boldsymbol{z}}\right)_{\boldsymbol{z}=\boldsymbol{z}^*} \text{ and } \mathbf{B} = \left(\frac{\partial \boldsymbol{f}_o}{\partial u}\right)_{u=u^*} \tag{B.11}$$

produces the final form of the linearized state equation:

$$\boldsymbol{\delta}\dot{\boldsymbol{z}} \cong \mathbf{A}\boldsymbol{\delta z} + \mathbf{B}\delta u \tag{B.12}$$

For an n^{th} order system with one input, $\mathbf{A}$ will be the n x n system matrix and $\mathbf{B}$ will be the n x 1 input vector.

The linearized output equation is derived using the same process. Perform the Taylor Series expansion of $h_o(\boldsymbol{z})$ about $\boldsymbol{z}^*$, neglecting higher order terms:

$$h_o(\boldsymbol{z}) \cong h_o(\boldsymbol{z}^*) + \left(\frac{\partial h_o}{\partial \boldsymbol{z}}\right)_{\boldsymbol{z}=\boldsymbol{z}^*} \boldsymbol{\delta z} \tag{B.13}$$

From Eq. B.2:

$$y^* = h_o(\boldsymbol{z}^*) \tag{B.14}$$

Substitute Eqs. B.2 and B.14 into B.13:

$$y \cong y^* + \left(\frac{\partial h_o}{\partial \boldsymbol{z}}\right)_{\boldsymbol{z}=\boldsymbol{z}^*} \boldsymbol{\delta z} \tag{B.15}$$

In Eq B.15, subtract y^* from the left and right sides and substitute Eq. B.6 into the left side:

$$\delta y \cong \left(\frac{\partial h_o}{\partial \boldsymbol{z}}\right)_{\boldsymbol{z}=\boldsymbol{z}^*} \boldsymbol{\delta z} \tag{B.16}$$

Defining:

$$\mathbf{C} = \left(\frac{\partial h_o}{\partial \boldsymbol{z}} \right)_{\boldsymbol{z}=\boldsymbol{z}^*} \tag{B.17}$$

produces the final form of the linearized output equation:

$$\delta y \cong \mathbf{C}\boldsymbol{\delta z} \tag{B.18}$$

For an nth order system with one output, $\mathbf{C}$ will be the 1 x n output vector.

B.2 DISCRETE-TIME SYSTEM

To derive the discrete, linear, state-space equations note that continuous-time equations can be sampled at specific instants in time to produce discrete equations. Starting with the continuous, linear, state-space equation:

$$\boldsymbol{\delta \dot{z}} = \mathbf{A}\boldsymbol{\delta z} + \mathbf{B}\delta u \,, \tag{B.12}$$

Recall the general solution to the linear state-space equation:

$$\boldsymbol{\delta z}(t) = \boldsymbol{\Phi}(t)\boldsymbol{\delta z}(0) + \int_0^t \boldsymbol{\Phi}(\tau)\mathbf{B}\,\delta u(\tau) d\tau \,. \tag{B.19}$$

Use Eq. B.20 to solve the state equation at the time T_s:

$$\boldsymbol{\delta z}(T_s) = \boldsymbol{\Phi}(T_s)\boldsymbol{\delta z}(0) + \int_0^{T_s} \boldsymbol{\Phi}(\tau)\mathbf{B}\,\delta u(\tau) d\tau \,. \tag{B.20}$$

B.21 can be used to produce discrete state solutions as shown below:

$$\boldsymbol{\delta z}_{k+1} = \boldsymbol{\Phi}(T_s)\boldsymbol{\delta z}_k + u_k \int_0^{T_s} \boldsymbol{\Phi}(\tau)\mathbf{B}\,\delta u(\tau) d\tau \tag{B.21}$$

where $\boldsymbol{\delta z}_k = \boldsymbol{\delta z}(kT_s)$, $\boldsymbol{\delta z}_{k+1} = \boldsymbol{\delta z}((k+1)T_s) = \boldsymbol{\delta z}(kT_s + T_s)$, and u_k is assumed constant over a sample period. Rewriting Eq. B.22:

$$\boldsymbol{\delta z}_{k+1} = \boldsymbol{\Phi}_k \boldsymbol{\delta z}_k + \mathbf{B}_k \delta u_k \tag{B.22}$$

where $\mathbf{B}_k = \int_0^{T_s} \mathbf{\Phi}(\tau)\mathbf{B}d\tau$. If $\mathbf{B}$ is constant, redefine $\mathbf{B}_k$ as:

$$\mathbf{B}_k = \mathbf{B}\left(\mathbf{I}T_s + \mathbf{A}\frac{T_s^2}{2!} + ...\right) \tag{B.23}$$

For the output equation:

$$\delta y = \mathbf{C}\boldsymbol{\delta z} \tag{B.18}$$

$\mathbf{C}_k = \mathbf{C}$ produces the discrete output equation:

$$\delta y_k = \mathbf{C}_k \boldsymbol{\delta z}_k \tag{B.24}$$

B.3 EQUILIBRIUM POINTS

To determine the equilibrium point ($\boldsymbol{z}^*, u^*$), start with the nonlinear, state-space equation of motion:

$$\dot{\boldsymbol{z}} = \boldsymbol{f}_o(\boldsymbol{z}, u) \tag{B.25}$$

The nonlinear state function vector was determined to be:

$$\boldsymbol{f}_o(\boldsymbol{z},u) = \begin{bmatrix} z_2 \\ \frac{1}{m}\left(\frac{z_4^2}{2\beta_2} - z_3 A - k(z_1 + X_{sid})\right) \\ \frac{\beta(V_o + x_c A)}{(V_o - z_1 A)(z_1 + x_c)A}\left(-\frac{\pi R^4}{8\mu L_p} z_3 + z_2 A\right) \\ -\frac{R_2}{\beta_2}(d + z_1)z_4 + V \end{bmatrix}, \tag{B.26}$$

where $u = V$. The equilibrium point ($\boldsymbol{z}^*, u^*$) was obtained as the point which produced $\boldsymbol{f}_o(\boldsymbol{z}^*, u^*) = \boldsymbol{0}$. Looking at each element of $\boldsymbol{f}_o(\boldsymbol{z}^*, u^*) = \boldsymbol{0}$:

$$0 = z_2^* \tag{B.27}$$

$$0 = \frac{\left(z_4^*\right)^2}{2\beta_2} - z_3^* A - k\left(z_1^* + X_{sid}\right) \tag{B.28}$$

$$0 = -\frac{\pi R^4}{8\mu L_p} z_3^* + z_2^* A \tag{B.29}$$

$$0 = -\frac{R_2}{\beta_2}\left(d + z_1^*\right) z_4^* + u^* \tag{B.30}$$

Equations B.27 and B.29 together indicate that $z_2^* = z_3^* = 0$. Substituting $z_3 = 0$ into Eq. B.28 and solving for z_1^* produces:

$$z_1^* = \frac{\left(z_4^*\right)^2}{2k\beta_2} - X_{sid}\,. \tag{B.31}$$

Finally, solving Eq. B.30 for z_4^* produces:

$$z_4^* = u^* \frac{\beta_2}{R_2}\left(\frac{1}{d + z_1^*}\right) \tag{B.32}$$

Eqs. B.31, B.32, $z_2^* = 0$, and $z_3^* = 0$ comprise the equilibrium point. The variables z_1^* and z_4^* can be determined for a given u^* by simultaneous solution of Eqs. B.31 and B.32. In the present research, the variable z_4^* and input u^* were determined for a given, desired, pilot poppet position (z_1^*) by simultaneous solution of Eqs. B.31 and B.32.

B.4 SOLENOID PARAMETERS

The solenoid EMA parameters β_2 and d are composite parameters calculated as follows:

$$\beta_2 = \frac{\lambda_\phi^2 N^2}{\mu_o A_2 C_o^2}, \tag{B.33}$$

where λ_ϕ is the flux leakage coefficient, N is the number of turns in the EMA coil, μ_o is the permeability in free space, A_2 is the area of the gap between the armature and core, and C_o is a constant used to determine the reluctance of the solenoid ($\Re = C_o g + C_1$, where g is the width of the gap between the armature and core)

$$d = d_o + x_{\max} \tag{B.34}$$

where $d_o = \frac{C_1}{C_o}$ and $x_{\max}$ is the maximum displacement of the armature. In the present work and the literature, the terms can be determined using empirical methods. A more rigorous derivation is presented in [17-19].

REFERENCES

[1] Zhang, R., Alleyne, A. G., Prasetiawan, E. A., "Performance Limitations of a Class of Two-Stage Electro-Hydraulic Flow Valves." International Journal of Fluid Power, Vol. 3, 2002, No. 1.

[2] Schexnayder, L. F., "Poppet Valve with Force Feedback Control." U.S. Patent 5 421 545, Jun. 6, 1995.

[3] Aardema, J. A., "Pilot Valve for a Flow Amplifying Poppet Valve." U.S. Patent 5 645 263, Jul. 8, 1997.

[4] Yang, X., Paik, M. J., Pfaff, J. L., "Pilot Operated Control Valve Having a Poppet With Integral Pressure Compensating Mechanism." U.S. Patent 6 745 992, Jun. 8, 2004

[5] Yang, X., Stephenson, D. B., Paik, M. J., "Hydraulic Poppet Valve with Force Feedback." U.S. Patent 6 869 060, Mar. 22 2005.

[6] Manring, N.D., 2005. *Hydraulic Control Systems*. Hoboken, NJ: John Wiley & Sons, pp. 224-228.

[7] Hayashi, S., 1995, "Instability of Poppet Valve Circuit." JSME International Journal Series C, Vol. 38, No. (3), pp. 357-366.

[8] Funk, J.E., "Poppet Valve Stability." Journal of Basic Engineering, June 1964, pp. 207-212.

[9] Hayashi, S. and Ohi, K., 1988 "Digital Simulation of Dynamic Behaviors of Poppet Valve Circuit." 2nd Int. Symp. Fluid-Control, Measurement, Mechanics and Visualization, p. 23.

[10] Muller, M.T., 2005. *Modeling, Design, and Control of Forced-Feedback Metering Poppet Valve System*. M.S. thesis, University of Missouri-Columbia.

[11] Muller, M.T., and Fales, R., 2006. "Design and analysis of a two-stage poppet valve for flow control" American Control Conference.

[12] Fales, R., 2005. "Stability and Performance Analysis of a Metering Poppet Valve." ASME International Mechanical Engineering Congress and Exposition, Orlando, FL.

[13] Opdenbosch, P., Sadegh, N., Book, W., 2004. "Modeling and Control of an Electro-hydraulic Poppet Valve." ASME International Mechanical Engineering Congress and Exposition, Anaheim, CA.

[14] Sohl, G.A., Bobrow, J.E., 1999. “Experiments and Simulations on the Nonlinear Control of a Hydraulic Servo system.” IEEE Transactions on Control Systems Technology, Vol. 7, No. 2, pp. 238-247.

[15] Hahn, H., Piepenbrick, A., Leimback, K.-D., 1994. “Input/Output Linearization Control of an Electro Servo-Hydraulic Actuator.” IEEE pp. 995-1000

[16] Eyabi, P., 2003. *Modeling and Sensorless Control of Solenoidal Actuators*. Ph.D. thesis, The Ohio State University.

[17] Yuan, Q., Li, P.Y., 2004. “Self-Calibration of Push-Pull Solenoid Actuators in Electrohydraulic Valves.” ASME International Mechanical Engineering Congress and RD&D Expo, Anaheim, CA.

[18] Yuan, Q., Li, P.Y., 2004. “Self-Sensing Actuators in Electrohydraulic Valves.” ASME International Mechanical Engineering Congress and Exposition, Anaheim, CA.

[19] Yuan, Q., Li, P.Y., 2005. “On Self-Sensing Actuators For Electrohydraulic Valves: Comparisons Between Boxcar Window Observer and Kalman Filter.” ASME International Mechanical Engineering Congress and Exposition, Orlando, FL.

[20] Noh, M.D., Maslen, E.H., 1997. “Self-sensing magnetic bearings using parameter estimation.” IEEE Transactions on Instrumentation and Measurement, 46 (1), pp. 45-50.

[21] Zhan, Y.J., Chan, C.C., Chau, K.T., 1999. “A novel sliding-mode observer for indirect position sensing of switched reluctance motor drives.” IEEE Transactions on Industrial Electronics, 46 (2), pp. 390-397.

[22] McCann, R.A., Islam, M.S., Husain, I., 2001. “Application of a sliding mode observer for position and speed estimation in switched reluctance motor drives.” IEEE Transactions on Industrial Electronics, 37(1), pp.51-58.

[23] Friedland, B., 1986. *Control System Design: An Introduction to State Space Methods*. Boston: McGraw-Hill.

[24] Brown, R.G., Hwang, P.Y.C., 1997. *Introduction To Random Signals and Applied Kalman Filtering: with MATLAB Exercises and Solutions*. 3rd ed. New York: John Wiley and Sons.

[25] Khalil, K., 2002. *Nonlinear Systems*, Upper Saddle River: Prentice Hall, pp 505-550.

VITA

Curtis Harvey Omari Cline, was born September 26, 1978 in St. Charles, Missouri. He attended Francis Howell North High School and immediately began college following graduation. He received his B.S, M.S, and Ph.D. in Mechanical & Aerospace Engineering from the University of Missouri-Columbia in 2000, 2002, and 2007, respectively. His academic background includes dynamic modeling and control of systems. His personal interests include chess, basketball, soccer, technical reading, Biblical reflection and study, and spending time with his wife.